

# <sup>1</sup> Search for Double Beta Decay to Excited States

<sup>2</sup> I. Guinn

<sup>3</sup> University of North Carolina at Chapel Hill, NC,  
<sup>4</sup> USA

## <sup>5</sup> CONTENTS

<sup>6</sup> I. Introduction	<sup>2</sup>
<sup>7</sup> II. Simulation of Excited State Decays	<sup>2</sup>
A. Comparing DECAY0 to the Kotila and Iachello generator	<sup>3</sup>
<sup>9</sup> III. Background Model Simulation	<sup>4</sup>
<sup>10</sup> IV. $^{56}\text{Co}$ Simulation	<sup>5</sup>
<sup>11</sup> V. Simulation Skimming	<sup>5</sup>
<sup>12</sup> VI. Selection of Multi-Detector Events	<sup>8</sup>
A. Variation in Detector Configuration	<sup>8</sup>
B. Dead Layer Effects	<sup>9</sup>
C. Dead Time Effects	<sup>9</sup>
D. Simulation Validation and Errors	<sup>9</sup>
<sup>17</sup> VII. Region of Interest Selection	<sup>12</sup>
A. Signal ROI Optimization	<sup>14</sup>
B. Background ROI Selection	<sup>15</sup>
C. ROI Detection Efficiency and Uncertainty	<sup>15</sup>
D. Detector Crosstalk	<sup>16</sup>
<sup>22</sup> VIII. Background Cuts	<sup>19</sup>
A. Enriched Source Detector Cut	<sup>19</sup>
B. Coincident and Sum Energy Cuts	<sup>19</sup>
C. Muon Veto Cut	<sup>22</sup>
<sup>26</sup> IX. Combined Detection Efficiency for $\beta\beta$ E.S.	<sup>23</sup>
<sup>27</sup> X. Double Beta Decay to Excited States Results	<sup>24</sup>
<sup>28</sup> XI. Validation	<sup>25</sup>
A. Data Rate	<sup>25</sup>
B. Background Cut Evaluation	<sup>25</sup>
<sup>31</sup> XII. Results	<sup>26</sup>
A. Statistical Methods	<sup>26</sup>
B. Limits and Sensitivities	<sup>31</sup>
C. Background Model Discussion	<sup>32</sup>
<sup>35</sup> XIII. Unblinding Plan	<sup>33</sup>
<sup>36</sup> References	<sup>34</sup>
<sup>37</sup> A. Detailed Results for All Decay Modes	<sup>36</sup>
<sup>38</sup> B. $2\nu\beta\beta$ to $0_1^+$	<sup>36</sup>
<sup>39</sup> C. $2\nu\beta\beta$ to $2_1^+$	<sup>43</sup>
<sup>40</sup> D. $2\nu\beta\beta$ to $2_2^+$	<sup>50</sup>
1. 559 keV peak	<sup>50</sup>
2. 657 keV peak	<sup>57</sup>
3. 1216 keV peak	<sup>63</sup>
<sup>44</sup> E. $0\nu\beta\beta$ to $0_1^+$	<sup>69</sup>
<sup>45</sup> F. $0\nu\beta\beta$ to $2_1^+$	<sup>76</sup>
<sup>46</sup> G. $0\nu\beta\beta$ to $2_2^+$	<sup>83</sup>

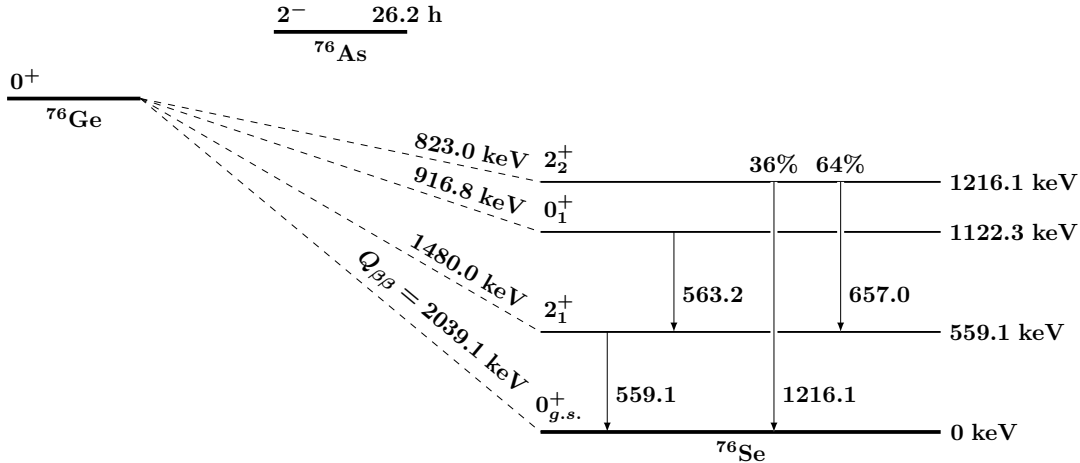


47	1. 559 keV peak	83
48	2. 657 keV peak	90
49	3. 1216 keV peak	96
50	H. Sensitivity and Discovery Potential	102

## 51 I. INTRODUCTION

52  $^{76}\text{Se}$  has 3 excited states that  $^{76}\text{Ge}$  can decay into in addition to the ground state, as shown in figure 15. While  
 53 the ground state decay has been observed, none of the decays to excited states have been yet. Each excited state  
 54 decay will have a  $\beta\beta$ -decay with a reduced  $Q$ -value compared to the ground state decay. The excited state decays will  
 55 also promptly produce one or two  $\gamma$ -rays at known energies. These  $\gamma$ s will typically travel several centimeters before  
 56 absorption and will often hit a different detector from the  $\beta\beta$ -decay site, meaning that we can search for peaks at  
 57 these energies.

58



59 FIG. 1 Energy level diagram for  $\beta\beta$ -decay of  $^{76}\text{Ge}$  to  $^{76}\text{Se}$ , including excited states. The  $Q$ -values for each decay branch and  
 60 the energies and branching ratios for the deexcitation  $\gamma$ s are shown next to their corresponding lines.

61

62 Furthermore, since these  $\gamma$ s hit separate detectors, this signal is inherently multi-site event. As shown in figure 2,  
 63 by searching for the peak only in events with high hit multiplicity, i.e. events that involve 2 or more detectors hit,  
 64  $\sim 85\%$  of backgrounds can be cut, while only sacrificing  $\sim 25\%$  of the signal. Furthermore, the coincident detector  
 65 hit(s) can provide additional observables that can be used to further discriminate excited state signals from multi-site  
 66 backgrounds. This chapter will describe the various background reduction data cuts and how they are implemented.  
 67 It will also evaluate the detection efficiency and systematic error associated with each cut based on simulations of the  
 MAJORANA DEMONSTRATOR.

## 68 II. SIMULATION OF EXCITED STATE DECAYS

69 Simulations of the  $^{76}\text{Ge}$  decay to excited states of  $^{76}\text{Se}$  are used to evaluate the detection efficiency of the analysis  
 70 presented in this document. Two different event generators are used to generate  $^{76}\text{Ge}$   $\beta\beta$ -decay within MAGE. The  
 71 first generator uses calculations of the phase space factors from J. Kotila and F. Iachello[1]. It is implemented in the  
 72 mage class `MGGeneratorDoubleBeta` using data tables with the distribution of both electron energies and angular  
 73 correlations. These data tables are provided for the  $2\nu\beta\beta$  and  $0\nu\beta\beta$  decays to the ground state of  $^{76}\text{Se}$ , but not for the  
 74 decays to any excited state of  $^{76}\text{Se}$ . This calculation is an improvement over other phase space calculations thanks to  
 75 an exact evaluation of the Dirac wave functions of the electrons involving a finite nuclear size and electron screening.

76 A second event generator packaged with MAGE is `DECAY0`[2], a FORTRAN program that generates a wide variety  
 77 of  $\beta\beta$ - and  $\beta$ -decays. `DECAY0` is capable of generating  $2\nu\beta\beta$  and  $0\nu\beta\beta$  for  $^{76}\text{Ge}$  to  $0^+$  and  $2^+$  excited states of  $^{76}\text{Se}$   
 78 using a variety of physics mechanisms. For the excited state decays, the deexcitation  $\gamma$ s and conversion electrons are  
 79 also generated. Several modifications were made to `DECAY0` for this analysis. First, the precision of the excited state

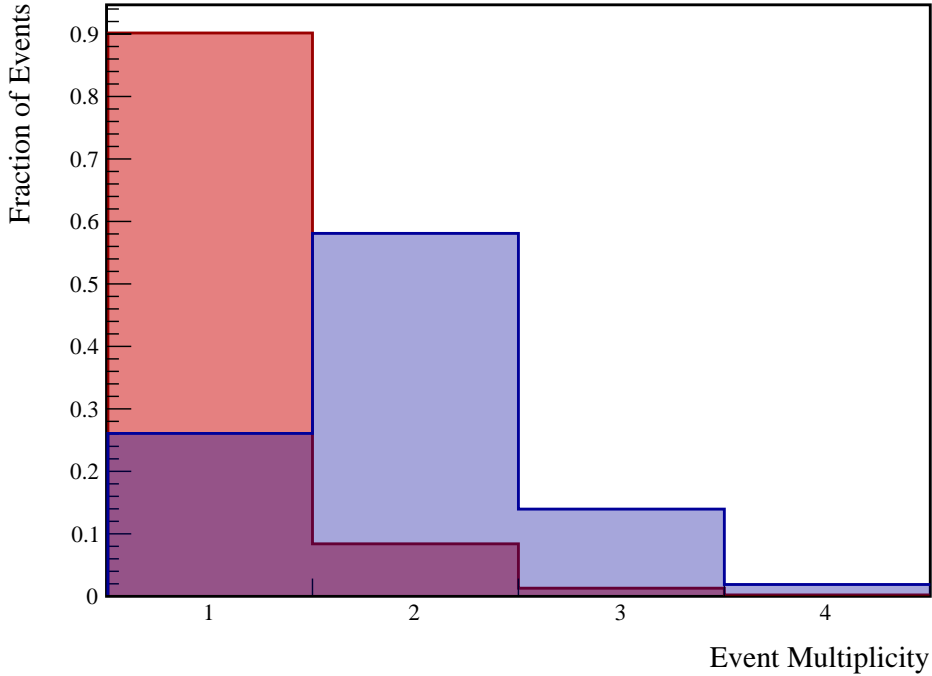


FIG. 2 The simulated distribution of ROI event multiplicities in the background model (red) and  $\beta\beta$  E.S. (blue) to  $0_1^+$  decay. These simulations use the DS6 detector configuration.

deexcitation energies was increased from 1 keV to 0.001 keV (The  $\gamma$  energies changed from 559 to 559.101 keV, from 563 to 563.178 keV, from 657 to 657.041 keV, and from 1216 to 1216.104 keV). Second, angular correlations were added for the  $2_2^+ - 2_1^+ - 0_{g.s.}^+$  deexcitation  $\gamma$  cascade which involves a 657 keV  $\gamma$  with multipolarity E2+M1 and mixing ratio of +5.2 followed by a 559 keV  $\gamma$  with multipolarity E2[3]. The angular distribution between the  $\gamma$ s is[4]

$$P(\theta) \propto 1 - 0.372 \cdot \cos^2(\theta) + 0.0439 \cdot \cos^4(\theta) \quad (1)$$

The angular correlation for the  $0_1^+ - 2_1^+ - 0_{g.s.}^+$  deexcitation was already correctly included in DECAY0, and is represented by the angular distribution[3; 4]

$$P(\theta) \propto 1 - 3 \cdot \cos^2(\theta) + 4 \cdot \cos^4(\theta) \quad (2)$$

Running DECAY0 produces data files with the initial momenta of the generated particles. The MAGE class MGGeneratorDecay0 reads these datafiles and generates initial positions for these events.

Simulations were run for  ${}^{76}\text{Ge}$   $2\nu\beta\beta$  and  $0\nu\beta\beta$  to the  $0_1^+$ ,  $2_1^+$  and  $2_2^+$  excited states of  ${}^{76}\text{Se}$  using the DECAY0 generator. For each decay mode, 5,000,000 event primaries were generated in the bulk of the enriched detectors and 500,000 primaries were generated in the bulk of the natural detectors. These events were skimmed with the relative activities set equal to the total isotopic mass in each set of detectors: 26.2538 kg in enriched detectors, and 1.1232 kg in natural detectors. These simulations were additionally post-processed and skim files were produced both with and without a dead layer, and with and without dead times. Figure 3 shows an energy spectrum of multiplicity 2 events produced by the simulation of the  ${}^{76}\text{Ge}$  decay to the  $0_1^+$  excited state of  ${}^{76}\text{Se}$ .

### A. Comparing DECAY0 to the Kotila and Iachello generator

The Kotila and Iachello generator performs a more accurate calculation of phase space than DECAY0 and is used for the MAJORANA DEMONSTRATOR's measurement of  $2\nu\beta\beta$  and  $0\nu\beta\beta$  to the ground state. Because Kotila and Iachello present only the phase space integral for the excited state decays, and do not include the energy and angular

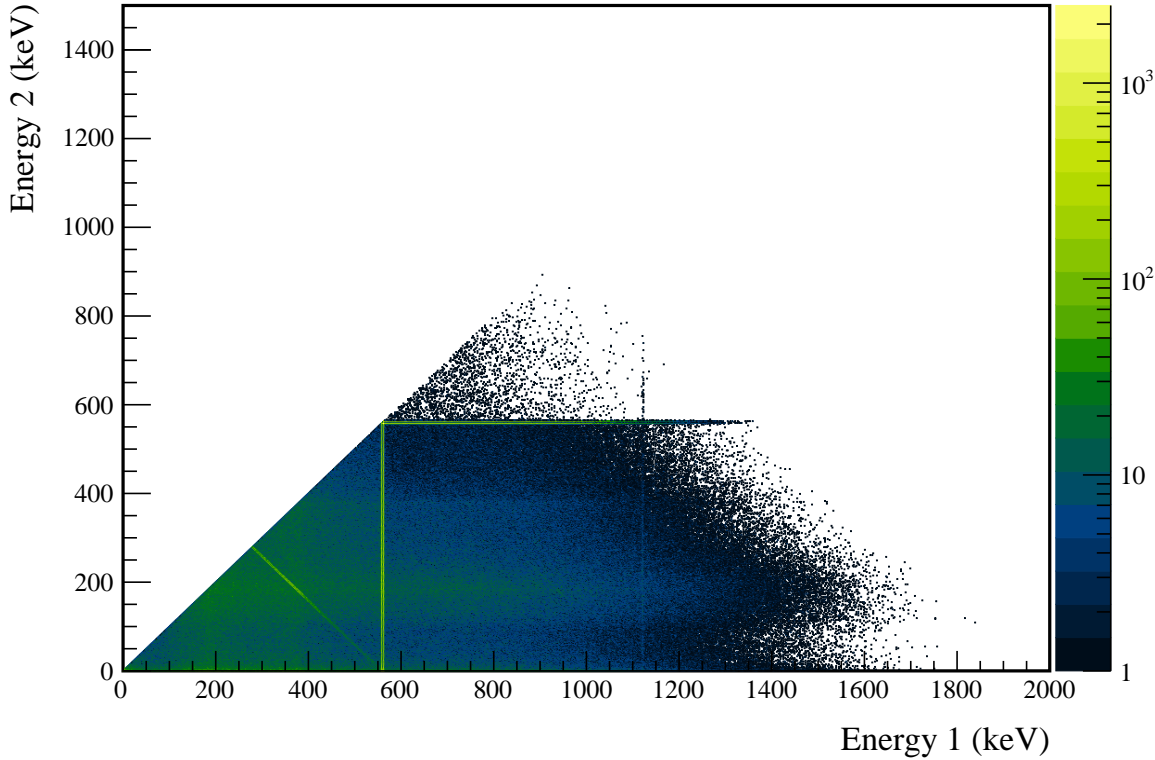


FIG. 3 Multiplicity 2 energy spectrum produced by a DECAY0 simulation of  $2\nu\beta\beta$  of  $^{76}\text{Ge}$  to the  $0_1^+$  state of  $^{76}\text{Se}$ .

distributions, DECAY0 is used for this analysis. To evaluate the accuracy of DECAY0, we can compare the spectrum of the  $2\nu\beta\beta$  to the ground state it generates to that of Kotila and Iachello; this comparison will reflect the error with respect to the true value if we assume that the errors corrected by Kotila and Iachello are the dominant errors in DECAY0. This comparison is performed using a Kolmogorov-Smirnov (KS) test. The KS test statistic is the maximum difference between the CDF of each normalized energy spectrum. As we will see in Section VIII.B, this test is useful in evaluating the uncertainties in the measurement presented in this document. The CDF difference is shown in Figure 4, with a KS statistic of 0.00081. While this error is statistically significant at a level of 97%, we will see that the systematic error generated is subdominant.

### III. BACKGROUND MODEL SIMULATION

A simulation of the background spectrum measured by the MAJORANA DEMONSTRATOR will be used to optimize the search for  $\beta\beta$  E.S.. MAGE simulations of a variety of decay chains, including  $^{232}\text{Th}$ ,  $^{238}\text{U}$ ,  $^{40}\text{K}$ ,  $^{60}\text{Co}$ ,  $^{222}\text{Rn}$  and  $^{68}\text{Ge}$ , have been run using event generators internal to GEANT4. A large number of component groups have been defined, encompassing one or more physical components of the experiment (e.g. all signal electronic connectors are a single component group). The event generators use the combined geometries of these groups to generate start positions, which can be in either the bulk of a component group, or on the surface. The activity of each isotope from each component group is determined by fitting a linear combination of the simulated energy spectra to the measured background spectrum. An incomplete version of this fit is used for this document, producing the spectra in Figures 5 and 6[5].  $^{68}\text{Ge}$  decays with a half-life of 271 days, so its activity is scaled to represent the exposure-weighted activity of each major dataset.  $^{210}\text{Pb}$  in the lead shield is simulated using a special generator that samples bremsstrahlung x-rays emitted from the surface of a thick lead shield [6].

The background model used for this analysis is known to be inaccurate. Since it is only used for optimizing the search for  $\beta\beta$  E.S. and is not important for the detection efficiency calculation, this does not affect the accuracy of

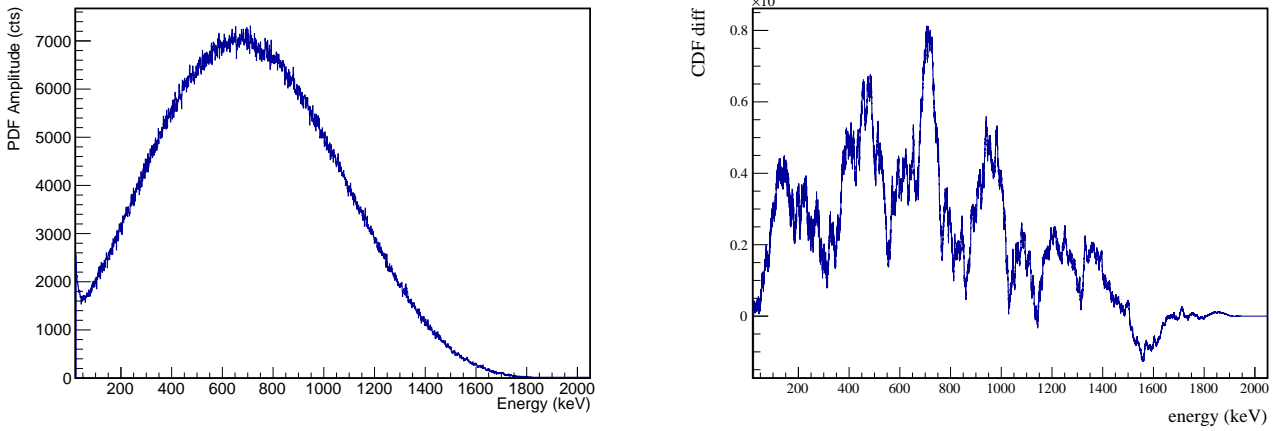


FIG. 4 A KS test is performed comparing the DECAYO  $2\nu\beta\beta$  to the ground state energy spectrum to that of Kotila and Iachello. The `decay0` spectrum is shown, along with the difference between the CDF of each spectrum.

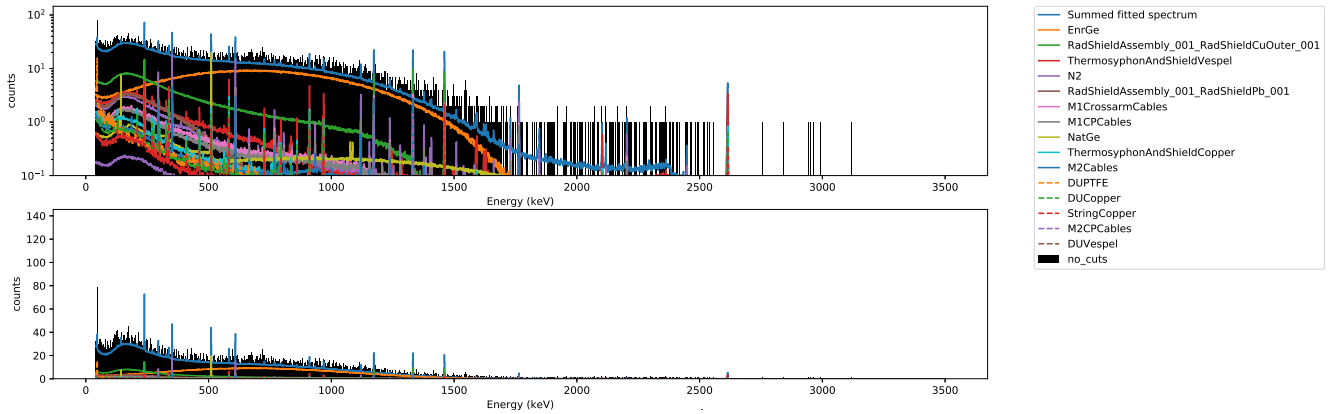


FIG. 5 Energy spectrum of observed multiplicity 1 events produced from a simulation of the preliminary background model, with the highest contributing components labelled.

121 the result presented. For future versions of this analysis, a complete and more accurate background model will be  
122 used, which should result in small improvements to the cut optimization.

#### 123 IV. $^{56}\text{CO}$ SIMULATION

124 Calibration of the MAJORANA DEMONSTRATOR is performed for each module using a line source that is injected  
125 by motor into a spiral track that winds around the module. Simulations of the  $^{56}\text{Co}$  calibration sources are performed  
126 using the GEANT4 generators for these isotopes, and a spiral position sampler written in MAGE. The detection  
127 efficiency test described in Section VI.D uses the  $^{56}\text{Co}$  source simulation. The simulated spectra for the  $^{56}\text{Co}$  source  
128 can be seen in Figures 7 and 8

#### 130 V. SIMULATION SKIMMING

131 Skim files are produced containing parameters of interest from the post-processed files using the software  
132 `es_skimsims`. Skim files can also mix postprocessed files from multiple sources in ratios corresponding to the  
133 various activities of the sources. `es_skimsims` accepts as input a JSON file listing the simulated sources, the  
134 desired activity of each source, and the number of available event primaries. From this, it calculates the number of

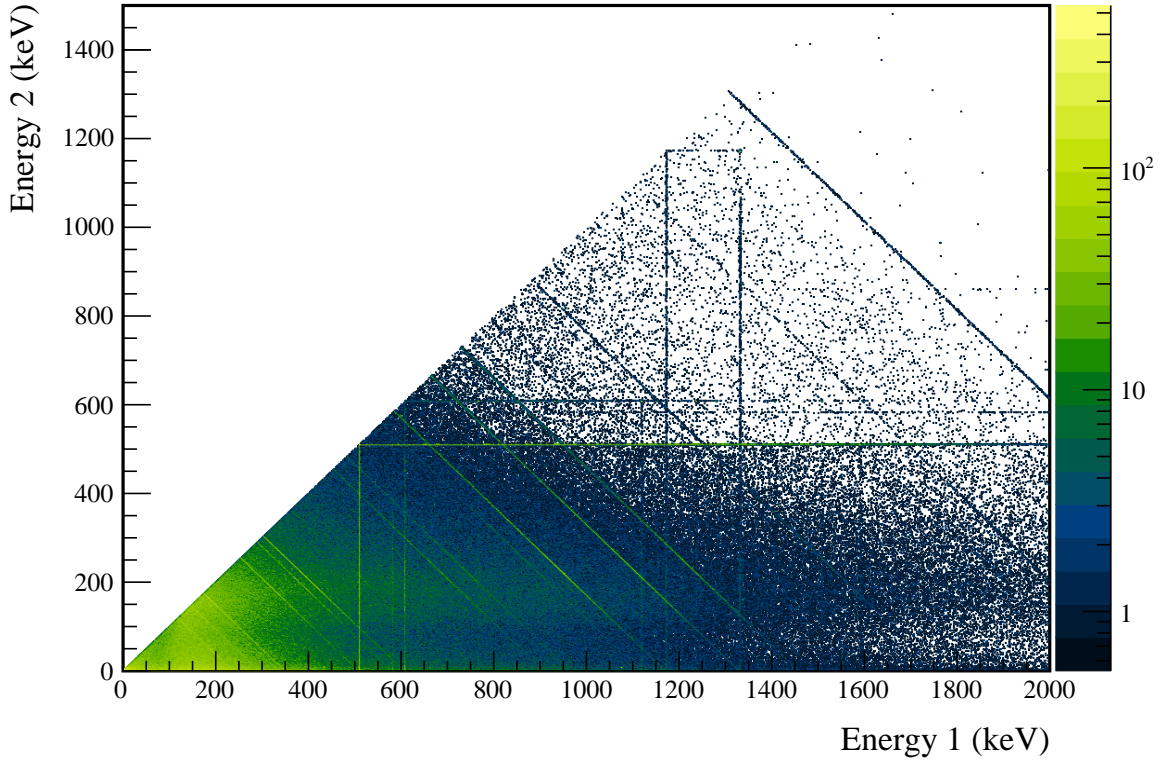


FIG. 6 Multiplicity 2 energy spectrum produced by a simulation of a preliminary version of the MAJORANA DEMONSTRATOR background model.

primaries to accept from each source by maximizing the total number of events used while maintaining the correct ratio according to the activities. Once this is done, it goes through each source sequentially and saves parameters of interest, including energy and detector position, to a `TTree`[7]. As will be discussed in future chapters, single detector events are of little interest to this analysis, so only multi-detector events are recorded in order to maintain a small file size. Multiplicity 1 events are recorded separately to a histogram according only to energy. The skimming process also accounts for which sets of detectors are enabled. Another input of `es_skimsims` is a JSON file containing a list of detector configurations, containing a bitmask describing which detectors are and are not enabled. The detector configurations will be discussed further in Section VI.A. When the skimmer encounters a disabled detector in an event, it ignores that detector, and does not count it towards the event multiplicity.

Each detector spends some portion of operating time dead, due to the finite rate at which the digitizers can retrigger, which typically cause  $< 0.1\%$  of HPGe hits to fail to read. However, during early datasets, some detector channels were effected by a bug in the Gretina cards that caused a high rate of triggers on negative-energy noise pulses, resulting in much higher dead time fractions. This effect is assumed to be random and uncorrelated between detectors. The dead time of each detector is measured by counting the number of pulser events in each detector for each run. Because the pulses occur at a fixed rate, we can predict the number of pulser events that should occur in any given run; the fraction of pulser events missed is assumed to represent the dead time fraction. The JSON detector configuration file contains the dead time fraction and the statistical uncertainty (assuming binomial statistics with respect to the total number of expected pulser events) on that fraction for each active detector. For each simulated detector hit, the data skimmer randomly throws out hits according to the probability represented by the dead fraction, treating that detector as inactive for that event.

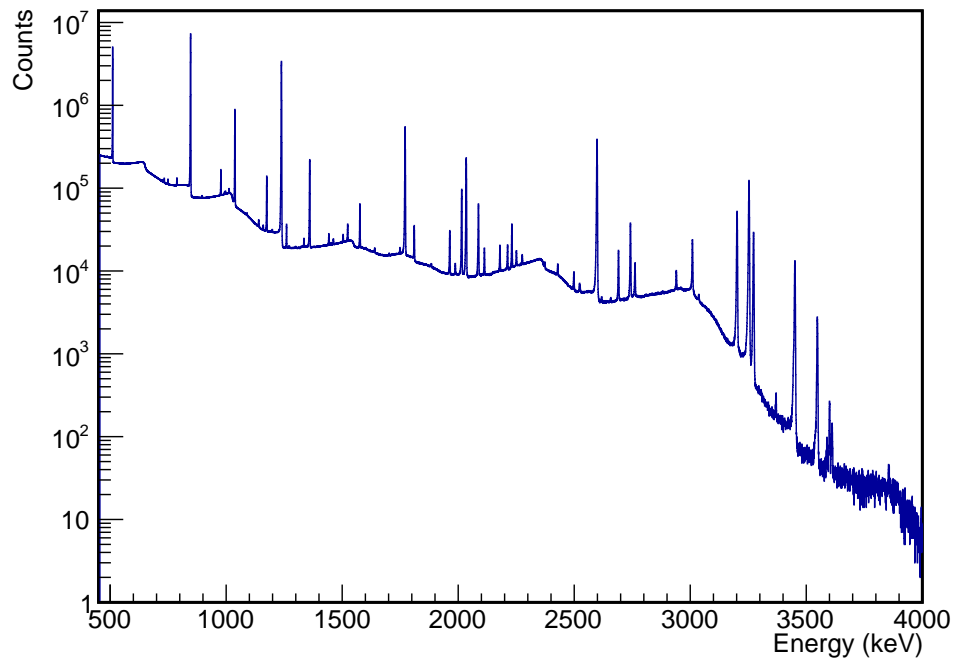


FIG. 7 Energy spectrum of multiplicity 1 events produced from a simulation of the  $^{56}\text{Co}$  line source inserted into the module 1 calibration track.

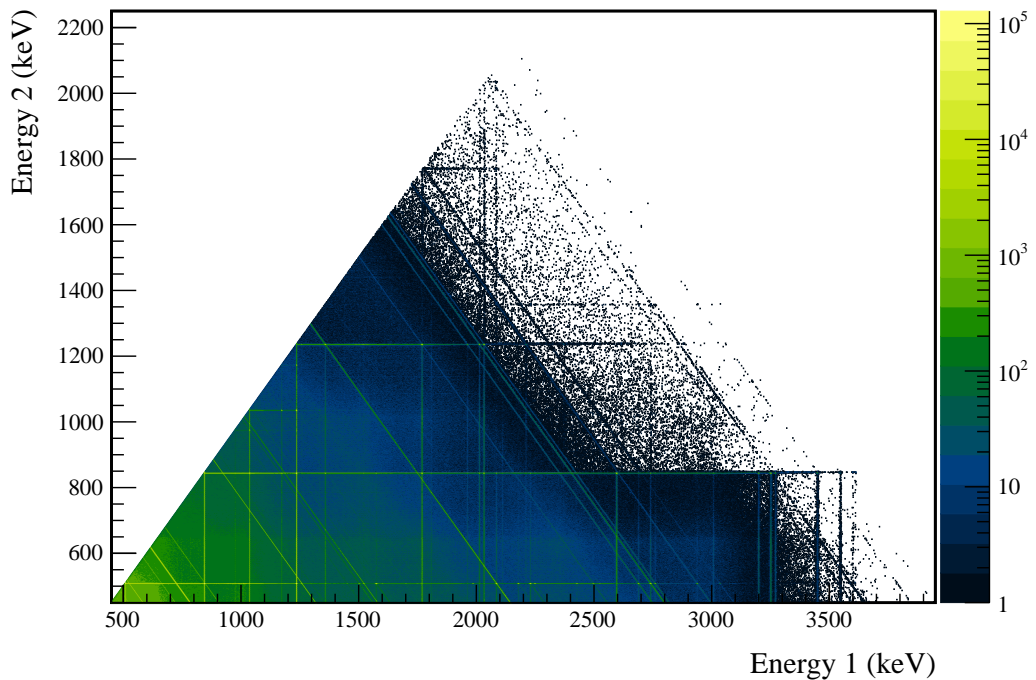


FIG. 8 Multiplicity 2 energy spectrum produced by a simulation of the  $^{56}\text{Co}$  line source inserted into the module 1 calibration track.



## 155 VI. SELECTION OF MULTI-DETECTOR EVENTS

156 Simultaneous detector hits are combined into events by the event builder. Events are combined in a  $4 \mu\text{s}$  rolling  
157 window. This window is expected to accept virtually all true coincidence events (see Figure 9). In a small number of  
158 runs, clocks between different Gretina cards were desynchronized. For these runs, the clocks were resynchronized by  
159 applying a timing offset during event building that is measured by seeking the time offset that aligns pulser events.  
160 With a typical overall rate between both modules of  $< 1 \text{ Hz}$ ,  $< 0.4\%$  of all multi-site events are expected to originate  
161 from accidental coincidences, making this a negligible background. Once all the data has gone through the standard  
162 MAJORANA DEMONSTRATOR processing chain, the skim files from all good open runs in datasets 16a are collected  
163 into a single skim file containing a `TTree` with only multi-site events by the program `es_skimdata`.

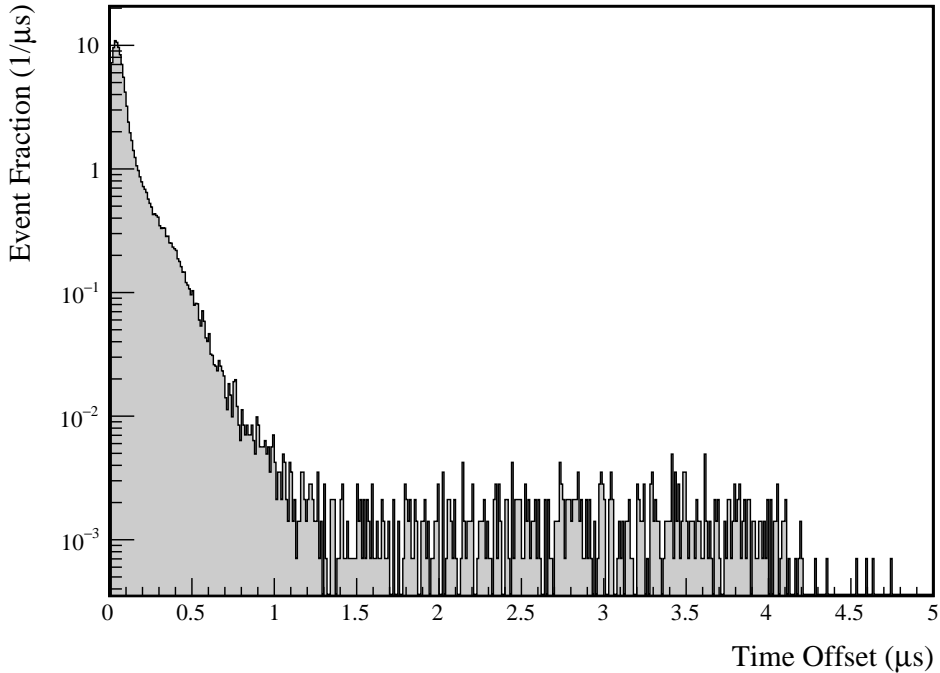


FIG. 9 Distribution of time interval between individual hits within a multi-detector event during a  $^{228}\text{Th}$  calibration run. Offsets of greater than  $\sim 1.5 \mu\text{s}$  are due to pileup, which is significant due to the high data rate of calibration runs. Offsets greater than  $\sim 4 \mu\text{s}$  must involve events with more than two hits, due to the event builder time window.

### 164 A. Variation in Detector Configuration

165 Throughout the runtime of the MAJORANA DEMONSTRATOR, not all detectors were simultaneously active, and  
166 within each dataset, the set of active detectors varied significantly. Because we are looking at multi-site event events,  
167 the detection efficiency for  $\beta\beta$  E.S. events in any detector depends on which other detectors are enabled. For this  
168 reason, detection efficiency is computed for each module in its entirety rather than for individual detectors. To account  
169 for changes in detector configuration, each dataset is divided into subdatasets based on which detectors are active.  
170 The subdatasets are described by a pair of 64-bit masks, one for each module, with each bit representing a single  
171 detector's state. To decode the bitmask, the  $b$ 'th least significant bit represents string position  $P$ , detector position  
172  $D$  if

$$b = 8 \cdot P + D \quad (3)$$

173 The set of runs and active channels for each run were determined by the run selection and data cleaning committee,  
174 and the procedures are outlined in [8]. The program `es_getdatasets` uses these selections to sort each run into a  
175 subdataset.



The detection efficiency is defined as the probability of a signal event in any detector, including inactive detectors. Detection efficiency is calculated individually for each subdataset and for each module by creating a separate skim file for each subdataset as outlined in Section V. The final efficiency is then computed as an isotopic exposure weighted average of the efficiency within each subdataset. Any efficiency uncertainties are assumed to be totally correlated between subdatasets. The livetime of each subdataset is calculated by the program `es_livetimes` by totalling the run time in each run, and subtracting any dead time that affects the entire module, including dead time caused by the muon veto system and by liquid nitrogen fills. Additional sources of dead time that affect individual detectors are calculated as inefficiencies rather than being subtracted from the livetime, as discussed in Section V. This is done because dead time in any individual detector affects the detection efficiency of all other detectors. The isotopic exposure is computed by multiplying the livetime of each module by the total isotopic mass in each module. Since this includes mass in inactive detectors and dead layers, the isotopic exposure for this analysis will differ from that presented in the  $0\nu\beta\beta$  analysis. Table I lists each subdataset along with its livetime and exposure.

## B. Dead Layer Effects

For multi-detector events, each individual hit may be degraded by the dead layer, so the loss of sensitivity from dead layers is larger for this search than for searches for single-site events. For this reason, dead layer effects are treated as a loss of detection efficiency instead of a loss of exposure (as in the  $0\nu\beta\beta$  analysis). Dead layers are included in the simulations as a part of simulation post-processing. To account for uncertainty in the thickness of the dead layer, two separate simulations are run, with and without dead layers. By comparing the efficiency measurement from each simulation, we measure the size of the dead layer effect. The percent uncertainty in the efficiency loss from dead layers is assumed to be the same as the percent uncertainty in the dead layer thickness. Typical loss of efficiency for multi-site peaks is 25-35%; for the  $2\nu\beta\beta$  to the  $0_1^+$  decay, the losses are 26% for module 1 and 34% for module 2. The uncertainty in the dead layer tends to be one of the dominant uncertainties in measuring the detection efficiency. This is much larger than the  $\sim 10\%$  loss seen in the  $0\nu\beta\beta$  analysis for two reasons. First, for multi-detector events, there are multiple hits that could possibly be lost to the dead layer. Second,  $\gamma$  hits will be more concentrated at the surface of the detectors, near the dead layers, than  $\beta\beta$  sites. The effect of dead layers on detection efficiency can be seen in Figure 10.

## C. Dead Time Effects

Detector dead times, which affect only a single detector at a time, reduce the detection efficiency for events that occur in all detectors in the module. For this reason, instead of subtracting these dead times from the livetime, the dead times are incorporated into the detection efficiency. Detector dead times are measured individually for each run by counting pulser events and comparing to the number of expected pulser events for each detector. The program `es_livetime` collects the detector dead times that are measured in this way and finds the average detector dead time for each subdataset. These dead times are then applied to the simulation skimming process as described in Section V. Similar to the dead layers, simulation files are produced with and without dead times in order to measure the size of the effect. Uncertainties in the detector dead times are measured as the statistical uncertainties from pulser counts. The percent uncertainty in efficiency loss from detector dead times is assumed to be the same as the average percent uncertainty in the detector dead time. Typical loss of efficiency from detector dead times range from 1-3%. For the  $2\nu\beta\beta$  to the  $0_1^+$  decay, the losses are 2.5% for module 1 and 1.9% for module 2. The effects of detector dead times can be seen in Figure 10.

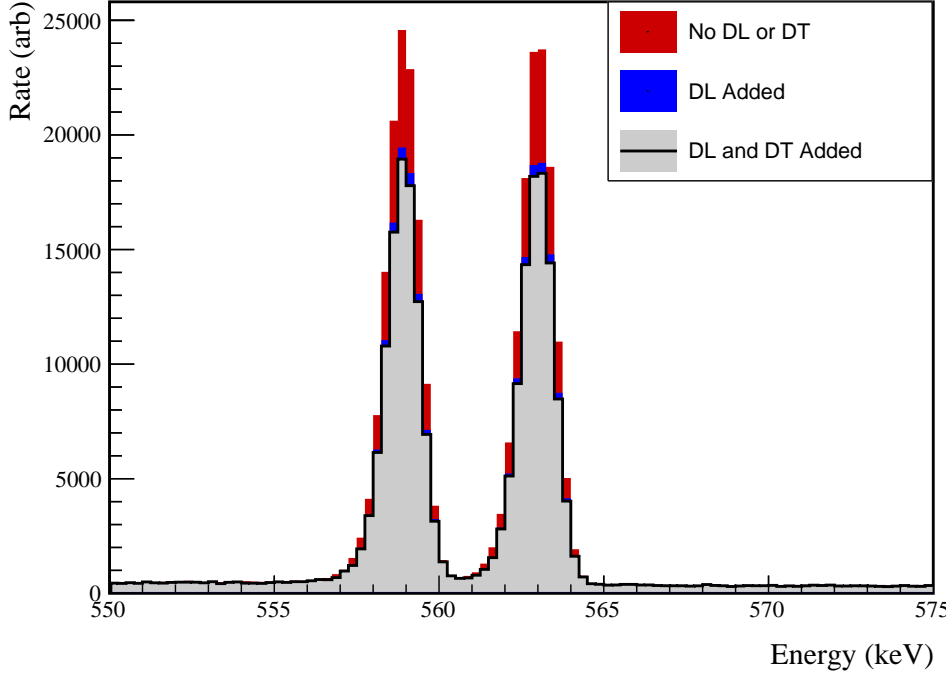
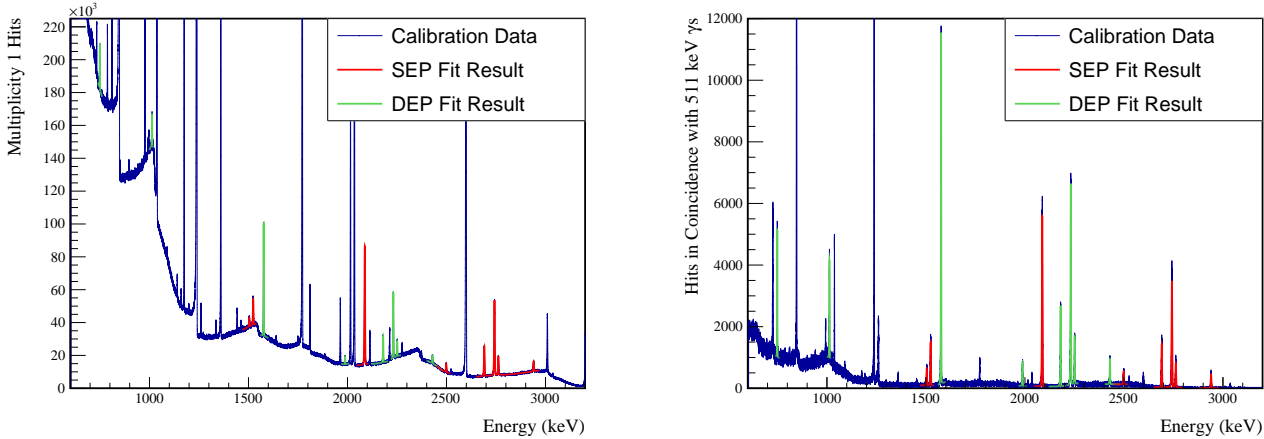
## D. Simulation Validation and Errors

In addition to dead layer and dead time effects that can be explicitly accounted for, other possible sources of systematic uncertainty from the simulation exist, such as inaccuracies in the simulation geometry. To account for these, we use pair production events from calibration runs as a proxy for  $\beta\beta$  E.S. events. In pair production events, an electron-positron pair is produced in the bulk of a detector, followed promptly by two 511 keV  $\gamma$ s from the annihilation of the positron. Because these events involve a single pair production site and the prompt emission of gamma rays which may be absorbed in a separate detector, they make a good proxy for  $\beta\beta$  E.S. events. In single-escape peak (SEP) events, one gamma is absorbed in the detector containing the pair-production, while the other escapes, resulting in a source detector hit with energy equal to the  $\gamma$  energy minus 511 keV. In double-escape peak (DEP) events, both



TABLE I List of each subdataset, labelled by the bitmasks defined in equation 3, with its livetime, detection efficiency measured for the  $\beta\beta$  E.S. to  $0^+_1$  decay, and total isotopic exposure. Note the large amount of variance in the detection efficiency.

DS	M1 Detector Mask	M2 Detector Mask	Run Time (days)	M1 L.T. (days)	M1 Eff.	M2 L.T. (days)	M2 Eff.	Exposure (kg.y)
DS1	061a08001e0e1c00	0000000000000000	2.64	2.60	1.72%	0.00	0.00%	0.109
DS1	161a08341e0e1c00	0000000000000000	0.02	0.02	2.00%	0.00	0.00%	0.001
DS1	161a0c341e0e1c00	0000000000000000	4.51	4.48	1.94%	0.00	0.00%	0.188
DS1	161a0c361e0e1c00	0000000000000000	3.49	3.48	1.47%	0.00	0.00%	0.146
DS1	1e1a0001e0e1c00	0000000000000000	7.82	7.73	2.04%	0.00	0.00%	0.324
DS1	1e1a08001e0e1c00	0000000000000000	37.30	36.87	2.23%	0.00	0.00%	1.547
DS1	1e1a08041e0e1c00	0000000000000000	6.26	6.19	2.30%	0.00	0.00%	0.260
DS1	1e1a08141e0e1c00	0000000000000000	0.26	0.25	2.32%	0.00	0.00%	0.011
DS1	1e1a08301e0e1c00	0000000000000000	1.40	1.37	2.33%	0.00	0.00%	0.057
DS1	1e1a08341e0e1c00	0000000000000000	7.58	7.50	2.12%	0.00	0.00%	0.315
DS1	1e1a0c001e0e1c00	0000000000000000	2.83	2.78	2.25%	0.00	0.00%	0.117
DS1	1e1a0c041e0e1c00	0000000000000000	0.04	0.04	2.24%	0.00	0.00%	0.002
DS1	1e1a0c341e0e1c00	0000000000000000	0.67	0.67	2.32%	0.00	0.00%	0.028
DS2	1e1a08001e0e1c00	0000000000000000	38.92	38.52	2.28%	0.00	0.00%	1.617
DS2	1e1a0c001e0e1c00	0000000000000000	1.22	1.19	2.27%	0.00	0.00%	0.050
DS3	1e1a0c3e1e0e1c00	0000000000000000	29.88	29.67	2.64%	0.00	0.00%	1.245
DS4	0000000000000000	1c061a16060e1e00	19.15	0.00	0.00%	18.85	1.89%	0.622
DS5a	0800002040e1c00	18060a02040e1e00	1.49	1.48	0.72%	1.46	1.16%	0.110
DS5a	08080020040e1c00	18060a16060e1e00	2.51	2.49	0.86%	2.47	1.56%	0.186
DS5a	08080030040e1c00	18060a02040e1e00	0.01	0.01	0.91%	0.01	1.14%	0.001
DS5a	0e1a04321e0e1c00	08020a16060e1e00	2.69	2.71	2.33%	2.66	1.23%	0.201
DS5a	0e1a0c321e0e1c00	0000000000000000	0.65	0.63	2.59%	0.00	0.00%	0.026
DS5a	0e1a0c321e0e1c00	08060a16060e1e00	1.24	1.24	2.58%	1.21	1.52%	0.092
DS5a	0e1a0c321e0e1c00	18060a02040e1e00	2.94	2.92	2.35%	2.89	1.15%	0.218
DS5a	0e1a0c321e0e1c00	18060a1406061600	0.04	0.04	2.56%	0.04	0.95%	0.003
DS5a	0e1a0c321e0e1c00	18060a1606060600	3.19	3.15	2.52%	3.16	0.82%	0.237
DS5a	0e1a0c321e0e1c00	18060a16060e0600	3.30	3.28	2.53%	3.29	0.84%	0.246
DS5a	0e1a0c3e1e0e1c00	1806020606081800	1.75	1.73	2.80%	1.73	0.76%	0.129
DS5a	0e1a0c3e1e0e1c00	18060216060c1c00	6.84	6.77	2.80%	6.74	1.12%	0.507
DS5a	0e1a0c3e1e0e1c00	18060216060e1e00	13.48	13.30	2.77%	13.27	1.26%	0.996
DS5a	0e1a0c3e1e0e1c00	18060816060e1c00	0.05	0.05	2.59%	0.05	1.30%	0.004
DS5a	0e1a0c3e1e0e1c00	18060a0606060600	2.16	2.12	2.77%	2.12	1.02%	0.159
DS5a	0e1a0c3e1e0e1c00	18060a16040e1e00	0.76	0.76	2.76%	0.74	1.29%	0.056
DS5a	0e1a0c3e1e0e1c00	18060a1606060600	0.25	0.25	2.78%	0.25	1.11%	0.019
DS5a	0e1a0c3e1e0e1c00	18060a1606061800	1.88	1.86	2.78%	1.86	1.04%	0.140
DS5a	0e1a0c3e1e0e1c00	18060a1606061600	9.20	9.13	2.75%	9.06	1.41%	0.682
DS5a	0e1a0c3e1e0e1c00	18060a16060c1c00	7.89	7.79	2.78%	7.79	1.41%	0.584
DS5a	0e1a0c3e1e0e1c00	18060a16060e1c00	11.68	11.53	2.43%	11.51	1.42%	0.864
DS5a	0e1a0c3e1e0e1c00	18060a16060e0600	5.21	5.15	2.76%	5.13	1.56%	0.386
DS5a	0e1a0c3e1e0e1c00	18061216060e1e00	2.39	2.37	2.77%	2.37	1.34%	0.178
DS5b	1e1a0c3e1e0c1c00	18061216060e1e00	24.46	24.09	2.75%	24.06	1.34%	1.805
DS5b	1e1a0c3e1e0c1c00	18061a16060e1e00	0.75	0.75	2.75%	0.75	1.73%	0.056
DS5b	1e1a0c3e1e0c1c00	18061216060e1e00	14.28	14.12	2.86%	14.07	1.24%	1.057
DS5c	1e1a0c3e1e0c1c00	0000000000000000	0.67	0.67	2.65%	0.00	0.00%	0.028
DS5c	1e1a0c3e1e0c1c00	00060216060e0e00	0.78	0.76	2.65%	0.78	0.84%	0.058
DS5c	1e1a0c3e1e0c1c00	00060a16060e0e00	5.91	5.82	2.75%	5.83	1.07%	0.437
DS5c	1e1a0c3e1e0c1c00	00061216060e0e00	38.85	38.45	2.73%	38.29	0.91%	2.877
DS6a	1200000000008000	1002020000604000	4.94	4.89	0.16%	4.89	0.42%	0.366
DS6a	12000c20000c1c00	18061216060c1e00	17.22	17.03	0.78%	17.03	1.13%	1.277
DS6a	12020000040c08000	1802020006040e00	5.69	5.63	0.29%	5.62	0.50%	0.422
DS6a	12020c00040c1800	1802020006040e00	7.90	7.79	0.68%	7.78	0.50%	0.584
DS6a	12080c20000c1c00	18061216060c1e00	12.23	12.11	0.96%	12.09	1.13%	0.907
DS6a	12120c3e1c0c1c00	18061216060c1e00	0.56	0.54	1.90%	0.56	1.10%	0.041
DS6a	16020c10040c1800	1806020006060e00	14.89	14.73	0.90%	14.68	0.69%	1.103
DS6a	160a0c321c0c1c00	1806021006061e00	5.87	5.80	2.05%	5.80	0.89%	0.435
DS6a	160a0c321c0c1c00	0000000000000000	0.23	0.23	2.31%	0.00	0.00%	0.010
DS6a	1e0a0c321c0c1c00	1806020006040200	10.00	9.89	2.31%	9.89	0.27%	0.741
DS6a	1e0a0c321c0c1c00	1806020006040600	7.43	7.35	2.31%	7.32	0.41%	0.550
DS6a	1e0a0c321c0c1c00	1806020006041600	4.88	4.83	2.31%	4.81	0.48%	0.362
DS6a	1e0a0c321c0c1c00	1806021006061e00	6.11	6.05	2.31%	6.04	0.89%	0.453
DS6a	1e120c3e1c0c1c00	18061216060c1e00	2.12	2.11	2.39%	2.09	1.13%	0.157
DS6a	1e1a0c321c0c1c00	1806020006060e00	5.56	5.51	2.49%	5.53	0.69%	0.414
DS6a	1e1a0c321c0c1c00	1806021006040e00	16.87	16.69	2.49%	16.64	0.69%	1.250
DS6a	1e1a0c321c0c1c00	1806021006041e00	11.93	11.81	2.49%	11.79	0.86%	0.885
DS6a	1e1a0c321c0c1c00	1806021006060e00	2.56	2.55	2.49%	2.55	0.73%	0.191
DS6a	1e1a0c3a1c0c1c00	1806020006040e00	8.66	8.59	2.60%	8.59	0.65%	0.644
DS6a	1e1a0c3a1c0c1c00	1806021006040e00	7.93	7.84	2.60%	7.83	0.69%	0.588
DS6a	1e1a0c3a1c0c1c00	1806021006041e00	1.24	1.23	2.60%	1.23	0.86%	0.092
DS6a	1e1a0c3e1c0c1c00	0000000000000000	0.06	0.05	2.69%	0.00	0.00%	0.002
DS6a	1e1a0c3e1c0c1c00	18060000006040e00	7.85	7.81	2.69%	7.54	0.61%	0.577
DS6a	1e1a0c3e1c0c1c00	18060200060404e00	5.96	5.88	2.65%	5.89	0.81%	0.441
DS6a	1e1a0c3e1c0c1c00	1806021006041e00	3.56	3.52	2.69%	3.52	0.86%	0.264
DS6a	1e1a0c3e1c0c1c00	1806021006061e00	15.72	15.56	2.69%	15.51	0.92%	1.165
DS6a	1e1a0c3e1c0c1c00	1806021206041e00	10.09	9.95	2.69%	9.97	0.89%	0.747
DS6a	1e1a0c3e1c0c1c00	18060214060c0e00	5.65	5.60	2.69%	5.66	0.80%	0.422
DS6a	1e1a0c3e1c0c1c00	18060214060c1e00	7.83	7.76	2.69%	7.74	0.98%	0.581
DS6a	1e1a0c3e1c0c1c00	18060214060e1e00	58.28	57.56	2.67%	57.43	0.95%	4.311
DS6a	1e1a0c3e1c0c1c00	1806121206041e00	1.00	0.98	2.69%	1.00	1.01%	0.074
DS6a	1e1a0c3e1c0c1c00	18061212060c1e00	12.96	12.80	2.69%	12.80	1.07%	0.959
DS6a	1e1a0c3e1c0c1c00	18061216060c1e00	26.05	25.76	2.69%	25.72	1.13%	1.930
DS Total	-	-	621.97	615.24	2.35%	487.97	1.00%	41.923

FIG. 10 Effect of dead layers and dead times on peak amplitudes for  $2\nu\beta\beta$  to the  $0_1^+$  peaks in multi-site event events.FIG. 11 Spectra are shown of multiplicity 1  $^{56}\text{Co}$  events (left) and multiplicity 2  $^{56}\text{Co}$  events in coincidence with an annihilation gamma. The results of the simultaneous peak fits are drawn in red (SEP fit) and green (DEP fit).

224 gammas escape the detector, resulting in a source detector hit with energy equal to the  $\gamma$  energy minus 1022 keV. Both  
 225 SEP and DEP events present the possibility for a second 511 keV detector hit. By comparing the rate of multiplicity-1  
 226 events in the SEPs and DEPs to the rate of multiplicity-2 events in which one hit falls into one of these peaks and  
 227 the other falls into the 511 keV peak, we can measure a proxy for the detection efficiency of our multi-site event  
 228 signature. By comparing this measurement to simulation, we can estimate the size of any unknown uncertainties in  
 229 our simulation-based efficiency estimate.

230 To achieve this, we will use a  $^{56}\text{Co}$  calibration source.  $^{56}\text{Co}$  presents the advantage of a large number of  $\gamma$ s at  
 231 energies high enough to cause pair production, which allows for a comparison of many peaks to our simulation. A



232  $^{56}\text{Co}$  line source was inserted into the module 1 calibration track on January 15, 2019 and 168.1 h of data were  
 233 recorded, until January 22, 2019. Immediately after this, the source was inserted into the module 2 calibration track  
 234 and 167.1 h of data were recorded until January 29, 2019. The source had a nominal activity of 6 kHz, resulting in a  
 235 high enough data rate that the energy threshold for each channel was raised to  $\sim 400$  keV. As discussed in Section IV,  
 236 3 billion event primaries were simulated for the  $^{56}\text{Co}$  source in each module's source track in order to achieve similar  
 237 events statistics for both the simulations and data. Simulations were run with and without dead layers.

238 8 SEPs and 7 DEPs were selected as proxies for the  $\beta\beta$  E.S. signal; these peaks were selected because of their  
 239 prominence above the Compton continuum and the absence of nearby peaks that would interfere with a peak-height  
 240 measurement. A simultaneous fit, using the multipeak fitter, of all SEPs as single-detector events and as two-detector  
 241 events in coincidence with a 511 keV peak event was performed in the calibration data and in the simulations both with  
 242 and without dead layers. SEPs and DEPs have abnormal peakshapes due to in-flight annihilation of the positrons,  
 243 which results in Doppler broadening of the peaks. For this reason, a high energy tail is added to the typical peak  
 244 shape function. The peak height ratios and uncertainties for peak  $k$  are determined as follows:

$$\epsilon_k = \frac{A_{k,m2}}{A_{k,m1}} \quad (4)$$

245

$$\sigma_{stat,k} = \epsilon_k \sqrt{\frac{\Sigma_{A,k,m1;A,k,m1}}{A_{k,m1}^2} - 2 \frac{\Sigma_{A,k,m1;A,k,m2}}{A_{k,m1} A_{k,m2}} + \frac{\Sigma_{A,k,m2;A,k,m2}}{A_{k,m2}^2}} \quad (5)$$

246 where  $A_{k,m1/2}$  are the fitted amplitudes of peak  $k$  with multiplicity 1 and multiplicity 2 respectively, and  $\Sigma_{A,k,m1/2;A,k,m1/2}$   
 247 is the fitted covariance matrix element for these amplitudes. The same process of simultaneously fitting DEPs is  
 248 followed to extract the DEP peak-height ratios. The measured data spectra and fit results are shown in Figure 11.

249 Figure 12 shows an overall offset that cannot be explained by statistical errors; this discrepancy is measured and  
 250 treated as a systematic error which will be applied to the  $\beta\beta$  E.S. measurement. Since some of this discrepancy can be  
 251 explained by the dead layer uncertainty, the difference between the simulated peak-height ratios with and without the  
 252 dead layer is multiplied by the percent uncertainty in the dead layer thickness in order to measure the systematic error  
 253 caused by the dead layer. Finally, a  $\chi^2$  value is computed for the comparison between the simulated and measured  
 254 peak-heights using the statistical and dead layer uncertainties.

$$\chi^2(\mu, \delta_{DL}) = \sum_{k=1}^N \frac{(\epsilon_{k,meas} - \epsilon_{k,sim} - \delta_{DL} \cdot \sigma_{DL,k} - \mu)^2}{\sigma_{stat,dat,k}^2 + \sigma_{stat,sim,k}^2} + \delta_{DL}^2 \quad (6)$$

255 where  $\sigma_{DL,k}$  is the uncertainty from dead layers,  $\delta_{DL}$  is the measured error from dead layers (correlated across all  
 256 peaks with a prior of 1  $\sigma$ ), and  $\mu$  is the mean error that remains. This  $\chi^2$  function is minimized with respect to  $\mu$   
 257 and  $\delta_{DL}$  and the profile likelihood is used to compute the uncertainty on  $\mu$ , using MINUIT[9]. The systematic error  
 258 is taken to be

$$\sigma_{sim}^2 = \mu^2 + \sigma_\mu^2 \quad (7)$$

259 Tables II and III list the peak height ratios and uncertainties for each peak for module 1 and module 2, respectively.  
 260 The final fractional uncertainties measured are  $\sigma_{sim,M1} = 0.0020$  and  $\sigma_{sim,M2} = 0.0047$ . This uncertainty is applied  
 261 directly to the detection efficiency measured before applying any other effects such as dead layers, dead times and  
 262 cuts, without any scaling. This uncertainty is one of the dominant uncertainties on the detection efficiency along with  
 263 the dead layer uncertainty; while the absolute uncertainty is small, because it is applied to the detection efficiency,  
 264 which tends to be  $\sim 5\%$ , directly rather than to the loss from an individual effect, the fractional uncertainty is on the  
 265 order of 10%. In cases where the detection efficiency is very low, such as the 1216 keV peak in module 2 from decays  
 266 to the  $2_2^+$  state, this uncertainty can completely overwhelm the detection efficiency. Figure 12 plots the peak height  
 267 ratios for simulated and measured data for both modules 1 and 2.

## 268 VII. REGION OF INTEREST SELECTION

269 Once the multi-site events have been collected, we want to search for detector hits with the energies of the  $\gamma$ s  
 270 emitted in each  $\beta\beta$  E.S. decay mode. To do this, a signal region of interest (ROI) must be identified. To estimate  
 271 the number of background events in the signal ROI, a background ROI must also be selected near the signal ROI.

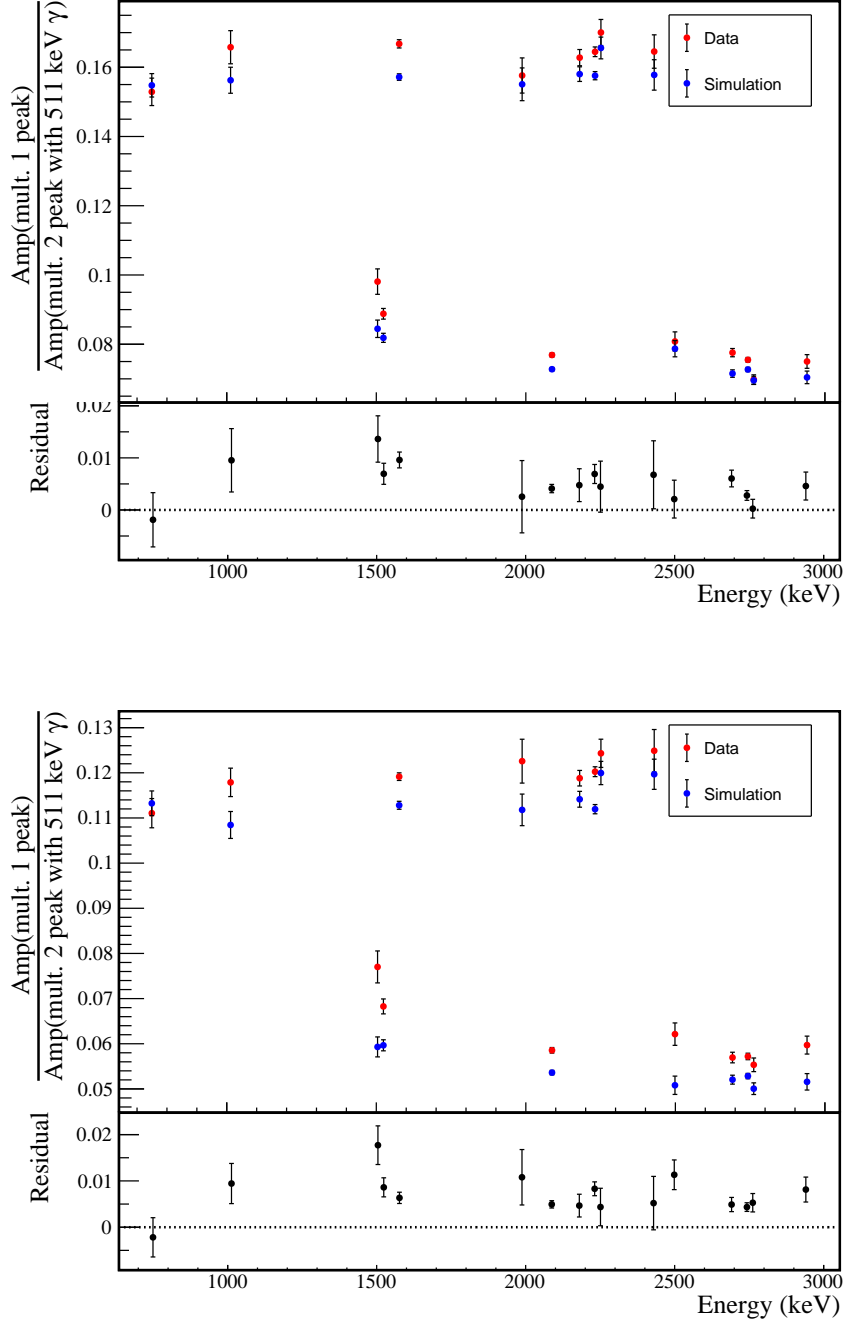


FIG. 12 Measurement of peak height ratios between multiplicity 1 events and multiplicity 2 events containing a 511 keV annihilation  $\gamma$  for both simulated and measured  $^{56}\text{Co}$  spectra. Only statistical error bars are drawn. These ratios are listed in tables II and III.

272 This section will describe the selection of the signal and background ROIs and the calculation of the efficiency and  
 273 uncertainties on the efficiency due to the ROI selection.

274 For each dataset, a simultaneous fit of many peaks is performed to a combined spectrum of all detectors and all  
 275 calibration runs, ensuring that any variation in gain or energy nonlinearity between detectors is accounted for. From  
 276 each fit result, a set of parameters describing a single peak at the energy of the signal ROI can be extracted, along  
 277 with a covariance matrix for those parameters. From these fit results, we can compute the optimal ROI, detection  
 278 efficiency and uncertainty for each data set. An example of a calibration spectrum with the FWHM curve fit to it is



TABLE II Table of measured peak height ratios between multiplicity 1 events and multiplicity 2 events containing a 511 keV annihilation  $\gamma$  in module 1 for both simulated and measured  $^{56}\text{Co}$  spectra, with uncertainties. A plot of these numbers is shown in Figure 12

Peak	$\frac{A_{m2,\text{dat}}}{A_{m1,\text{dat}}}$	$\frac{A_{m2,\text{sim}}}{A_{m1,\text{sim}}}$	$\frac{A_{m2,\text{noDL}}}{A_{m1,\text{noDL}}}$	$\sigma_{\text{dat,stat}}$	$\sigma_{\text{sim,stat}}$	$\sigma_{\text{sim,DL}}$	Residual	$\sigma_{\text{resid}}$
1504 keV (SEP)	0.098	0.084	0.110	0.004	0.003	0.004	0.014	0.004
1524 keV (SEP)	0.089	0.082	0.109	0.002	0.001	0.005	0.007	0.002
2088 keV (SEP)	0.077	0.073	0.098	0.001	0.001	0.004	0.004	0.001
2499 keV (SEP)	0.081	0.079	0.108	0.003	0.002	0.005	0.002	0.004
2691 keV (SEP)	0.078	0.072	0.099	0.001	0.001	0.005	0.006	0.002
2743 keV (SEP)	0.075	0.073	0.101	0.001	0.001	0.005	0.003	0.001
2762 keV (SEP)	0.070	0.070	0.096	0.001	0.001	0.004	0.000	0.002
2940 keV (SEP)	0.075	0.070	0.100	0.002	0.002	0.005	0.005	0.003
749 keV (DEP)	0.153	0.155	0.225	0.004	0.003	0.012	-0.002	0.005
1013 keV (DEP)	0.166	0.156	0.229	0.005	0.004	0.012	0.010	0.006
1577 keV (DEP)	0.167	0.157	0.224	0.001	0.001	0.011	0.010	0.002
1988 keV (DEP)	0.158	0.155	0.222	0.005	0.005	0.011	0.003	0.007
2180 keV (DEP)	0.163	0.158	0.225	0.002	0.002	0.011	0.005	0.003
2232 keV (DEP)	0.164	0.158	0.225	0.001	0.001	0.012	0.007	0.002
2251 keV (DEP)	0.170	0.166	0.233	0.004	0.003	0.011	0.004	0.005
2429 keV (DEP)	0.165	0.158	0.230	0.005	0.004	0.012	0.007	0.007

TABLE III Table of measured peak height ratios between multiplicity 1 events and multiplicity 2 events containing a 511 keV annihilation  $\gamma$  in module 2 for both simulated and measured  $^{56}\text{Co}$  spectra, with uncertainties. A plot of these numbers is shown in Figure 12

Peak	$\frac{A_{m2,\text{dat}}}{A_{m1,\text{dat}}}$	$\frac{A_{m2,\text{sim}}}{A_{m1,\text{sim}}}$	$\frac{A_{m2,\text{noDL}}}{A_{m1,\text{noDL}}}$	$\sigma_{\text{dat,stat}}$	$\sigma_{\text{sim,stat}}$	$\sigma_{\text{sim,DL}}$	Residual	$\sigma_{\text{resid}}$
1504 keV (SEP)	0.077	0.059	0.082	0.004	0.002	0.004	0.018	0.004
1524 keV (SEP)	0.068	0.060	0.081	0.002	0.001	0.004	0.009	0.002
2088 keV (SEP)	0.059	0.054	0.074	0.001	0.000	0.003	0.005	0.001
2499 keV (SEP)	0.062	0.051	0.073	0.002	0.002	0.004	0.011	0.003
2691 keV (SEP)	0.057	0.052	0.074	0.001	0.001	0.004	0.005	0.002
2743 keV (SEP)	0.057	0.053	0.075	0.001	0.001	0.004	0.004	0.001
2762 keV (SEP)	0.055	0.050	0.071	0.002	0.001	0.004	0.005	0.002
2940 keV (SEP)	0.060	0.052	0.072	0.002	0.002	0.003	0.008	0.003
749 keV (DEP)	0.111	0.113	0.155	0.003	0.003	0.007	-0.002	0.004
1013 keV (DEP)	0.118	0.108	0.156	0.003	0.003	0.008	0.009	0.004
1577 keV (DEP)	0.119	0.113	0.161	0.001	0.001	0.008	0.006	0.001
1988 keV (DEP)	0.123	0.112	0.153	0.005	0.003	0.007	0.011	0.006
2180 keV (DEP)	0.119	0.114	0.164	0.002	0.002	0.008	0.005	0.002
2232 keV (DEP)	0.120	0.112	0.160	0.001	0.001	0.008	0.008	0.001
2251 keV (DEP)	0.124	0.120	0.170	0.003	0.003	0.008	0.004	0.004
2429 keV (DEP)	0.125	0.120	0.159	0.005	0.003	0.007	0.005	0.006

shown in Figure 13.

### A. Signal ROI Optimization

The signal region of interest around each peak is optimized based on the peak shape functions as fit for each data set. The optimization follows the procedure laid out in Appendix H and maximizes the rate sensitivity with respect to the region of interest upper and lower boundaries,  $E_{low}$  and  $E_{high}$  respectively:

$$\hat{\Gamma}(E_{low}, E_{high}, \bar{B}) \propto \frac{\text{DP}(\bar{B}(E_{high} - E_{low}))}{\epsilon_{ROI}(E_{low}, E_{high})} \quad (8)$$

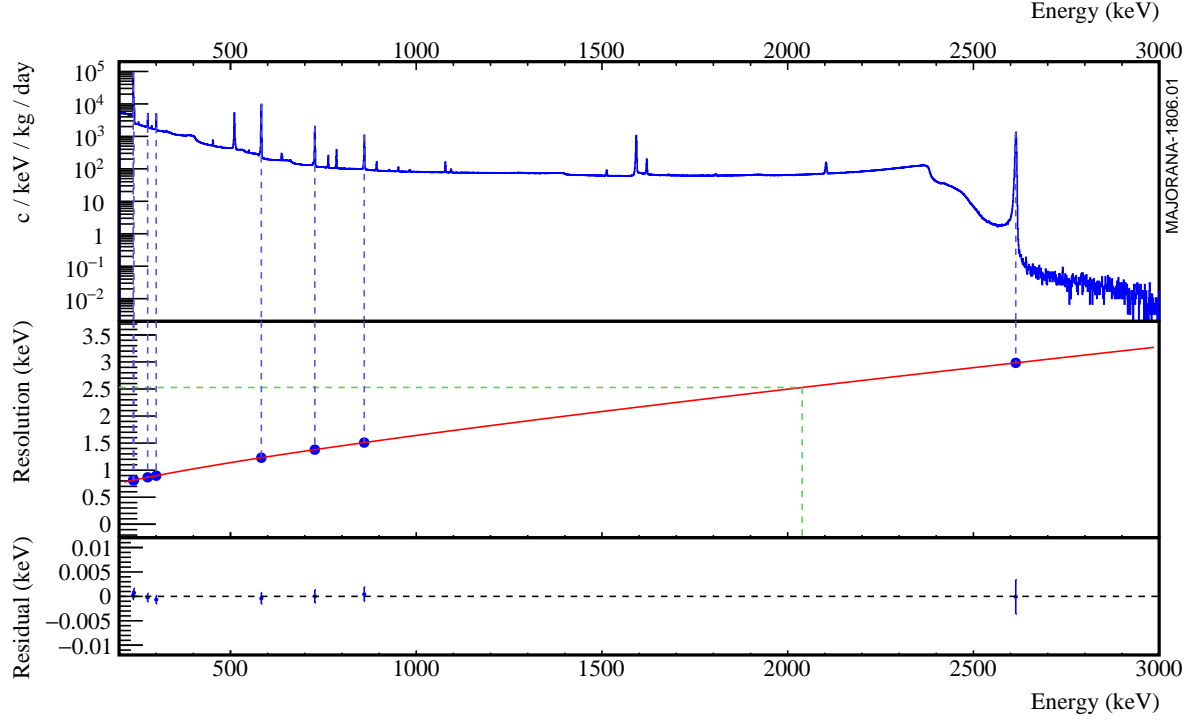


FIG. 13 A  $^{228}\text{Th}$  calibration run with the FWHM fit curve and individual uncertainties at several peaks. This curve is used to compute the FWHM for a peak at a given energy. The statistical uncertainties are extracted from the fit result. An additional systematic uncertainty is added to account for the residuals.

where DP is the discovery potential as defined in Appendix H, and a flat background with background index  $\bar{B}$  measured from data is assumed. The efficiency is defined by the CDF of the Gaussian and LE tail components

$$\epsilon_{ROI}(E_{low}, E_{high}; \mu, \sigma, f_{tail}, \tau) = \frac{1}{2} \left( \operatorname{erfc} \left( \frac{E_{low} - \mu}{\sqrt{2}\sigma} \right) - \operatorname{erfc} \left( \frac{E_{high} - \mu}{\sqrt{2}\sigma} \right) \right) + f_{tail}\tau \left( \operatorname{ExGaus}(E_{high}; \mu, \sigma, \tau) - \operatorname{ExGaus}(E_{low}; \mu, \sigma, \tau) \right) \quad (9)$$

The optimal ROI is numerically calculated by minimizing  $\frac{1}{\Gamma(E_{low}, E_{high}, \bar{B})}$  with respect to  $E_{low}$  and  $E_{high}$  using MINUIT[9].

## B. Background ROI Selection

For each peak, a background ROI of width 50 – 100 keV surrounding the peak is selected. The ROI is selected to avoid any known background peaks and exclude them with at least 99.9% efficiency. A 99.9% exclusion region calculated from the peakshape function is selected around the peak and removed from the background ROI.

## C. ROI Detection Efficiency and Uncertainty

The ROI detection efficiency is calculated from the CDF defined in Equation 9. The covariance matrix of the peak shape parameters obtained from the fit result is used to calculate the statistical uncertainty of the efficiency. Several additional systematic effects must also be accounted for:

- **Gain drift:**  $^{228}\text{Th}$  energy calibrations are taken once per week, for 90 minutes each. In between these calibration runs, the energy calibration parameters undergo small adjustments that result in energy inaccuracies for background runs taken in between. This gain drift results in an increase in the width of the peak, which is accounted for by adding in quadrature  $\sigma_{drift}$  to the value of  $\sigma$  obtained from the fit. This also results in the dominant systematic uncertainty on the peak width,  $\delta_{fwhm,drift}$ . The gain drift also results in a small



302 systematic error in the measured energy of the peak  $\delta_{\mu,drift}$ . A detailed description of the measurement of this  
303 systematic effect is contained in Reference [10].

304 • **Energy nonlinearity:** While the energy response for HPGe detectors is ostensibly linear, several factors result  
305 in small nonlinearities. Local nonlinearities that are correlated over small energy scales of arise from the response  
306 of the Gretina digitizers. While these nonlinearities are corrected for, a residual nonlinearity of  $\sim 0.1$  keV with a  
307 period of  $\sim 300$  keV remains. Global nonlinearities result from systematic uncertainties in the energy estimation.  
308 One source of global nonlinearity arises from uncertainty in the start time of the waveform, which is energy  
309 dependant. Another is a small quadratic term resulting from charge recombination. Because calibrations are  
310 performed on peaks with energies ranging from 238 keV to 2614 keV, energy shifts due to global nonlinearities  
311 are very small in this range and local energy nonlinearities dominate. At smaller and larger energies, the shifts  
312 can be as large as  $\sim 0.5$  keV in some detectors. In addition to this bias, energy nonlinearities result in an increase  
313 in  $\sigma$  as a result of the combining of peaks from different detectors with different shifts; however, since the energy  
314 calibrations include all detectors, this shift is already included in the fit result, so no action is required. Energy  
315 nonlinearities also have a significant affect on the uncertainty in the measured peak energy,  $\delta_{\mu,NL}$ , which is a  
316 dominant uncertainty. A detailed description of the measurement of each of these systematic effects is contained  
317 in Reference [10].

318 • **Detector Crosstalk:** Because we are searching for peaks in coincidence events, the possibility for a distortion  
319 in the energy measurement due to crosstalk between the involved events exists. This effect is measured in  
320 Section VII.D to be small enough that no energy correction or peakshape correction is required. However, this  
321 effect does contribute to small uncertainties in the peak position,  $\delta_{\mu,xtalk}$  and peak width,  $\delta_{fwhm,xtalk}$ .

322 Once these uncertainties have been measured, they must be propagated into the detection efficiency. The statistical  
323 and systematic uncertainties on  $\mu$  and the FWHM are added in quadrature to obtain  $\delta_\mu$  and  $\delta_{fwhm}$ . The uncertainty  
324 on the FWHM is used to calculate a width scale uncertainty,  $\delta_\alpha$ , which is simply the fractional uncertainty on the  
325 FWHM. To compute the uncertainty on the efficiency, the efficiency is computed after modifying the peakshape  
326 parameters by one-sigma in either direction. For the uncertainty from the width, we take:

$$\sigma_{\epsilon_{ROI,fwhm}} = \frac{1}{2} (\epsilon_{ROI}(E_{low}, E_{high}; \mu, \sigma(1 + \delta_\alpha), f_{LE}, \tau(1 + \delta_\alpha)) - \epsilon_{ROI}(E_{low}, E_{high}; \mu, \sigma(1 - \delta_\alpha), f_{LE}, \tau(1 - \delta_\alpha))) \quad (10)$$

327 Because the ROI is optimized around  $\mu$ , shifts in the peak in either direction will cause a reduction in efficiency. For  
328 this reason, we must perform a second order propagation of uncertainties with respect to  $\delta_\mu$ . The result is a slight  
329 degradation in the efficiency, so that

$$\epsilon_{ROI} = \frac{\epsilon_{ROI}(E_{low}, E_{high}; \mu + \delta_\mu, \sigma, f_{LE}, \tau) + \epsilon_{ROI}(E_{low}, E_{high}; \mu - \delta_\mu, \sigma, f_{LE}, \tau)}{2} \quad (11)$$

330 and

$$\sigma_{\epsilon_{ROI,\mu}} = \epsilon_{ROI}(E_{low}, E_{high}; \mu, \sigma, f_{LE}, \tau) - \epsilon_{ROI} \quad (12)$$

331 These uncertainties are taken to be uncorrelated and added in quadrature to obtain the final uncertainty on the ROI  
332 efficiency. Table XXVI contains a full summary of all of the energy uncertainties, the ROIs, and the ROI efficiencies  
333 and uncertainties.

#### 335 D. Detector Crosstalk

336 Detector crosstalk is caused when a true signal in one detector channel induces a small signal in another channel.  
337 This is not a large enough effect to trigger events in a separate channel, meaning that it does not effect single-detector  
338 events. However, it could produce an energy estimation error in multi-detector events since coincident pulses could  
339 induce signals that interfere either constructively or destructively, shifting the measured energies. In practice, this  
340 could produce both a shift and additional uncertainty in both the measured energy of the peak and in the width of  
341 the peak. To check for this effect, we can look at multi-detector events in  $^{228}\text{Th}$  calibration data. In particular, we  
342 will compare the centroid and FWHM for several peaks in both single-detector events and multi-detector events.

343 5 peaks were selected from the  $^{208}\text{Tl}$   $\gamma$  cascade, at 277, 583, 763, 860 and 2614 keV, and one additional peak  
344 was selected from the  $^{212}\text{Bi}$  cascade, at 785 keV. These peaks were selected based on their prominence in the high



TABLE IV Table of energy estimation uncertainties, regions of interest, and efficiencies

DS	$E_{peak}$ (keV)	$\sigma_{fit}$ (keV)	$\sigma_{drift}$ (keV)	$\sigma$ (keV)	$f_{t,fit}$ (keV)	$\tau_{fit}$ (keV)	$\delta_{\mu,fit}$ (keV)	$\delta_{\mu,NL}$ (keV)	$\delta_{\mu,drift}$ (keV)	$\delta_{\mu,peak}$ (keV)	$\delta_u$ (keV)	FWHM (keV)	$\delta_{fwhm,drift}$ (keV)	$\delta_{fwhm,fit}$ (keV)	$\delta_{fwhm,xtalk}$ (keV)	$\delta_{FWHM}$ (keV)	$\delta_\alpha$	$E_{ROI,1}$ (keV)	$E_{ROI,2}$ (keV)	$\epsilon_{ROI}$	$\sigma_{\epsilon_{ROI}}$	
DS1	559.101	0.460	0.063	0.464	0.230	0.515	0.001	0.104	0.002	0.012	0.005	0.105	1.152	0.001	0.039	0.011	0.040	0.035	558.199	559.847	0.871	0.015
DS2	559.101	0.461	0.055	0.464	0.249	0.515	0.002	0.067	0.004	0.012	0.005	0.068	1.158	0.001	0.107	0.011	0.108	0.093	558.186	559.845	0.874	0.031
DS3	559.101	0.470	0.066	0.474	0.224	0.505	0.001	0.026	0.024	0.012	0.005	0.038	1.174	0.001	0.073	0.011	0.074	0.063	558.187	559.863	0.879	0.021
DS4	559.101	0.455	0.077	0.461	0.108	0.445	0.002	0.076	0.010	0.012	0.005	0.078	1.111	0.001	0.106	0.011	0.107	0.096	558.283	559.856	0.888	0.032
DS5a	559.101	0.560	0.085	0.567	0.106	0.855	0.002	0.079	0.005	0.012	0.005	0.080	1.367	0.002	0.055	0.011	0.056	0.041	558.098	560.022	0.875	0.014
DS5b	559.101	0.469	0.074	0.475	0.158	0.491	0.001	0.020	0.011	0.012	0.005	0.026	1.157	0.001	0.125	0.011	0.125	0.108	558.229	559.872	0.885	0.036
DS5c	559.101	0.460	0.085	0.468	0.174	0.489	0.001	0.037	0.030	0.012	0.005	0.050	1.145	0.001	0.162	0.011	0.162	0.142	558.231	559.860	0.883	0.046
DS6a	559.101	0.456	0.044	0.458	0.191	0.463	0.001	0.069	0.025	0.012	0.005	0.075	1.123	0.000	0.041	0.011	0.042	0.038	558.241	559.841	0.881	0.014
DS1	563.178	0.461	0.064	0.466	0.230	0.518	0.001	0.104	0.002	0.012	0.005	0.105	1.156	0.001	0.039	0.011	0.040	0.035	562.273	563.927	0.871	0.015
DS2	563.178	0.463	0.055	0.466	0.249	0.517	0.002	0.067	0.004	0.012	0.005	0.068	1.162	0.001	0.107	0.011	0.108	0.093	562.259	563.924	0.874	0.030
DS3	563.178	0.471	0.066	0.476	0.224	0.508	0.001	0.026	0.024	0.012	0.005	0.038	1.179	0.001	0.073	0.011	0.074	0.063	562.261	563.943	0.879	0.021
DS4	563.178	0.457	0.077	0.463	0.108	0.447	0.002	0.076	0.010	0.012	0.005	0.078	1.115	0.001	0.106	0.011	0.107	0.096	562.357	563.935	0.888	0.032
DS5a	563.178	0.562	0.086	0.569	0.106	0.858	0.002	0.079	0.006	0.012	0.005	0.080	1.372	0.002	0.055	0.011	0.056	0.041	562.172	564.103	0.875	0.014
DS5b	563.178	0.471	0.074	0.477	0.158	0.494	0.001	0.020	0.011	0.012	0.005	0.026	1.162	0.001	0.125	0.011	0.125	0.108	562.303	563.952	0.885	0.035
DS5c	563.178	0.462	0.086	0.470	0.174	0.492	0.001	0.037	0.030	0.012	0.005	0.050	1.449	0.001	0.162	0.011	0.162	0.141	562.305	563.939	0.883	0.046
DS6a	563.178	0.457	0.044	0.459	0.191	0.465	0.001	0.069	0.026	0.012	0.005	0.075	1.127	0.000	0.041	0.011	0.042	0.038	562.315	563.921	0.881	0.013

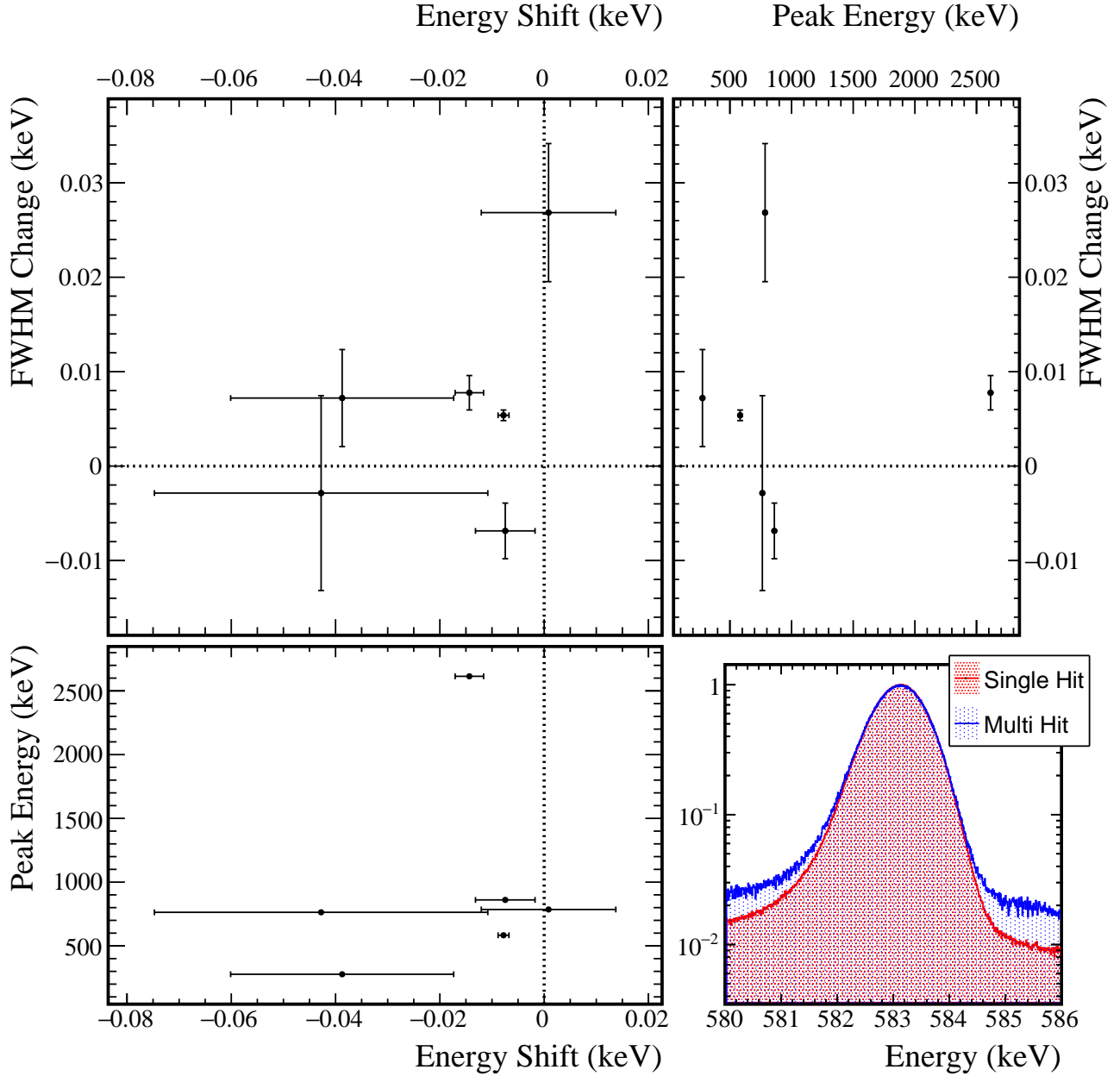


FIG. 14 Difference of the measured centroid and FWHM of several  $^{228}\text{Th}$  calibration peaks. Error bars represent the fit errors. Notice on the bottom right, that any difference is not visible to the naked eye.

346 multiplicity hit spectrum. The combined calibration spectra from dataset 6 were used to perform this analysis. These  
 347 peaks were fit individually, and the centroid and FWHM were computed for multiplicity 1 and multiplicity 2 events.  
 348 Figure 14 shows the results of these measurements. While a very small reduction in peak centroid and increase in  
 349 peak width are observed, the shifts are small compared to the existing uncertainties in these parameters. As a result,  
 350 we will ignore this shift and instead compute an uncertainty in each parameter caused by crosstalk. We will treat the  
 351 systematic error as uncorrelated between the peaks and compute the necessary error needed to make the combined  
 352 statistical and systematic errors large enough to make the  $\chi^2$  value computed by comparing these peaks equal to 1:

$$\chi^2 = \sum_{k=0}^N \frac{(cen_{k,m1} - cen_{k,m2})^2}{\sigma_{cen,k,m1}^2 + \sigma_{cen,k,m2}^2 + \delta_{\mu,xtalk}^2} \quad (13)$$



353

$$\chi^2 = \sum_{k=0}^N \frac{(\text{FWHM}_{k,m1} - \text{FWHM}_{k,m2})^2}{\sigma_{fwhm,k,m1}^2 + \sigma_{fwhm,k,m2}^2 + \delta_{fwhm,xtalk}^2} \quad (14)$$

354 Both systematic errors are numerically computed using a Brent minimization algorithm[11]. The results are  $\delta_{\mu,xtalk} =$   
 355  $0.012 \text{ keV}$  and  $\delta_{fwhm,xtalk} = 0.011 \text{ keV}$ , both of which are subdominant uncertainties.

356 **VIII. BACKGROUND CUTS**

357 By making use of known properties of background events, data cleaning cuts can be designed to selectively reduce  
 358 backgrounds while minimizing sacrifice of excited state events. Because of the multi-detector event nature of the event  
 359 selection, many of these background cuts are designed to make use of observables from the detector hits in coincidence  
 360 with candidate hits.

361 **A. Enriched Source Detector Cut**

362 Since the  $\beta\beta$  E.S. events must originate in  $^{76}\text{Ge}$ , events are far likelier to originate in enriched HPGe detectors  
 363 than those with natural germanium isotopic abundances. There are 29.8 kg of enriched detectors, with  $88.1 \pm 0.7\%$   
 364 abundance of  $^{76}\text{Ge}$  and 14.4 kg of natural detectors, with  $7.83 \pm 0.07\%$  abundance of  $^{76}\text{Ge}$ . This means that  $95.8 \pm 0.1\%$   
 365 of  $\beta\beta$  E.S. events will originate in enriched detectors. If we assume that background events will hit all detector mass  
 366 at the same rate, then we would expect only 67% of hits from background events involving two detectors to be in  
 367 coincidence with a hit in an enriched detector. This means that a significant gain in sensitivity can be achieved by  
 368 cutting hits that are not in coincidence with an enriched detector hit. While the detection efficiency of this cut is  
 369 expected to be close to 95.8%, the actual efficiency is measured from simulations, and tends to be greater, since a  
 370 greater proportion of enriched detectors are active compared to natural detectors.



FIG. 15 Diagram showing each detector in each module, arranged by which string and position they are in. Enriched detectors are colored green and natural detectors are colored blue. 95% of  $^{76}\text{Ge}$  in the array is contained in the enriched detectors.

371 **B. Coincident and Sum Energy Cuts**

372 The greatest source of background events is expected to be  $\gamma$ -rays from a handful of known primordial and cos-  
 373 mogenic isotopes. Because  $\gamma$ -rays are monoenergetic, they will often present a clear detection signature that can be  
 374 targeted.  $\gamma$ -rays will often Compton scatter from one detector into another, depositing their entire energy between  
 375 the two. For this reason, events whose total energy is equal to the energy of a known  $\gamma$  can be cut.  $\beta$ -decays will  
 376 often result in a cascade of multiple  $\gamma$ s, at least one of which may be fully absorbed in a single detector. These events  
 377 can be cut by searching for a coincident detector with energy equal to that of a known  $\gamma$ . Finally, whereas the  $\beta\beta$   
 378 decay spectrum approaches zero amplitude at low energies and at  $Q_{\beta\beta}$ , the Compton continuum of  $\gamma$ s has a large  
 379 amplitude at low energies. This means that sensitivity can be gained by setting low- and high-energy thresholds on  
 380 hits in coincidence with a candidate event. These combined backgrounds can be reduced by cutting events with either



sum energies or coincident hit energies that fall in a set of energy ranges. For  $\beta\beta$  E.S. modes with multiple  $\gamma$ s, the optimal energy ranges will differ between natural and enriched detectors, since natural detectors will mostly include hits from one of the  $\gamma$ s, while enriched events will include  $\beta\beta$  hits,  $\gamma$  hits, and pileup events including both of these, allowing a much wider energy range. For this reason, a separate set of coincident cut energy ranges are used for natural and enriched detectors.

The energy ranges that are cut can be determined by comparing the background model simulation to simulations of each  $\beta\beta$  E.S. decay mode. An algorithm was written that simultaneously selects a set of both sum and coincident energy ranges to cut that optimizes discovery potential, as defined in Appendix H. The algorithm begins by identifying events in the  $\beta\beta$  E.S. simulation that include at least one hit consisting of the full absorption of a  $\gamma$  photon and events in the background model simulation that include at least one hit in the background region of interest. These events are then sorted into energy bins for each coincident hit and for the sum energy of the event (a single event will be in multiple bins). For each bin, the algorithm checks the change in discovery potential if the bin was toggled to be either cut or included. Following Equation H10, the discovery potential will be improved by toggling bin  $k$  if:

$$\text{DP}'(s \cdot N_{BG}) \frac{s \cdot n_{k,BG}}{\text{DP}(s \cdot N_{BG})} < \frac{n_{k,ES}}{N_{ES}} \quad (15)$$

where  $N_{ES}$  and  $N_{BG}$  are the total number of events remaining in the simulated  $\beta\beta$  E.S. and background spectra, respectively;  $s$  is a scaling to estimate the number of background events in the data from the number in the simulation; and  $n_{k,ES}$  and  $n_{k,BG}$  are the number of simulated  $\beta\beta$  E.S. and background events contained in the bin. A  $\chi$  value is computed representing the normal quantile of the probability that cutting or including the bin will improve the discovery potential. This is done by assuming that the uncertainty on the number of events in the bin is Gaussian distributed, with standard deviations  $\sqrt{n_{k,ES}}$  and  $\sqrt{n_{k,BG}}$ , respectively. In this case, we get:

$$\chi_k = \frac{\frac{n_{k,ES}}{N_{ES}} - \text{DP}'(s \cdot N_{BG}) \frac{s \cdot n_{k,BG}}{\text{DP}(s \cdot N_{BG})}}{\sqrt{\left(\text{DP}'(s \cdot N_{BG}) \frac{s}{\text{DP}(s \cdot N_{BG})}\right)^2 n_{k,BG} + \frac{n_{k,ES}}{N_{ES}^2}}} \quad (16)$$

All events in the bin with highest probability of improving the discovery potential are then either cut or included, and must be cut or included to all other bins that they fall into. Note that a included event will only be included if it is not cut by any other bin. This process is repeated until toggling any bin will have  $\chi_k < 0$ , meaning there is a  $< 50\%$  chance of improving the discovery potential. At this point, the bins are then combined in order to determine the ranges of energies to be cut in sum energy and coincident energies.

Because of limited statistics in the simulations, this cut will be biased to cut events in bins with a downward fluctuation in  $\beta\beta$  E.S. rate and accept bins with an upward fluctuation, and vice-versa for the simulated background model. In order to minimize this bias and ensure that energy ranges are selected based on real backgrounds rather than statistical fluctuations, a penalty is applied to the probability calculations if a new range would be added. If cutting or readding a bin would increase the number of energy ranges, a penalty of 3 is added to the  $\chi$  value, and if it would reduce the number of ranges, a penalty of -3 is added. This corresponds to requiring a 99.8% chance that adding a new energy range will represent an improvement before we conclude that it is not a statistical fluctuation. This is inspired by the Akaike Information Criterion (AIC)[12], which adds a penalty of 1 to a likelihood for each parameter added to a model. In this case, adding an energy range adds two parameters to our cut, so the equivalent penalty is 1.5 per parameter, which is a larger penalty than AIC. This difference can be explained by the fact that the AIC penalty of 1 requires 97.7% that toggling a bin represents an improvement; however, it has been observed that  $\sim 100$  bins exist close enough to the threshold for inclusion or exclusion to accidentally toggle the bin. As a result, using a penalty of 1 will result in multiple accidentally excluded energy regions, on average, while a penalty of 1.5 will not.

To further control limited simulation statistics, a variety of bin widths is used to determine the optimal energy ranges. This is necessary because with a narrow binning, bins do not have enough statistics to overcome the penalty described above, but wider bins produce very imprecise energy ranges. The algorithm starts by optimizing the cut ranges with a bin width of 6.4 keV starting from a prior of cutting no energy ranges. Once this optimization is complete, the bin width is split in half and the algorithm re-optimizes the energy ranges, using the previous ranges as a prior. This halving of bin width is repeated until a final bin width of 0.2 keV is reached. The results of this cut optimization procedure are shown in figures 16 and 17.

The efficiency of each of the sum and coincident energy cuts can be evaluated by computing the ratio of simulated  $\beta\beta$  E.S. events that pass the cut to the total number of simulated events. The primary source of uncertainty arises from imperfections in the simulated  $\beta\beta$  E.S. spectra produced by DECAYO (see Section II). Additionally uncertainty in

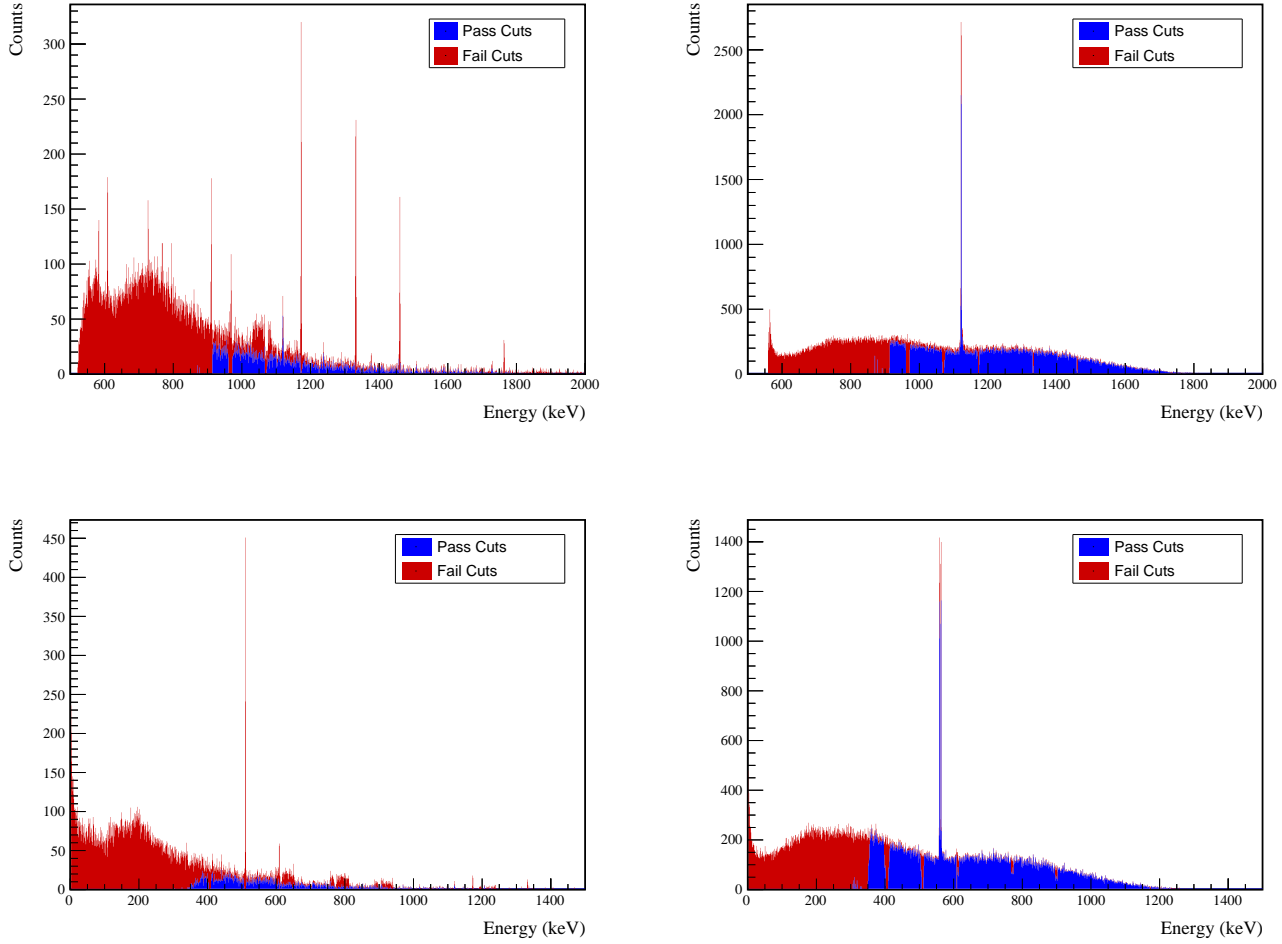


FIG. 16 Top: Simulated sum energy spectra of simulated ES and BG events. The events in red are cut by the sum- or coincident-energy cut. Note that regions around many peaks are cut, as intended.  
Bottom: Simulated energy spectrum of events in coincidence with events in the ROI. Excesses in red are cut by the sum- or coincident-energy cut. Once again, regions around prominent peaks are cut out as intended.

the spectral shape arises from energy nonlinearity. Since the efficiency is calculated by integrating over portions of the coincidence spectrum, an upper limit on the systematic error can be found using the KS statistic of a comparison between the simulated spectrum and the true spectrum. As discussed in Section II.A, we can perform this comparison by using the Kotila and Iachello spectrum as a proxy. This relies on the assumption that the Kotila and Iachello spectrum has corrected the dominant errors in the DECAY0 spectrum; if any errors coexist in both spectra that have a similar order of magnitude, then this approach will underestimate the uncertainty. To account for energy nonlinearity, each simulated energy is shifted to represent the effects of digitizer nonlinearity and energy drift. Digitizer nonlinearity originates from the fact that some digitizer energy bins are slightly wider than others and has an approximately sawtooth dependency on energy with a period of  $\sim 600$  keV. A correction is applied that reduces the size of this nonlinearity to  $\sim 0.1$  keV in magnitude and smooths it out significantly, as shown in Figure 18. Digitizer nonlinearity is included in the simulation by shifting each energy according to a sawtooth function with rms 0.1 keV and period 600 keV:

$$\Delta(E) = \sqrt{3} \cdot (0.1 \text{ keV}) \left( \text{rem}\left(\frac{E - 150 \text{ keV}}{600 \text{ keV}}\right) \right) \quad (17)$$

where `rem` is the remainder function as defined in the C++ standard library. An additional shift that is randomly sampled from a Gaussian distribution with standard deviation  $0.00015 \cdot E$  is applied to simulate the effect of gain drift, based on the drift observed during DS5. After applying both of these alterations to the DECAY0 spectrum, a KS

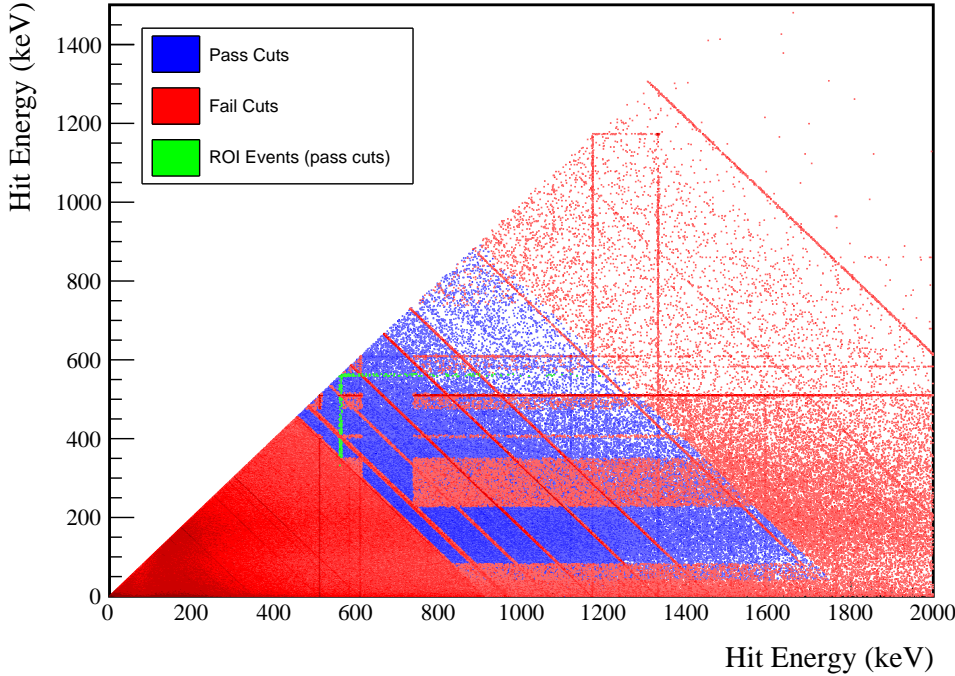


FIG. 17 2D energy spectrum of simulated BG events. Blue bins have at least one hit that passes both the sum- or coincident-energy cuts. For red bins, both hits have failed at least one of these cuts. Green bins have at least one hit in the BG or ES ROI that passes these cuts.

444 test is performed against the Kotila and Iachello spectrum, and a maximum CDF difference of 0.08% is observed, as  
 445 shown in Figure 19. This difference is used as an upper limit on the uncertainty from the energy range cuts for  $2\nu\beta\beta$   
 446 modes.

448 For  $0\nu\beta\beta$ , the energy ranges selected by this cut surround peaks corresponding to the  $Q_{\beta\beta}$ s of the decay modes or  
 449 sum peaks of the  $Q_{\beta\beta}$  with a deexcitation  $\gamma$ . In this case, since we are no longer integrating over a  $\beta\beta$ -spectrum, the  
 450 uncertainty in the efficiency will depend on shifts in the peak, similar to the ROI-efficiency. Since the energy regions  
 451 selected keep at least 99.9% of these peaks in all cases, we can set an upper limit on the uncertainty by checking  
 452 the ROI efficiency uncertainty around the 2039 keV  $Q_{\beta\beta}$ , assuming an ROI tuned to select 99.9% of the peak. The  
 453 uncertainty observed in this case is 0.325%, which is applied to the energy range cuts for  $0\nu\beta\beta$  modes. For both  $0\nu\beta\beta$   
 454 and  $2\nu\beta\beta$  modes, this efficiency uncertainty is sub-dominant, so these highly conservative uncertainty estimates will  
 455 suffice.

### 456 C. Muon Veto Cut

457 Cosmic ray muons have the potential to produce particle showers in the MAJORANA DEMONSTRATOR that can  
 458 produce multi-site event events and can activate short-lived isotopes that in turn may decay, producing delayed multi-  
 459 site event events. Background events caused by muons can be cut using the muon veto system. This analysis follows  
 460 the standard MAJORANA DEMONSTRATOR muon cut procedure, for which any HPGe detector events occurring 20 ms  
 461 before and 1 s after a tagged muon event are cut. This cut will remove > 99.9% of events induced by the muon shower,  
 462 based on simulations[13]. In reality, the cut efficiency is slightly lower due to periods of time where the muon veto  
 463 system clock became desynchronized with the Germanium detector clock. The impact of this cut is to reduce the  
 464 total livetime in each module by < 40 s per day[13].

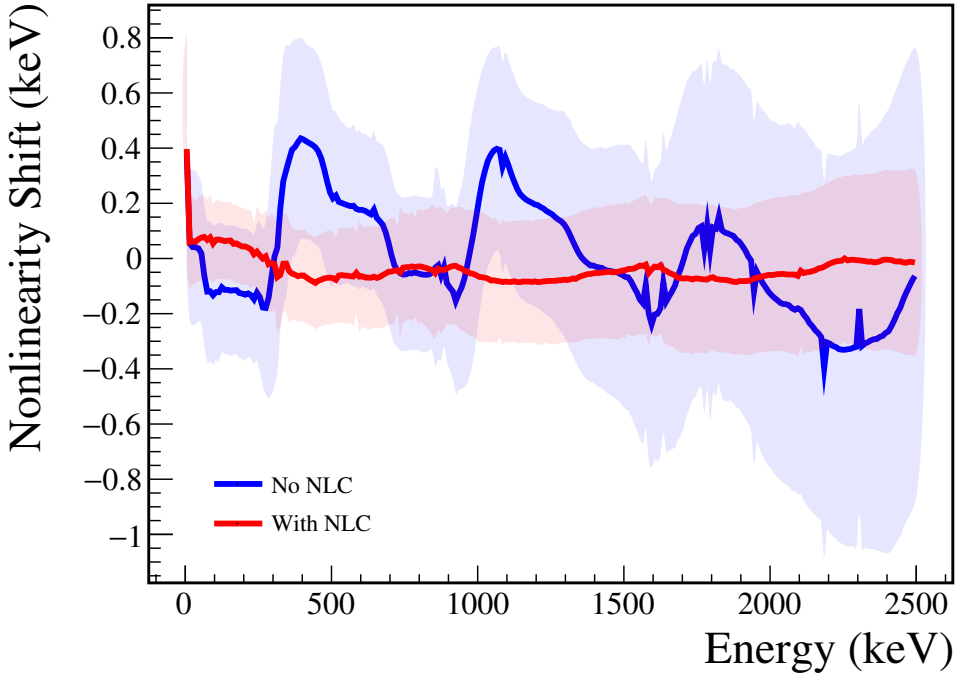


FIG. 18 Digitizer nonlinearity before (red) and after (blue) being corrected. This nonlinearity is measured by comparing the energy measured in the high gain channel to that of the low gain channel.

## 465 IX. COMBINED DETECTION EFFICIENCY FOR $\beta\beta$ E.S.

466 The final efficiency measurement combining all of the effects described in this chapter for each  $\beta\beta$  E.S. mode is  
 467 measured directly from the simulations by computing the ratio of events that survive all cuts and effects to the  
 468 total number of generated events. The efficiency used is the exposure-weighted average of the simulated efficiency  
 469 for each subdataset. Because each module is an independent measurement, separate efficiencies are measured for  
 470 modules 1 and 2. Because of correlations causing the probability of certain effects causing sacrifice of a  $\beta\beta$  E.S. event  
 471 to be conditional on other effects, the combined efficiency will differ from simply being the product of the individual  
 472 efficiencies. This means that the combined efficiency  $\epsilon_{comb}$  for each effect  $k$  is:

$$\epsilon_{comb} = \prod_{k=0}^N P(\text{event is cut} | \text{cuts } 0 \dots k-1 \text{ are applied}) \quad (18)$$

473 In spite of this, we will assume that the sources of error are uncorrelated and the fractional uncertainty is independent  
 474 of what other effects have been applied. The effect of this assumption will be discussed below. This implies that the  
 475 uncertainty on the combined efficiency,  $\sigma_{\epsilon,comb}$  can be expressed as:

$$\sigma_{\epsilon,comb} = \epsilon_{comb} \sqrt{\sum_{k=0}^N N \left( \frac{\sigma_{\epsilon,k}}{\epsilon_k} \right)^2} \quad (19)$$

476 The values  $\epsilon_k$  represent the probability of cutting an event assuming no other analysis cuts are applied. Because  
 477 of correlations among the cuts (particularly between the sum and coincident energy cuts), this results in a double-  
 478 counting of uncertainty, making this a conservative estimate.

479 Table V shows the efficiency for each effect described in this chapter and uncertainty on each efficiency, and the  
 480 combined efficiency and uncertainty. Similar tables for each other  $\beta\beta$  E.S. peak are shown in Appendix A. In all cases  
 482 the dominant uncertainties come from either the dead layer thickness or the simulation uncertainty. Figure 21 shows  
 483 the effect of each cut as it is applied sequentially to the  $2\nu\beta\beta$  to  $0_1^+$  peaks.

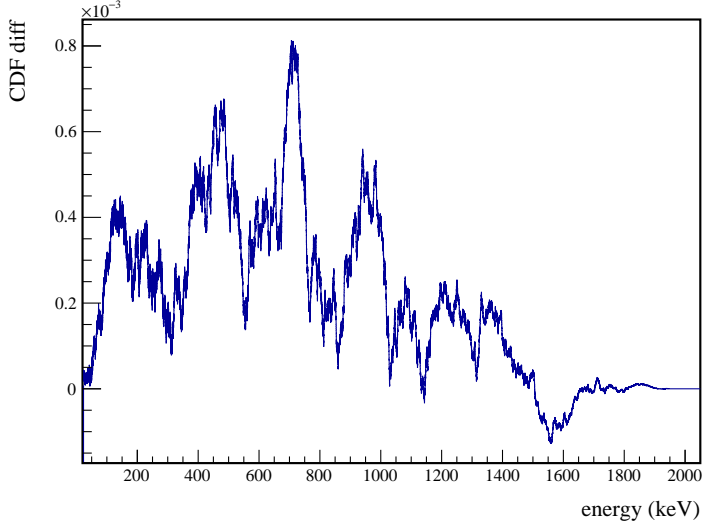


FIG. 19 KS test comparing the CDFs of the simulated DECAY0  $2\nu\beta\beta$  ground state decay with energy nonlinearity modifications applied to the Kotila and Iachello simulated spectrum.

Source	Module 1 efficiency	Module 2 efficiency
Multi-Detector with Full Energy $\gamma$	$5.9 \pm 0.2\%$	$3.2 \pm 0.5\%$
Region of Interest	$87.9 \pm 1.4\%$	$87.9 \pm 1.4\%$
Dead Layer	$74.5 \pm 4.3\%$	$65.7 \pm 6.0\%$
Detector Dead Times	$97.5 \pm 1.2\%$	$98.1 \pm 0.9\%$
Enriched Source Detector Cut	$96.8 \pm <0.1\%$	$89.4 \pm <0.1\%$
Coincident Energy Cut	$88.5 \pm 0.5\%$	$84.4 \pm 0.5\%$
Sum Energy Cut	$60.2 \pm 0.5\%$	$54.0 \pm 0.5\%$
Final Efficiency	$2.29 \pm 0.16\%$	$0.97 \pm 0.17\%$

TABLE V Table of detection efficiencies and uncertainties for  $2\nu\beta\beta$  of  $^{76}\text{Ge}$  to the  $0_1^+$  state of  $^{76}\text{Se}$ . Efficiencies of individual effects are calculated without applying other cuts; because of correlations between cuts (especially the sum and coincident energy cuts), simply multiplying these efficiencies together will underestimate the efficiency. The final efficiency calculated here correctly accounts for such correlations. Note that the efficiencies are the combined efficiency for the 559 and 563 keV peaks.

## 485 X. DOUBLE BETA DECAY TO EXCITED STATES RESULTS

486 Now that we have found and characterized a specific detection signature for each decay mode, we can apply this  
 487 search to data. This result will look at open and blind runs from datasets 1 through 6a that were designated silver or  
 488 gold in run quality. The duty cycle and changes that define each data set are shown in Figure 22. These were taken  
 489 from January 12, 2016 to April 18, 2018, and contain a total of 49.1 kg y of isotopic exposure. Approximately half  
 490 the data in these datasets is blinded, and was not included in initial results. The MAJORANA DEMONSTRATOR uses  
 491 a statistical blinding scheme in which 3/4 of runs are blinded administratively (i.e. through file access) in cycles of  
 492 31 h of unblinded runs followed by 93 h of blinded runs. Unblinding data proceeds in a staged fashion, where first  
 493 single-site events, not including any interesting physics regions are unblinded (i.e. no background ROI,  $0\nu\beta\beta$  to the  
 494 ground state ROI, low energy or multi-site data). This data is used for a variety of data validation checks prior to  
 495 unblinding of any other data. The remaining data are separately unblinded after a collaboration review for individual  
 496 analyses and users.

497 9606 multi-detector events were observed. A histogram of the event multiplicities is shown in Figure 23, and a  
 498 spectrum of all multiplicity 2 event energies is shown in Figure 24.

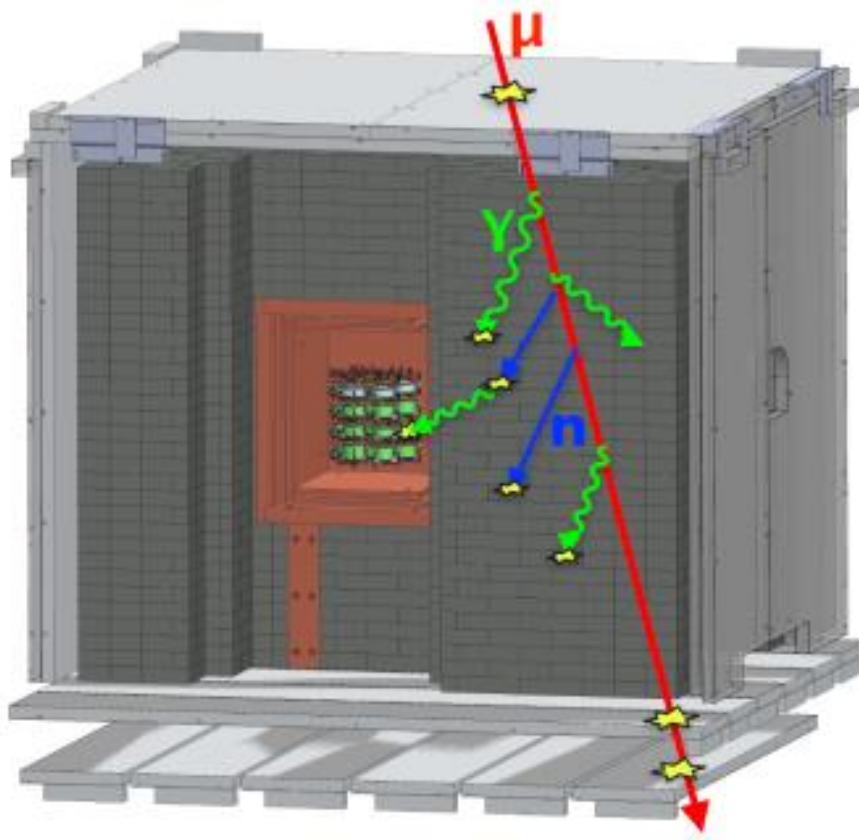


FIG. 20 A cartoon of a particle shower created by a muon event. The particles produced in such a shower can hit multiple detectors, producing multi-detector events.

## 501 XI. VALIDATION

502 In addition to the basic run selection and data cleaning validation checks that are run on all multiplicity 1 data,  
 503 we perform some additional checks on high multiplicity data. As previously, this section will describe these checks  
 504 applied to the  $2\nu\beta\beta$  to the  $0_1^+$  state of  $^{76}\text{Se}$ . Similar checks are performed on other decay modes in Appendix A.

### 505 A. Data Rate

506 Any spikes in the rate of multi-site events would potentially indicate problems with run selection or data cleaning.  
 507 Significant variation in the data rate is expected due to changes in which detectors are active. For this reason, the  
 508 rate of multi-site events with respect to the sensitive exposure, defined as the exposure times the detection efficiency  
 509 of  $\beta\beta$  E.S. events, is used instead. This quantity is interesting because the rate of observed  $\beta\beta$  E.S. events should be  
 510 constant with respect to it. The changes in detection efficiency from one subdataset to another for both backgrounds  
 511 and  $\beta\beta$  E.S. are highly correlated and driven by which detectors are enabled. For this reason, we can reasonably expect  
 512 that the backgrounds should also have a nearly constant rate with respect to sensitive exposure, although differences  
 513 between background source positions and the distribution of  $^{76}\text{Ge}$  in the detectors imply that some differences should  
 514 be expected. Figure 25 shows changes in rate consistent with changes in which detectors are enabled. In particular,  
 515 enabling or disabling a natural detector can cause a large change in the background rate relative to sensitive exposure,  
 516 since natural detector events largely do not contribute to detection efficiency.

### 518 B. Background Cut Evaluation

519 A second important check to ensure that the cuts applied to each  $\beta\beta$  E.S. mode is to compare each cut efficiency to  
 520 the expected background cut efficiency. Since the background model used for this analysis uses preliminary results,

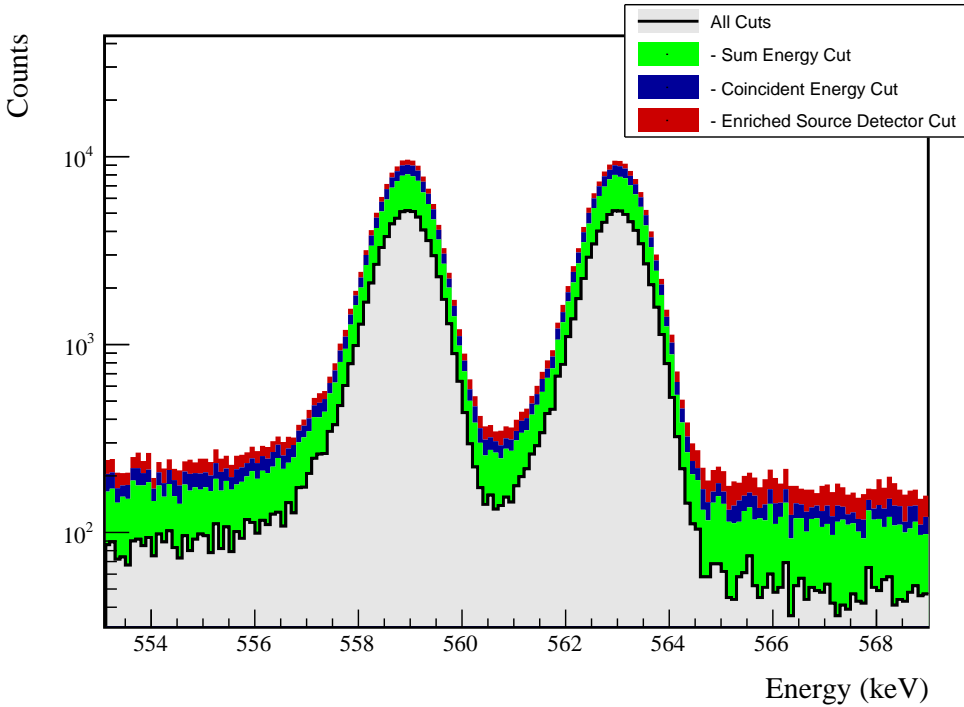


FIG. 21 The 559 and 563 keV peaks from the  $2\nu\beta\beta$  decay to the  $0_1^+$  decay mode, with the effect of all cuts applied sequentially to simulated ES events. The cuts are applied from top to bottom (i.e. red, blue, then green). Many events will be cut by more than one of these; in that case it will be colored by whichever cut is applied first.

disagreement between the expected and measured cut efficiencies could indicate a difference between the background model and the measured backgrounds rather than a problem with the application of cuts. However, any major discrepancies could indicate a bug in the analysis. To perform this comparison, the cut efficiencies are measured both in terms of the total number of events cut,  $\epsilon_{total}$  and the number of events that are uniquely cut,  $\epsilon_{unique}$  (i.e. not cut by any of the others). Table VI lists each cut for the  $\beta\beta$  E.S. decay to the  $0_1^+$  state and the expected and measured cut efficiencies. The expected background cut efficiencies,  $\langle \epsilon \rangle$  represent the fraction of simulated events cut, measured as an exposure-weighted average across all open datasets. The measured background cut efficiencies,  $\hat{\epsilon}$  represent the measured fraction of events cut. Statistical uncertainties in the expected efficiencies are negligible compared to the uncertainties in the measured efficiencies, and are not included. The sacrifice is the number of events uniquely sacrificed by the cut.  $\Delta DP$  is the expected improvement in discovery potential, defined in Appendix H, as a result of the cut. Figure 26 shows the effects of data cuts on multiplicity 2 events. Figure 27 shows the effects of cuts on events in the ROI in both measured and simulated data.

## 533 XII. RESULTS

### 534 A. Statistical Methods

Neyman confidence intervals are computed for each peak in each  $\beta\beta$  E.S. decay mode, and each module. For a given peak  $k$ , the expected number of signal counts is

$$\langle s_k \rangle = \ln 2 \frac{N_A}{m_{76}} \epsilon_k \frac{M_{iso} T_{live}}{T_{1/2}} \quad (20)$$

where  $M_{iso}$  is the total isotopic mass and  $T_{live}$  is the livetime ( $M_{iso} T_{live}$  is the exposure and is calculated in Section VI.A to be  $13.356 \pm 0.021$  kg-y for module 1 and  $7.872 \pm 0.13$  kg-y for module 2.  $\epsilon_k$  is the total detection efficiency of the decay mode using peak  $k$ , which can be found in Appendix A.  $m_{76} = 0.0759214$  kg is the molar mass of  $^{76}\text{Ge}$ ,



Cut Name	Cut Description	$\langle \epsilon_{total} \rangle$	$\hat{\epsilon}_{total}$	$\langle \epsilon_{unique} \rangle$	$\hat{\epsilon}_{unique}$	Sacrifice	$\Delta IDP$
Enriched Source	Any other detector: 1:sBar	M1: 21.5 %	23.3 <sup>+2.7</sup> <sub>-2.5</sub> %	3.2 %	2.3 <sup>+1.1</sup> <sub>-0.7</sub> %	1.0 %	9%
Detector Cut	No other detector: ((energy<40.8)    (energy>403.4 && energy<409.2)    (energy>509.2 && energy<512.2)    (energy>608.6 && energy<611.4)    (energy>170.6 && energy<175.6)    (energy>1204.2 && energy<1208.2)    (energy>1259.2) && isbar)    ((energy<42.2)    (energy>497.6 && energy<522.)    (energy>563.8 && energy<10.6)    (energy>903.2) && 1:sBar)    (sumE<852.2)    (sumE>853. && sumE<855.4)    (sumE>855.6 && sumE<877.8)    (sumE>978. && sumE<991.)    (sumE>906.8 && sumE<912.4)    (sumE>961.8 && sumE>971.8)    (sumE>1169.8 && sumE>1174.6)    (sumE>1330. && sumE<1535.6)    (sumE>1458. && sumE>1462.2)    (sumE>1761.8 && sumE<1771.)    (sumE>1824.6))	M2: 40.5 %	63.8 <sup>+6.0</sup> <sub>-6.5</sub> %	6.7 %	12.1 <sup>+4.9</sup> <sub>-3.6</sub> %	2.9 %	9%
Coincident Energy Cut		M1: 20.6 %	21.8 <sup>+2.6</sup> <sub>-2.4</sub> %	3.5 %	1.9 <sup>+1.0</sup> <sub>-0.7</sub> %	2.8 %	5%
Sum Energy Cut		M2: 22.9 %	31.0 <sup>+6.4</sup> <sub>-5.7</sub> %	3.2 %	1.7 <sup>+2.7</sup> <sub>-1.1</sub> %	2.1 %	
Combined Cuts							
		M1: 81.6 %	80.8 <sup>+2.3</sup> <sub>-2.5</sub> %	—	—	41.0 %	29%
		M2: 86.9 %	89.7 <sup>+3.3</sup> <sub>-4.7</sub> %	—	—	49.0 %	

TABLE VI Table of detection efficiencies and uncertainties for  $2\nu\beta\beta$  of  $^{76}\text{Ge}$  to the  $0_1^+$  state of  $^{76}\text{Se}$ .

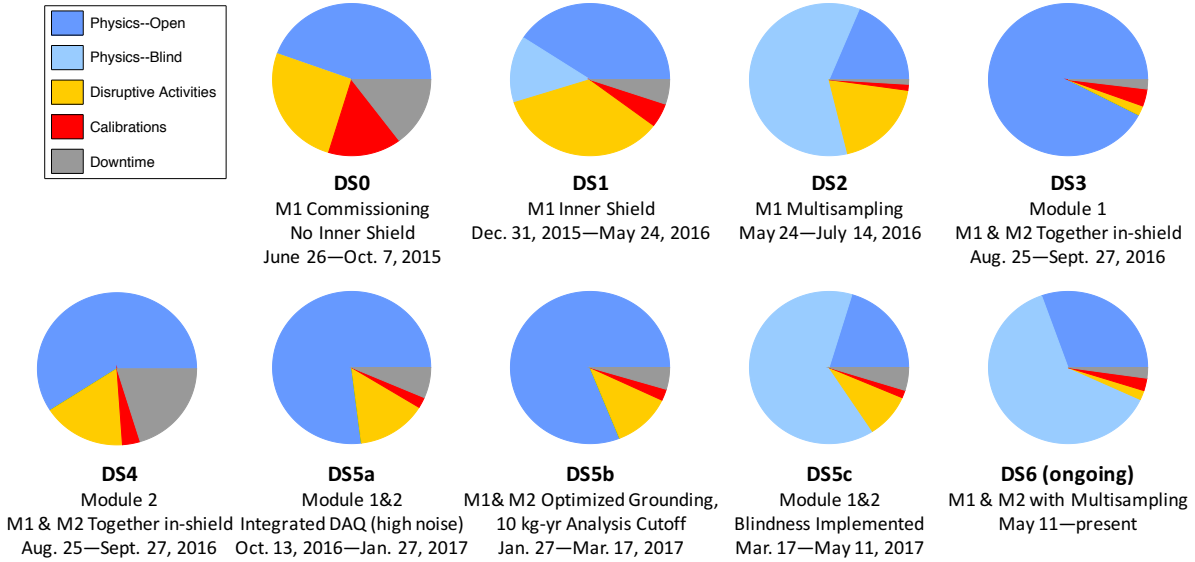


FIG. 22 The duty cycles for each major dataset used in this analysis, and a brief description of the major changes in configuration that define each data set.

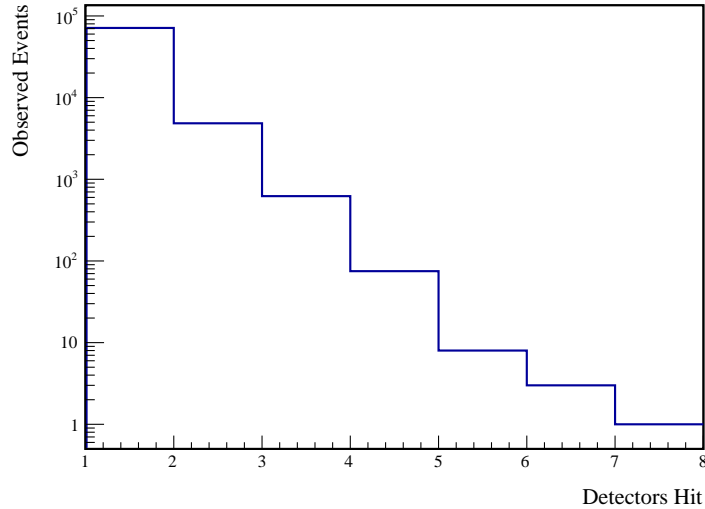


FIG. 23 The measured multiplicities for events in datasets 1-6a. For multiplicity 1 events, only events with energy between 40 keV and 4 MeV were considered.

and  $N_A = 6.02214076 \times 10^{23}$  is Avagadro's number. Fun fact: an Avagadro's number of avocados has approximately the volume of Mars. We will define the single count half-life to be

$$T_k^* = \ln 2 \frac{N_A}{m_{76}} \epsilon_k M_{iso} T_{live} \quad (21)$$

which is the decay half-life that would produce on average one count in signal ROI  $k$ .

Because of the nearly background free nature of this search, a likelihood construction is used that assumes Poisson

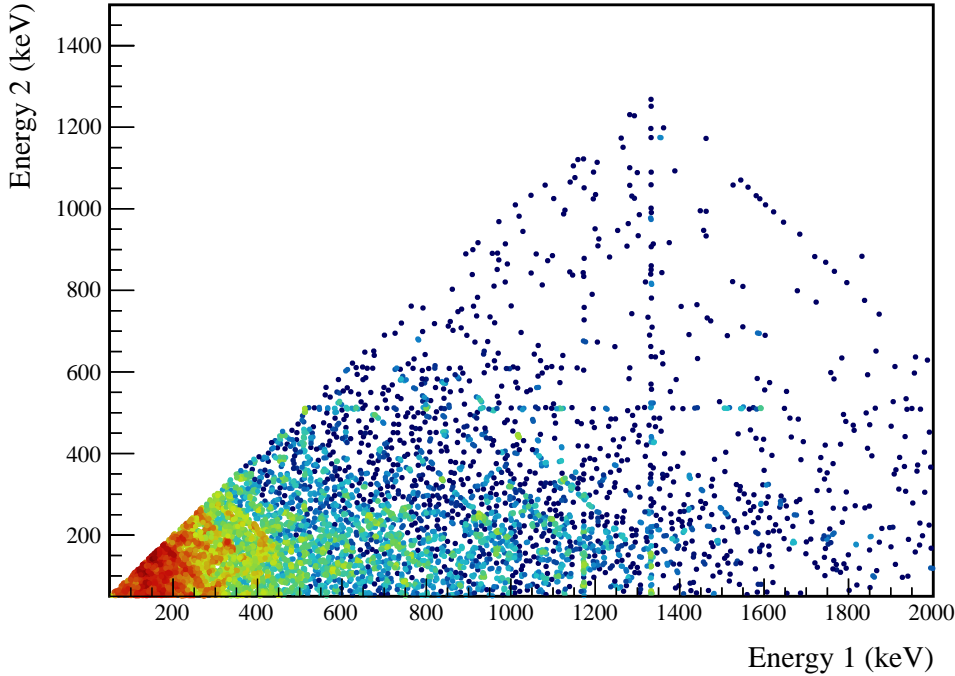
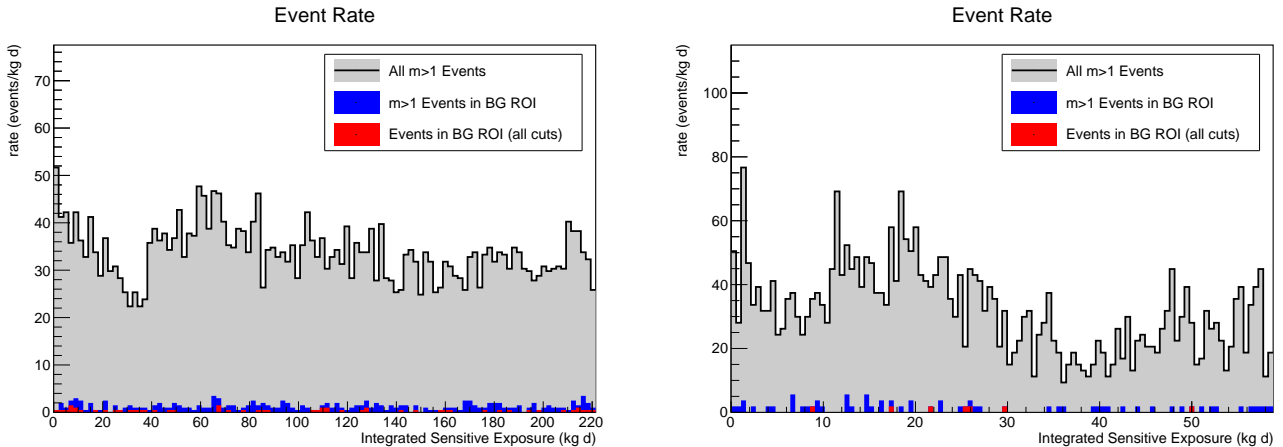


FIG. 24 Measured energy spectrum of open multiplicity 2 events in datasets 1-6a.

FIG. 25 Event rate with respect to sensitive exposure, or the detection efficiency of the  $2\nu\beta\beta$  decay to the  $0_1^+$  excited state times the exposure. Integrated exposure is the total sensitive exposure prior to an event. The background rate is expected to be mostly flat, with differences discussed in Section XI.A.

544 statistics for the number of counts in the signal and background ROIs.

$$\begin{aligned} \mathcal{L}_k(T_{1/2}, T_k^*, b_k | n_k, m_k, \langle T_k^* \rangle, \sigma_{T^*,k}, \tau) &= \frac{\mu_k^{n_k} e^{-\mu_k}}{n_k!} \cdot \frac{(b_k \tau)^{m_k} e^{-b_k/\tau}}{m_k!} \cdot \frac{1}{\sigma_{T^*,k} \sqrt{2\pi}} e^{-\frac{(T_k^* - \langle T_k^* \rangle)^2}{2\sigma_{T^*,k}^2}} \\ \mu_k &= s_k + b_k = \frac{T_k^*}{T_{1/2}} + b_k \end{aligned} \quad (22)$$

545  $T_{1/2}$  represents the decay mode half-life and is the parameter of interest.  $T_k^*$  and  $b_k$  are nuisance parameters rep-

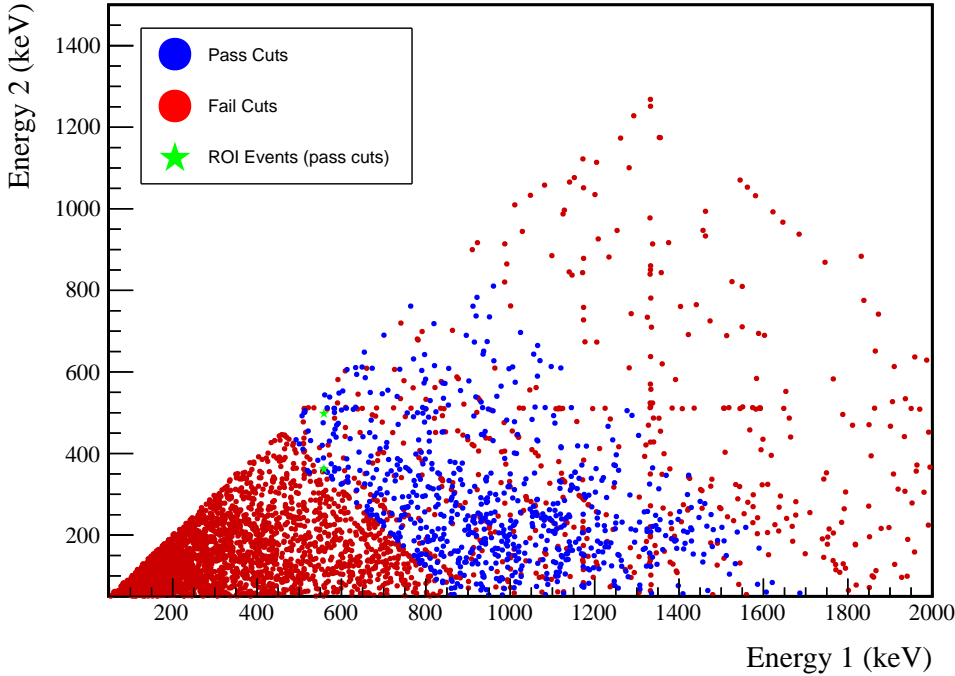


FIG. 26 Energy spectrum of multiplicity 2 events. Red events are events that are cut. For blue events, at least one of the hits passes all cuts; however, the other hit may fail. For green events, one of the hits must both pass all cuts and place the event in the BG or ES ROI. Note that the green events include any events of multiplicity > 1; for higher multiplicity events, instead of showing the energy in the second detector, the sum of the energy in all other detectors is shown.

resenting the measured single count halflife and expected backgrounds in the ES ROI, respectively.  $\mu_k$  is the total expected number of counts, combining background and signal, in the ES ROI.  $n_k$  is the measured number of events in the ES ROI and is expected to be drawn from a Poisson distribution with mean  $\mu_k$ .  $m_k$  is the measured number of events in the BG ROI and is expected to be drawn from a Poisson distribution with mean  $b_k/\tau$ , where  $\tau$  is the ratio between the number of expected background counts in the BG ROI to the number in the ES ROI. Note that since these events are multi-detector events, it is possible for multiple hits in the event to fall into one of the ROIs; however, we will choose a single hit to represent the whole event. In this case, any hit that falls into the ES ROI takes precedence over any hit that falls into the BG ROI, and if multiple hits fall into the ES ROI, one is chosen at random. This approach would produce a very small bump in an otherwise flat background at the ES ROI; this is accounted for in the calculation of  $\tau$ .  $\tau$  is usually determined based on the background simulation; however, in cases where the simulation statistics are limited after applying all cuts, a flat background is assumed and the ratio of the ES ROI width to the BG ROI width is used.  $\langle T_k^* \rangle$  represents the expected value of  $T_k^*$  based on previous measurements of exposure and detection efficiency, which is assumed to have Gaussian uncertainty:

$$\sigma_{T_k^*,k} = \langle T_k^* \rangle \sqrt{\left(\frac{\sigma_{\epsilon,k}}{\epsilon_k}\right)^2 + \left(\frac{\sigma_{exposure}}{M_{iso}T_{live}}\right)^2} \quad (23)$$

The implementation of Equation 22 is performed by the `TRolke` class in ROOT [14]. This likelihood function is used to compute a likelihood ratio

$$LR_k(T_{1/2}) = \frac{\sup_{T_k^*, b_k} (\mathcal{L}_k(T_{1/2}, T_k^*, b_k | n_k, m_k, \langle T_k^* \rangle, \sigma_{T_k^*,k}, \tau))}{\sup_{T_{1/2}, T_k^*, b_k} (\mathcal{L}_k(T_{1/2}, T_k^*, b_k | n_k, m_k, \langle T_k^* \rangle, \sigma_{T_k^*,k}, \tau))} \quad (24)$$

The `TRolke` class analytically computes the supremum over  $T_k^*$  and  $b_k$ , returning the log-likelihood difference. The implementation is parameterized in terms of  $\Gamma = \frac{1}{T_{1/2}}$ , which is restricted to positive values; if the supremum of the function has a negative value of  $\Gamma$ , then the value at  $\Gamma = 0$  is used instead. Since the likelihood ratio is expected to

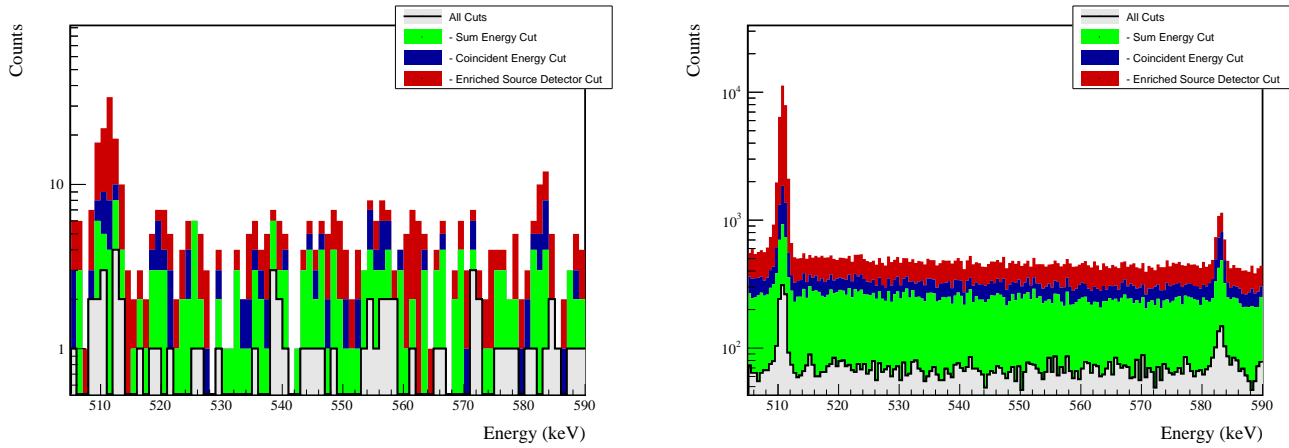


FIG. 27 Effect of cuts on all events in the BG and ES ROIs. Events are applied in sequence from top to bottom, meaning that if an event is cut by multiple cuts, it will be colored based on the first cut that applied. Both the simulated and measured event spectra are shown for comparison.

be  $\chi^2$ -distributed, to construct a 90% confidence interval, we seek the values of  $T_{1/2}$  corresponding to a log-likelihood ratio value of 2.7. In cases where the lower limit on  $\gamma$  is found to be  $< 0$ , a lower limit on  $T_{1/2}$  is reported.

After constructing confidence intervals for each peak and module individually, a combined confidence interval is constructed for each  $\beta\beta$  E.S. decay mode. A combined log-likelihood over all peak/module combinations  $k$  is defined by

$$\log(\mathcal{L}(T_{1/2})) = \sum_{k=0}^N \sup_{T_k^*, b_k} (\log(\mathcal{L}_k(T_{1/2}, T_k^*, b_k | n_k, m_k, \langle T_k^* \rangle, \sigma_{T^*, k}, \tau))) \quad (25)$$

This construction relies on the fact that the  $T_k^*$  and  $b_k$  values across each peak can be independently maximized, enabling the continued use of the TRolke implementation. A combined likelihood ratio is constructed:

$$\log(\text{LR}(T_{1/2})) = \log(\mathcal{L}(T_{1/2})) - \sup_{T_{1/2}} (\log(\mathcal{L}(T_{1/2}))) \quad (26)$$

and used to compute a confidence interval as above. Table VII contains the limits constructed for each decay mode, peak and module. For all modes, a lower half-life limit is set.

Note that each decay mode is analyzed independently. The problem with this approach is that all decay modes have the 559 keV peak in common, meaning that the results will be correlated. For this result, since all modes only have a lower limit on half-life set, this approach is not problematic since for any individual mode, we would take the supremum over all other half-lives, which would be at or near infinity, resulting in the same sets of equations used here. However, if the  $\beta\beta$  E.S. to the  $0_1^+$  mode is discovered, it will become necessary to perform a full combined analysis.

The detection sensitivity is computed by constructing a toy Monte Carlo for each decay mode, assuming that each  $T_{1/2}$  is infinite. For each sample  $i$ , a random  $n_i$  and  $m_i$  is drawn from a Poisson distribution with mean  $b_k$  and  $m_k$ . The confidence interval for a measurement with these values is computed. The median sensitivity is extracted by taking the median lower half-life limit over all samples. For the results in Table VII, 100001 samples were used.

## 583 B. Limits and Sensitivities

584 The limits and sensitivities for each peak and module individually, and the combination for each mode, are shown  
585 in Table VII. Figure 28 shows the event spectrum after all cuts have been applied with both ROIs highlighted.

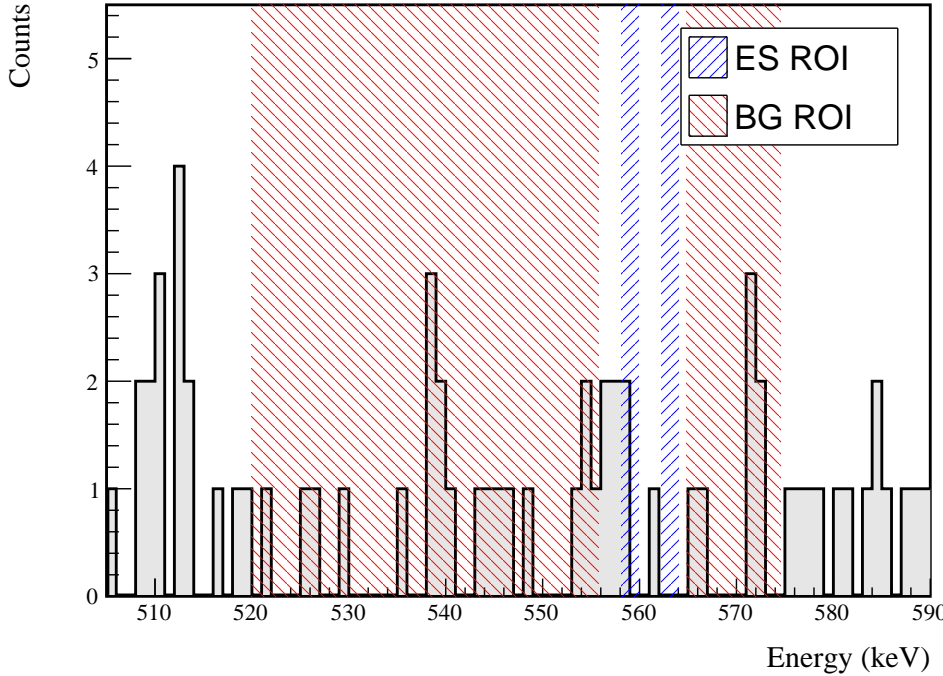
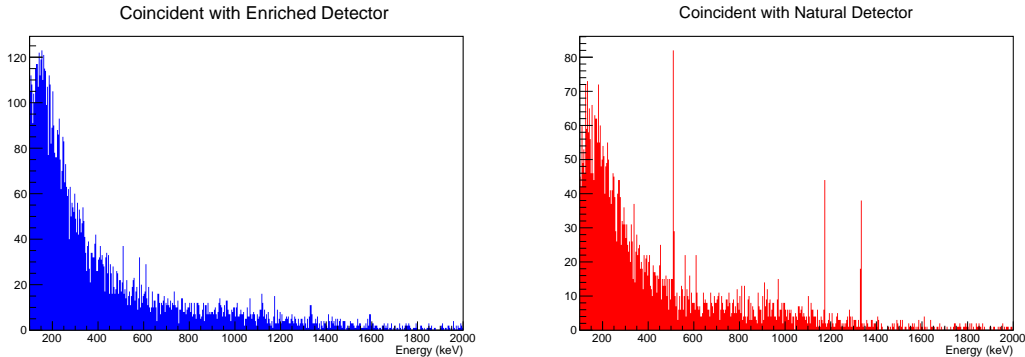


FIG. 28 Events that pass all cuts for the  $2\nu\beta\beta$  to  $0^+$  decay mode. The ES and BG ROIs are highlighted. Note that these ROIs undergo small variations from dataset to dataset, and the ROIs drawn here are averaged over all datasets. The energies shown in this spectrum are the energies of the hit that places the event in the ROI. A single event will only be placed once into an ROI; however, as drawn here, if multiple hits in a single event fall into an ROI, they will all be drawn.

### 586 C. Background Model Discussion

587 Several interesting discrepancies exist between the data used for this result and the background model. It is important  
 588 to keep in mind that the result only depends on the model for optimization; this means that these discrepancies  
 589 make this result not-quite-optimal, but not incorrect.

590 One discrepancy is can be seen in table VI, where the cut efficiency of the enriched coincident detector cut is  
 591 much higher than expected. This suggests an excess of backgrounds from decays of cosmogenics in natural isotopic  
 592 abundance detectors. Figure 29 shows a comparison of the multiplicity 2 event hit spectrum for hits in coincidence  
 593 with natural and enriched detectors. There is a clear excess of 511 keV hits for events in coincidence with natural



594 FIG. 29 Energy spectrum of hits in coincidence with enriched (left, blue) and natural (right, red) detector hits. Note the  
 595 excesses of 511, 1173 and 1333 keV events in coincidence with natural hits.



Decay Mode	Peak	Module	$n_{ROI}$	$m_{BG}$	Expected ROI BGs	$T^* (\times 10^{23} \text{y})$	$T_{1/2} (\times 10^{23} \text{y})$ 90% Limit	$T_{1/2} (\times 10^{23} \text{y})$ 90% Sensitivity
$0^+_{g.s.} \xrightarrow{2\nu\beta\beta} 0^+_1$	559 keV	M1	2	51	$1.77 \pm 1.18$	$16.63 \pm 1.18$	> 4.7	> 5.1
		M2	1	6	0.25	$4.46 \pm 0.82$	> 1.3	> 3.2
	563 keV	M1	2	51	$1.95 \pm 1.19$	$16.72 \pm 1.19$	> 4.9	> 5.2
	Combined	M2	0	6	0.22	$4.41 \pm 0.81$	> 3.2	> 3.2
$0^+_{g.s.} \xrightarrow{2\nu\beta\beta} 2^+_1$	559 keV	M1	0	35	1.43	$19.23 \pm 1.96$	> 14.1	> 7.8
	Combined	M2	1	2	0.10	$5.16 \pm 1.73$	> 1.2	> 3.3
							> 7.7	> 10.2
$0^+_{g.s.} \xrightarrow{2\nu\beta\beta} 2^+_2$	559 keV	M1	3	76	2.64	$13.89 \pm 1.72$	> 3.2	> 4.3
		M2	1	8	0.32	$3.86 \pm 1.78$	> 0.8	> 2.4
	657 keV	M1	0	30	0.98	$10.66 \pm 1.39$	> 7.8	> 4.0
		M2	0	3	0.10	$3.05 \pm 1.53$	> 1.8	> 1.8
	1216 keV	M1	0	41	1.07	$5.79 \pm 1.60$	> 4.0	> 2.1
	Combined	M2	0	7	0.24	$1.52 \pm 1.84$	> 2.2	> 2.2
							> 12.6	> 8.8
$0^+_{g.s.} \xrightarrow{0\nu\beta\beta} 0^+_1$	559 keV	M1	0	6	0.24	$21.45 \pm 1.81$	> 15.8	> 15.8
		M2	0	1	0.06	$5.69 \pm 1.14$	> 4.1	> 4.1
	563 keV	M1	0	6	0.25	$21.19 \pm 1.79$	> 15.6	> 15.6
	Combined	M2	0	1	0.06	$5.58 \pm 1.12$	> 4.0	> 4.0
$0^+_{g.s.} \xrightarrow{0\nu\beta\beta} 2^+_1$	559 keV	M1	0	0	0.00	$22.89 \pm 2.48$	> 16.8	> 16.8
	Combined	M2	0	0	0.00	$5.98 \pm 2.06$	> 4.0	> 4.0
							> 21.2	> 21.2
$0^+_{g.s.} \xrightarrow{0\nu\beta\beta} 2^+_2$	559 keV	M1	0	8	0.29	$13.38 \pm 1.81$	> 9.8	> 9.8
		M2	0	1	0.07	$3.54 \pm 1.70$	> 2.1	> 2.1
	657 keV	M1	0	10	0.41	$13.27 \pm 1.86$	> 9.7	> 9.7
		M2	0	1	0.01	$3.48 \pm 1.82$	> 1.9	> 1.9
	1216 keV	M1	0	0	0.00	$6.16 \pm 1.67$	> 4.3	> 4.3
	Combined	M2	0	0	0.00	$1.62 \pm 1.90$	> 0.4	> 0.4
							> 30.4	> 18.7

TABLE VII Results for all decay modes.

detectors, caused by cosmogenic  $^{68}\text{Ge}$ ; this is accounted for in the background model. There is also a clear excess of 1173 and 1333 keV hits in coincidence with natural detectors, originating from cosmogenic  $^{60}\text{Co}$ , which is NOT included in the background model used. Figure ?? shows the hit spectrum for natural germanium events in coincidence with 1173 and 1333 keV hits. The  $^{60}\text{Co}$   $\beta$  spectrum, with a Q-value of 318 keV, is visible, along with pileup of  $\beta$ s and  $\gamma$ s at energies up to 1651 keV. Cosmogenic  $^{60}\text{Co}$  will be included in future versions of the background model. Fortunately, these events are cut with very high efficiency by the coincident enriched detector cut, both explaining the discrepancy in table VI and preventing a large contribution of these events towards backgrounds for this result.

Another discrepancy can be seen in figure 27, where the 511 keV peak is significantly wider than expected. This peak is also significantly wider than the 511 keV peak found in calibration data. Note that all other peaks visible in data have FWHMs consistent with expectations based on table XXVI. The width of the 511 keV peak can be explained by doppler broadening of annihilation electrons. Doppler broadening increases as the velocity of either the electron or positron involved in annihilation increases; as a result, annihilation with valence electrons results in a wider peak than annihilation with conduction band electrons. Most 511 keV  $\gamma$ s in high multiplicity MJD data are expected to originate from positron decay of  $^{68}\text{Ge}$  that is cosmogenically activated in natural isotopic abundance detectors. Because these detectors are depleted, these annihilations will involve valence band electrons instead of conduction band electrons resulting in a wider peak. A similar effect can be observed in calibration data by comparing the width of 511 keV  $\gamma$ s that occur as multiplicity 1 events, which likely originate from pair productions in surrounding copper, with an abundance of conduction band electrons, to those that occur in coincidence with DEP or SEP detector hits, which occur in the depleted regions of detectors. Figure 31 shows this comparison; the multiplicity 1 peak has a FWHM of 1.3 keV, while the SEP/DEP coincident peak has a FWHM of 2.4 keV.

### XIII. UNBLINDING PLAN

Previous results presented used only open data from DS1-6a; this document also includes blind data in these datasets. The plan that follows was written prior to unblinding and was followed. A bug that was quickly fixed resulted in incorrect detector selection for DS6a blind runs; this was discovered due to large spikes in the data rates from figure 25. For the sake of posterity, the plan has been left in this document.

Data is blinded by administratively by forbidding access to built and gatified files to users; access to blinded data is provided through skim files. Unblinding proceeds in multiple stages; skim files produced in the first stage exclude high multiplicity events, events in the 400 keV ROI around  $Q_{\beta\beta}$ , and low energy events. Access to these events is

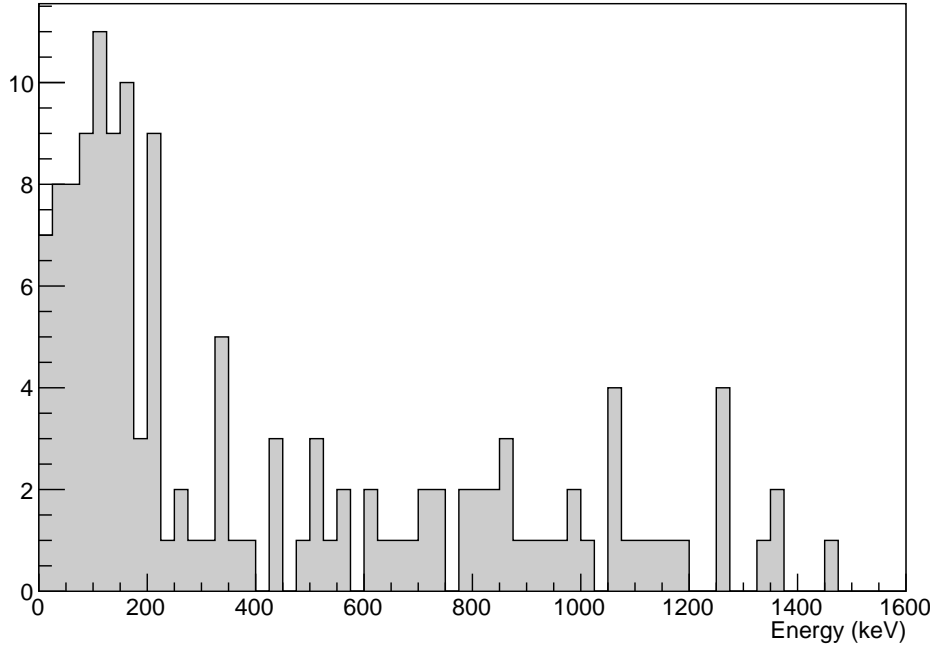


FIG. 30 Energy spectrum for natural detector hits in coincidence with 1173 and 1333 keV  $\gamma$ s.

626 provided individually to analyzers through inclusion in skim files accessible only by that individual. For this analysis,  
627 high multiplicity events will be needed.

628 Prior to unblinding, several steps will be completed. First, subdatasets must be identified using `es_get_datasets`,  
629 requiring access to channel selection files that are produced during the first stage of unblinding. Next, the live time  
630 must be measured. Unfortunately, this requires access to detailed run information from built files, which are left  
631 blinded; as a result, `es_livetime` must be run by someone with access to the mjd account. Next, background model  
632 and excited state simulations for each subdataset will be produced using `es_skimsim`. Next, cut optimization must be  
633 performed using `es_optimize_cuts`. Because an estimate of a scaling required to get the actual background level from  
634 the simulations is required for this step, an estimate should be made using the already unblinded single-site events.  
635 Finally, cuts should be applied with `es_apply_cuts`, and the efficiencies and exposures estimated using `es_get_result`  
636 with the `--nodata` option. In addition to running this code, plots of the simulated data should be made, similar to  
637 those displayed in Appendix A. Once this is completed, the plots and efficiencies should be inspected; any discrepancies  
638 between the unblinded result and these blinded numbers should be understood prior to unblinding.

639 Once the analysis is approved for unblinding and skim files with high multiplicity data have been produced,  
640 `es_skim_data` will be used to collect the high multiplicity events therein. `es_get_result` should be run using this  
641 data. The sanity checks discussed in Sections XI.A and XI.B should be performed, and any discrepancies in the  
642 data rate or cut efficiencies should be explained, and any changes to the analysis resulting from these checks must be  
643 carefully documented. Finally, `es_get_limits` can be run to get the final limits.

644 Unblinding will approximately double the exposure to  $\sim 40$  kg-y of isotopic exposure. Assuming identical back-  
645 grounds and efficiencies, the projected half-life sensitivity for the search to the first  $0^+$  decay is  $\sim 1 \cdot 10^{24}$  yr. It  
646 should be noted that rerunning the cut optimization with a more exposure will result in a slightly more stringent set  
647 of cuts; as a result, the background rate and detection efficiency will both be lower. The cutoff at the end of DS6a  
648 is motivated by the fact that this encompasses all data in the MAJORANA DEMONSTRATOR 2018  $0\nu\beta\beta$  release, and  
649 has been extensively vetted. In concert with the next major  $0\nu\beta\beta$  release, containing DS6b and 6c data, this analysis  
650 will add the additional exposure as well.

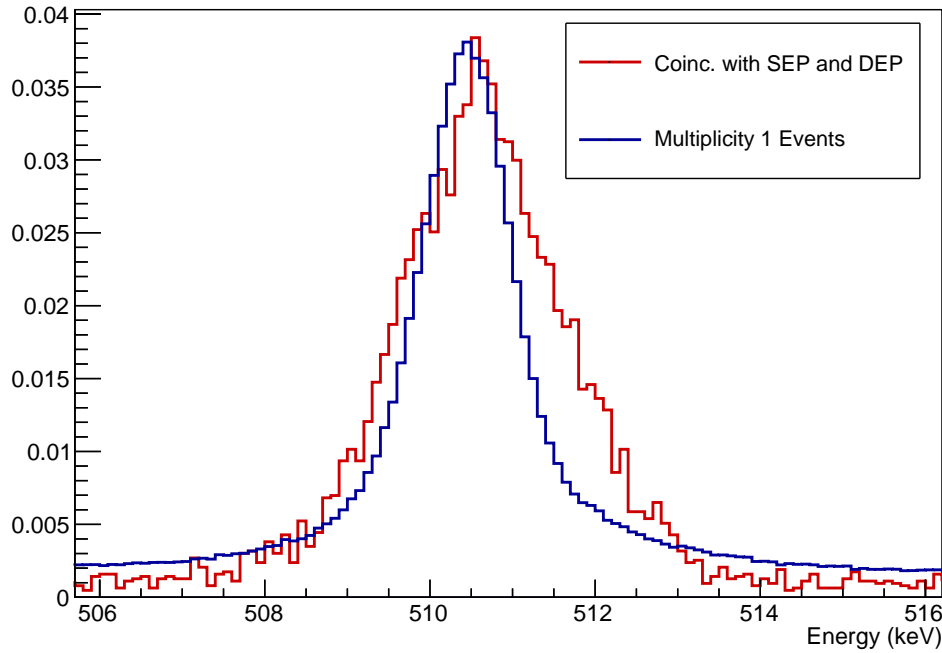


FIG. 31 The 511 keV peak from single-detector events (blue) have a FWHM of 1.3 keV. The 511 keV peak in coincidence with SEP and DEP events has a FWHM of 2.4 keV.

## 651 REFERENCES

- [1] J. Kotila and F. Iachello. Phase-space factors for double- $\beta$  decay. *Phys. Rev. C*, 85:034316, Mar 2012.  
[2] O. A. Ponkratenko, V. I. Tretyak, and Yu. G. Zdesenko. Event generator decay4 for simulating double-beta processes and decays of radioactive nuclei. *Physics of Atomic Nuclei*, 63(7):1282–1287, Jul 2000.  
[3] Balraj Singh. Nuclear data sheets update for A = 76. *Nuclear Data Sheets*, 74(1):63 – 164, 1995.  
[4] Robley D. Evans. *The Atomic Nucleus*, chapter 6, page 240. International series in pure and applied physics. McGraw-Hill, New York, 1955.  
[5] Micah Buuck. *A Comprehensive Radiogenic Background Model for the MAJORANA DEMONSTRATOR*. PhD thesis, University of Washington, 2019.  
[6] Pavol Vojtyla. Fast computer simulations of background of low-level Ge  $\gamma$ -spectrometers induced by  $^{210}\text{Pb}$   $^{210}\text{Bi}$  in shielding lead. *Nuclear Instruments and Methods in Physics Research Section B: Beam Interactions with Materials and Atoms*, 117(1):189 – 198, 1996.  
[7] I. Antcheva, M. Ballintijn, B. Bellenot, M. Biskup, R. Brun, N. Buncic, Ph. Canal, D. Casadei, O. Couet, V. Fine, L. Franco, G. Ganis, A. Gheata, D. Gonzalez Maline, M. Goto, J. Iwaszkiewicz, A. Kreshuk, D. Marcos Segura, R. Maunder, L. Moneta, A. Naumann, E. Offermann, V. Onuchin, S. Panacek, F. Rademakers, P. Russo, and M. Tadel. Root — a c++ framework for petabyte data storage, statistical analysis and visualization. *Computer Physics Communications*, 180(12):2499 – 2512, 2009. 40 YEARS OF CPC: A celebratory issue focused on quality software for high performance, grid and novel computing architectures.  
[8] A Reine, T Caldwell, C Cuesta, I Guinn, and J Myslik. Run selection and data cleaning of ds5 (m1 and m2) (internal). Technical Report 2017-020, University of North Carolina at Chapel Hill, May 2018.  
[9] F. James. MINUIT Function Minimization and Error Analysis: Reference Manual Version 94.1. Technical Report CERN-D506, CERN CN Division, Geneva, 1994.  
[10] P. Chu, J. Detwiler, and I. Guinn. Energy systematic of MAJORANA DEMONSTRATOR. Technical Report 2017-021, Los Alamos National Laboratory, Oct 2017.  
[11] R.P. Brent. *Algorithms for Minimization without Derivatives*. Prentice-Hall, Englewood Cliffs, NJ, 1973.  
[12] H. Akaike. A new look at the statistical model identification. *IEEE Transactions on Automatic Control*, 19(6):716–723, December 1974.  
[13] C Wiseman. Muon veto analysis for the MAJORANA DEMONSTRATOR (internal). Technical report, University of South Carolina, 2016.  
[14] Wolfgang A. Rolke, Angel M. López, and Jan Conrad. Limits and confidence intervals in the presence of nuisance parameters. *Nuclear Instruments and Methods in Physics Research Section A: Accelerators, Spectrometers, Detectors*



and Associated Equipment, 551(2):493 – 503, 2005.

- [15] F. Alessandria, R. Ardito, D. R. Artusa, III Avignone, F. T., O. Azzolini, M. Balata, T. I. Banks, G. Bari, J. Beeman, F. Bellini, A. Bersani, M. Biassoni, T. Bloxham, C. Brofferio, C. Bucci, X. Z. Cai, L. Canonica, X. Cao, S. Capelli, L. Carbone, L. Cardani, M. Carrettoni, N. Casali, D. Chiesa, N. Chott, M. Clemenza, C. Cosmelli, O. Cremonesi, R. J. Creswick, I. Dafinei, A. Dally, V. Datskov, A. De Biasi, M. M. Deninno, S. Di Domizio, M. L. di Vacri, L. Ejzak, R. Faccini, D. Q. Fang, H. A. Farach, M. Faverzani, G. Fernandes, E. Ferri, F. Ferroni, E. Fiorini, M. A. Franceschi, S. J. Freedman, B. K. Fujikawa, A. Giachero, L. Gironi, A. Giuliani, J. Goett, P. Gorla, C. Gotti, E. Guardincerri, T. D. Gutierrez, E. E. Haller, K. Han, K. M. Heeger, H. Z. Huang, R. Kadel, K. Kazkaz, G. Keppel, L. Kogler, Yu. G. Kolomensky, D. Lenz, Y. L. Li, C. Ligi, X. Liu, Y. G. Ma, C. Maiano, M. Maino, M. Martinez, R. H. Maruyama, Y. Mei, N. Moggi, S. Morganti, T. Napolitano, S. Newman, S. Nisi, C. Nones, E. B. Norman, A. Nucciotti, T. O'Donnell, F. Orio, D. Orlandi, J. L. Ouellet, M. Pallavicini, V. Palmieri, L. Pattavina, M. Pavan, M. Pedretti, G. Pessina, G. Piperno, S. Pirro, E. Previtali, V. Rampazzo, F. Rimondi, C. Rosenfeld, C. Rusconi, E. Sala, S. Sangiorgio, N. D. Scielzo, M. Sisti, A. R. Smith, F. Stivanello, L. Taffarello, M. Tenconi, W. D. Tian, C. Tomei, S. Trentalange, G. Ventura, M. Vignati, B. S. Wang, H. W. Wang, T. Wise, A. Woodcraft, L. Zanotti, C. Zarra, B. X. Zhu, and S. Zucchelli. Sensitivity and Discovery Potential of CUORE to Neutrinoless Double-Beta Decay. *arXiv e-prints*, page arXiv:1109.0494, Sep 2011.

## Appendix A: Detailed Results for All Decay Modes

The main document concerned itself primarily with the  $2\nu\beta\beta$  of  $^{76}\text{Ge}$  to the  $0_1^+$  excited state. However, results are presented for all decay modes and energy peaks. This appendix will present figures and tables detailing the simulations, cuts, efficiencies and results for each decay mode and peak.

## Appendix B: $2\nu\beta\beta$ to $0_1^+$

Note that both the 559 and 563 keV peaks will be shown together since they use the same sets of cuts.

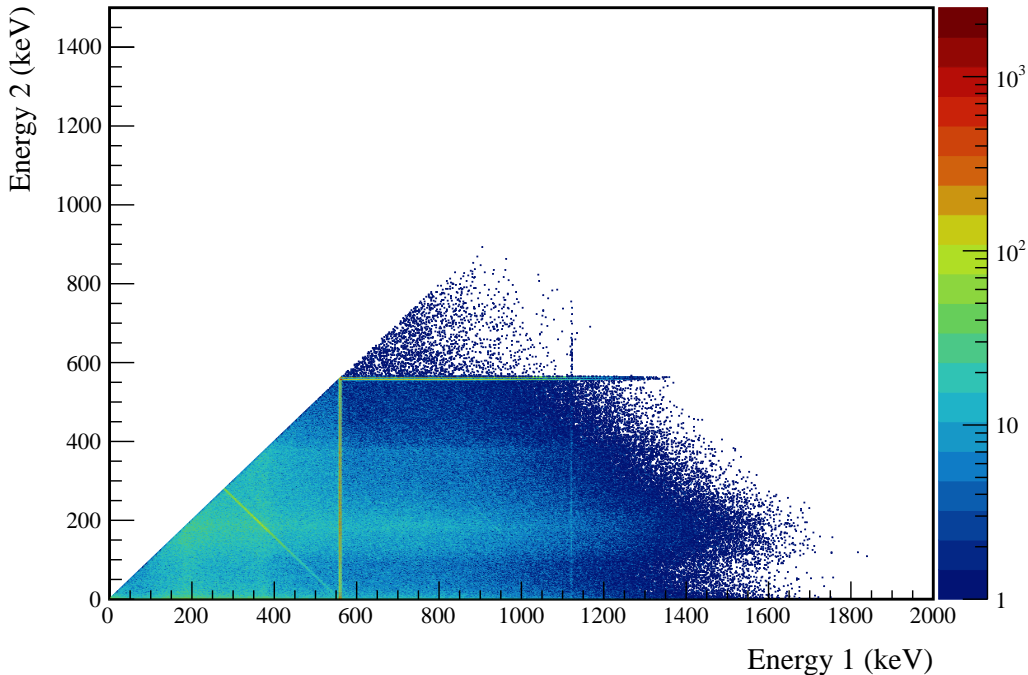


FIG. 32 Simulated multiplicity 2 energy spectrum of the  $2\nu\beta\beta$  to  $0_1^+$  decay mode



TABLE VIII Table of energy estimation uncertainties for the 559 and 563 keV peaks.

DS	$E_{peak}$ (keV)	$\sigma_{fit}$ (keV)	$\sigma_{drift}$ (keV)	$\sigma$ (keV)	$f_{t,fit}$ (keV)	$f_{t,fit}$ (keV)	$\tau_{fit}$ (keV)	$\delta_{\mu,fit}$ (keV)	$\delta_{\mu,NL}$ (keV)	$\delta_{\mu,drift}$ (keV)	$\delta_{\mu,peak}$ (keV)	$\delta_u$ (keV)	FWHM (keV)	$\delta_{fwhm,drift}$ (keV)	$\delta_{fwhm,fit}$ (keV)	$\delta_{fwhm,xtalk}$ (keV)	$\delta_{FWHM}$ (keV)	$\delta_\alpha$	$E_{ROI,1}$ (keV)	$E_{ROI,2}$ (keV)	$\epsilon_{ROI}$	$\sigma_{\epsilon_{ROI}}$
DS1	559.101	0.460	0.063	0.464	0.230	0.515	0.001	0.104	0.002	0.012	0.005	0.105	1.152	0.001	0.039	0.001	0.040	0.035	558.230	559.823	0.859	0.016
DS2	559.101	0.461	0.055	0.464	0.249	0.515	0.002	0.067	0.004	0.012	0.005	0.068	1.158	0.001	0.107	0.011	0.108	0.093	558.217	559.820	0.862	0.032
DS3	559.101	0.470	0.066	0.474	0.224	0.505	0.001	0.026	0.024	0.012	0.005	0.038	1.174	0.001	0.073	0.011	0.074	0.063	558.218	559.838	0.868	0.022
DS4	559.101	0.455	0.077	0.461	0.108	0.445	0.002	0.076	0.010	0.012	0.005	0.078	1.111	0.001	0.106	0.011	0.107	0.096	558.309	559.832	0.876	0.034
DS5a	559.101	0.560	0.085	0.567	0.106	0.855	0.002	0.079	0.005	0.012	0.005	0.080	1.367	0.002	0.055	0.011	0.056	0.041	558.131	559.994	0.864	0.015
DS5b	559.101	0.469	0.074	0.475	0.158	0.491	0.001	0.020	0.011	0.012	0.005	0.026	1.157	0.001	0.125	0.011	0.125	0.108	558.258	559.847	0.874	0.037
DS5c	559.101	0.460	0.085	0.468	0.174	0.489	0.001	0.037	0.030	0.012	0.005	0.050	1.145	0.001	0.162	0.011	0.162	0.142	558.260	559.835	0.871	0.049
DS6a	559.101	0.456	0.044	0.458	0.191	0.463	0.001	0.069	0.025	0.012	0.005	0.075	1.123	0.000	0.041	0.011	0.042	0.038	558.270	559.817	0.869	0.014
DS1	563.178	0.461	0.064	0.466	0.230	0.518	0.001	0.104	0.002	0.012	0.005	0.105	1.156	0.001	0.039	0.011	0.040	0.035	562.303	563.902	0.859	0.016
DS2	563.178	0.463	0.055	0.466	0.249	0.517	0.002	0.067	0.004	0.012	0.005	0.068	1.162	0.001	0.107	0.011	0.108	0.093	562.291	563.900	0.862	0.032
DS3	563.178	0.471	0.066	0.476	0.224	0.508	0.001	0.026	0.024	0.012	0.005	0.038	1.179	0.001	0.073	0.011	0.074	0.063	562.291	563.918	0.867	0.022
DS4	563.178	0.457	0.077	0.463	0.108	0.447	0.002	0.076	0.010	0.012	0.005	0.078	1.115	0.001	0.106	0.011	0.107	0.096	562.383	563.911	0.876	0.034
DS5a	563.178	0.562	0.086	0.569	0.106	0.858	0.002	0.079	0.006	0.012	0.005	0.080	1.372	0.002	0.055	0.011	0.056	0.041	562.204	564.074	0.864	0.015
DS5b	563.178	0.471	0.074	0.477	0.158	0.494	0.001	0.020	0.011	0.012	0.005	0.026	1.162	0.001	0.125	0.011	0.125	0.108	562.332	563.927	0.874	0.037
DS5c	563.178	0.462	0.086	0.470	0.174	0.492	0.001	0.037	0.030	0.012	0.005	0.050	1.449	0.001	0.162	0.011	0.162	0.141	562.334	563.915	0.871	0.048
DS6a	563.178	0.457	0.044	0.459	0.191	0.465	0.001	0.069	0.026	0.012	0.005	0.075	1.127	0.000	0.041	0.011	0.042	0.038	562.344	563.897	0.869	0.014



Cut Name	Cut Description	$\langle \epsilon_{total} \rangle$	$\hat{\epsilon}_{total}$	$\langle \epsilon_{unique} \rangle$	$\hat{\epsilon}_{unique}$	Sacrifice	$\Delta IDP$
Enriched Source Detector Cut	Any other detector: <code>isBar</code>	M1: 21.5 % M2: 40.5 %	$23.3^{+2.7}_{-2.5}$ % $63.8^{+6.0}_{-6.5}$ %	3.2 % 6.7 %	$2.3^{+1.1}_{-0.7}$ % $12.1^{+4.9}_{-3.6}$ %	1.0 % 2.9 %	9%
Coincident Energy Cut	No other detector: <code>((energy&lt;40.8)    (energy&gt;403.4 &amp;&amp; energy&lt;509.2)    (energy&gt;512.2)    (energy&gt;403.4 &amp;&amp; energy&lt;11.4)    (energy&gt;170.6 &amp;&amp; energy&gt;1176.6)    (energy&gt;1204.2 &amp;&amp; energy&gt;1208.2)    (energy&gt;1259.2)    (energy&gt;1208.2 &amp;&amp; energy&gt;1259.2)    (energy&gt;497.6 &amp;&amp; energy&gt;522.)    (energy&gt;568.6 &amp;&amp; energy&gt;591.6)    (energy&gt;903.2 &amp;&amp; energy&gt;931.2)    (energy&gt;1169.6 &amp;&amp; energy&gt;1174.6)    (energy&gt;1330.6 &amp;&amp; energy&gt;1333.6)    (energy&gt;1462.2 &amp;&amp; energy&gt;1761.8)    (energy&gt;1824.6 &amp;&amp; energy&gt;1871.6))</code>	M1: 20.6 % M2: 22.9 %	$21.8^{+2.6}_{-2.4}$ % $31.0^{+6.4}_{-5.7}$ %	3.5 % 3.2 %	$1.9^{+1.0}_{-0.7}$ % $1.7^{+2.7}_{-1.1}$ %	2.8 % 2.1 %	5%
Sum Energy Cut	Note: <code>(sumE&gt;852.2)    (sumE&gt;853.2) &amp;&amp; sumE&gt;855.4)    (sumE&gt;855.6 &amp;&amp; sumE&gt;877.8)    (sumE&gt;961.8 &amp;&amp; sumE&gt;971.8)    (sumE&gt;1169.6 &amp;&amp; sumE&gt;1174.6)    (sumE&gt;1330.6 &amp;&amp; sumE&gt;1333.6)    (sumE&gt;1468.6 &amp;&amp; sumE&gt;1462.2)    (sumE&gt;1761.8 &amp;&amp; sumE&gt;1771.6)</code>	M1: 73.1 % M2: 73.8 %	$74.4^{+2.6}_{-2.8}$ % $72.4^{+5.5}_{-6.2}$ %	44.8 % 33.5 %	$44.4 \pm 3.0$ % $20.7^{+5.8}_{-4.8}$ %	29.8 % 30.7 %	19%
Combined Cuts		M1: 81.6 % M2: 86.9 %	$80.8^{+2.3}_{-2.5}$ % $89.7^{+3.3}_{-4.7}$ %	—	—	41.0 % 49.0 %	29%

TABLE IX Table of cut descriptions and efficiencies for simulated backgrounds and measured data for the 559 and 563 keV peaks.

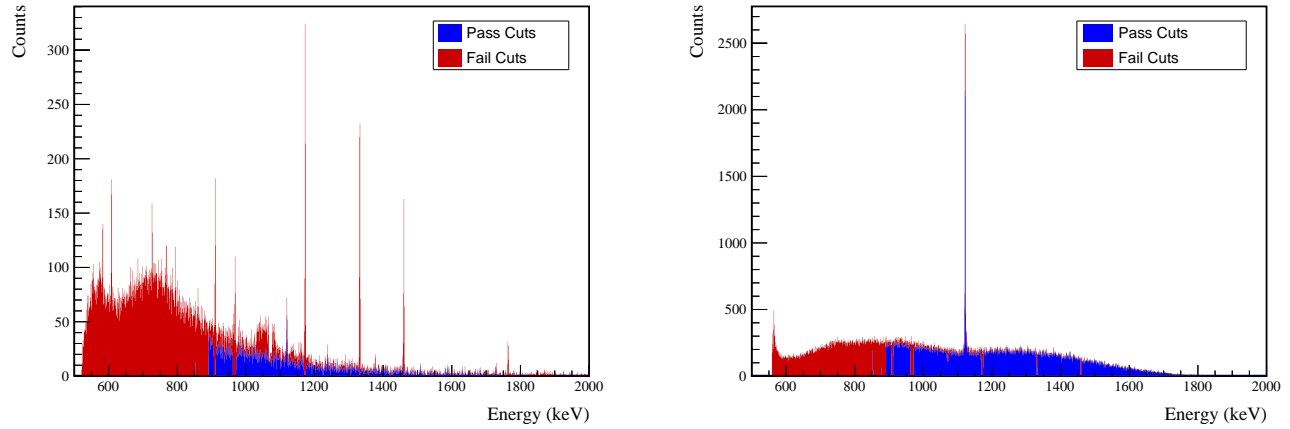


FIG. 33 Effect of 559 and 563 keV peaks cuts on sum energy spectra in BG (left) and ES (right) simulations.

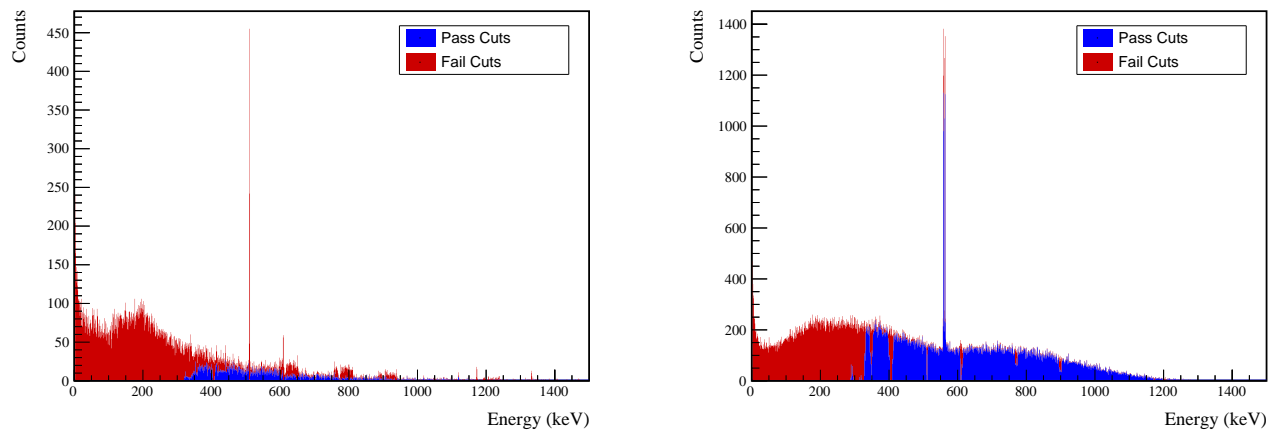


FIG. 34 Effect of 559 and 563 keV peaks cuts on coincident energy spectra in BG (left) and ES (right) simulations.

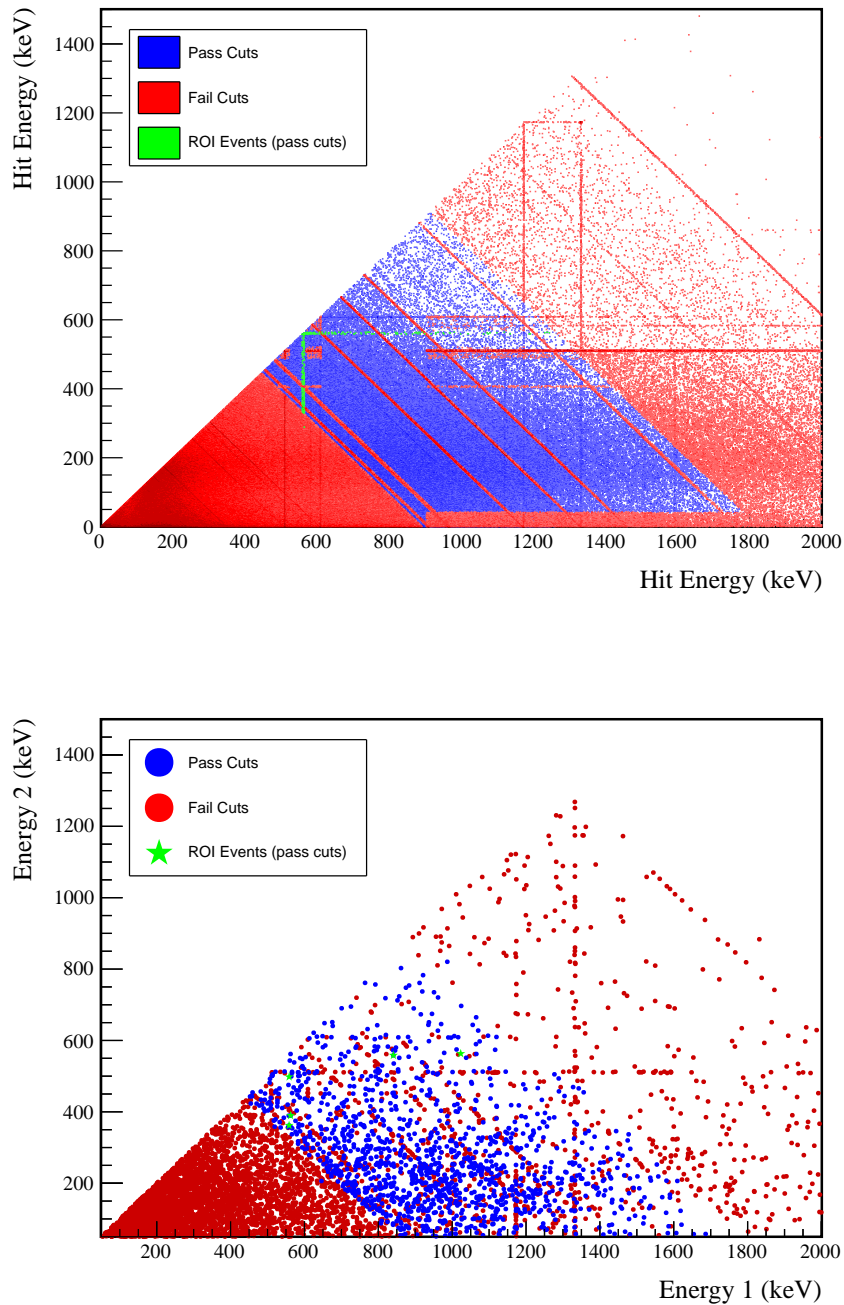
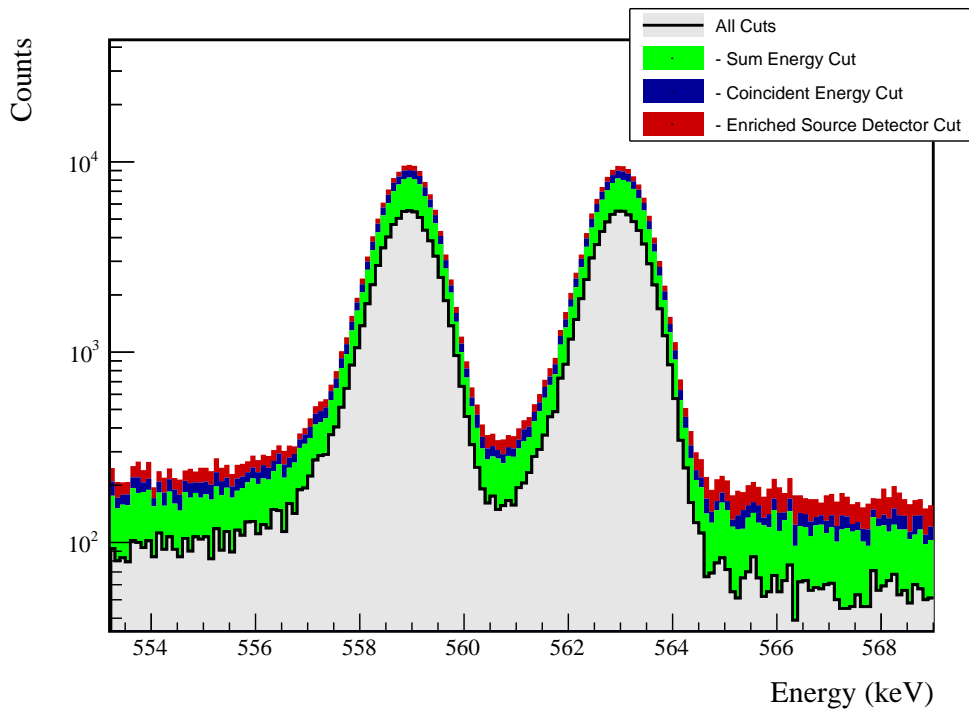


FIG. 35 Simulated (left) and measured (right) multiplicity 2 energy spectrum with sum and coincident energy cuts included for the 559 and 563 keV peaks.

FIG. 36 Effect of all cuts applied sequentially on ROI for 559 and 563 keV peaks of  $2\nu\beta\beta$  to  $0_1^+$ 

Source	Module 1 efficiency	Module 2 efficiency
Multi-Detector with Full Energy $\gamma$	$5.7 \pm 0.2\%$	$3.1 \pm 0.5\%$
Region of Interest Dead Layer	$86.8 \pm 1.5\%$	$86.8 \pm 1.5\%$
Detector Dead Times	$74.8 \pm 4.3\%$	$63.5 \pm 6.4\%$
Enriched Source Detector Cut	$98.3 \pm 0.8\%$	$98.5 \pm 0.7\%$
Coincident Energy Cut	$96.9 \pm <0.1\%$	$90.5 \pm <0.1\%$
Sum Energy Cut	$91.3 \pm 0.5\%$	$89.6 \pm 0.5\%$
Final Efficiency	$63.0 \pm 0.5\%$	$56.7 \pm 0.5\%$
	$2.35 \pm 0.17\%$	$1.00 \pm 0.18\%$

FIG. 37 Table of detection efficiencies for the 559 and 563 keV peaks.

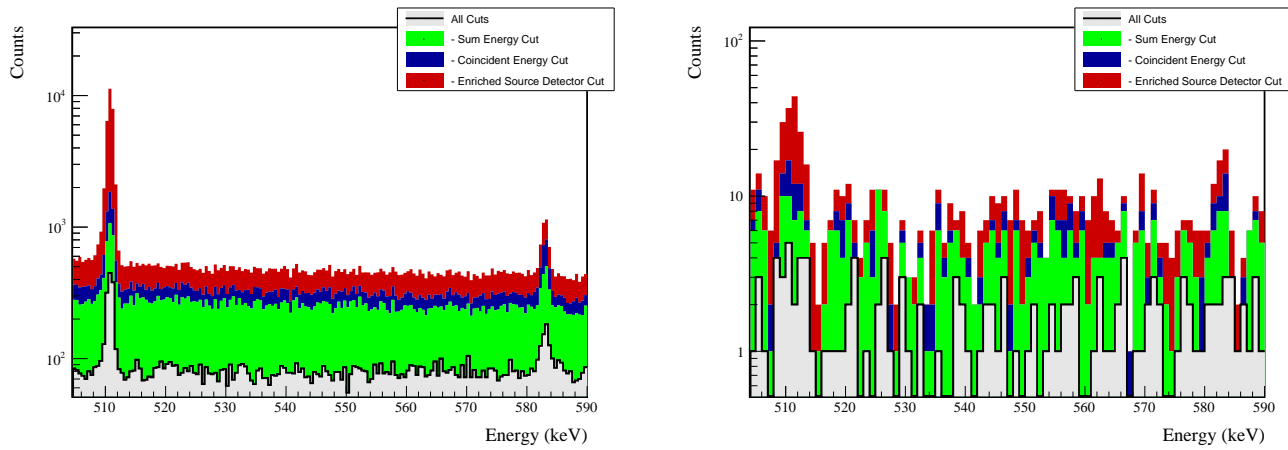


FIG. 38 Effect of all cuts applied to sequentially simulated (left) and measured (right) background data.

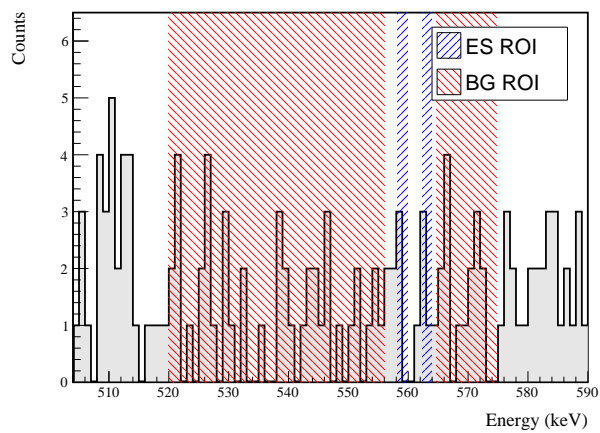


FIG. 39 All events after cuts in background (red) and signal (blue) ROIs for 559 and 563 keV peaks of  $2\nu\beta\beta$  to  $0_1^+$

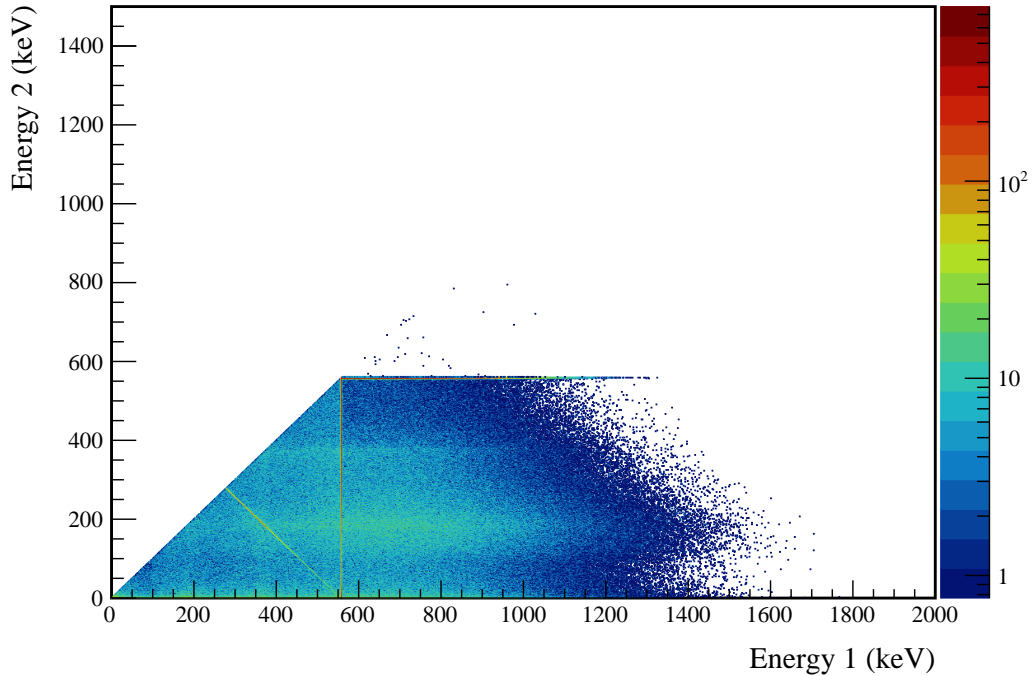
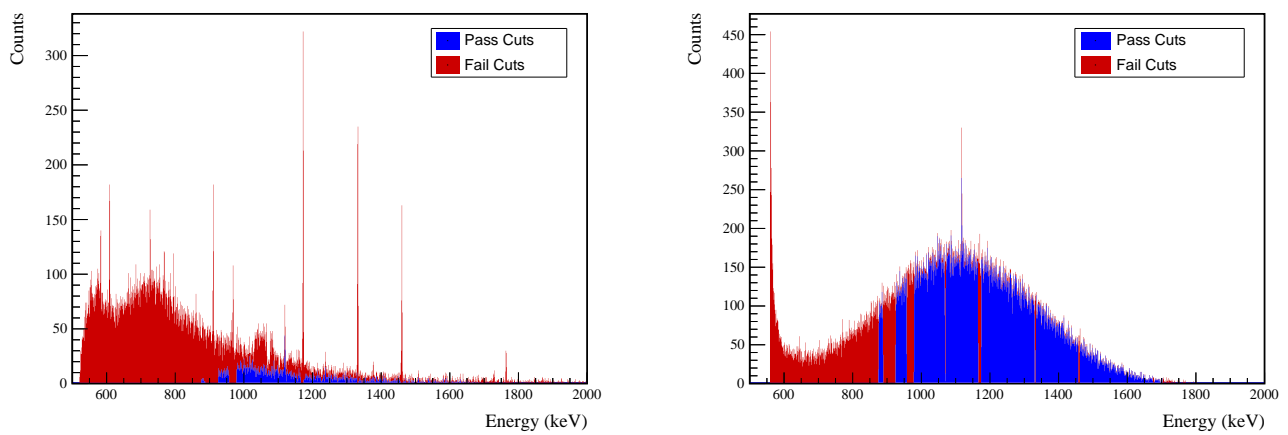
705 **Appendix C:  $2\nu\beta\beta$  to  $2_1^+$** FIG. 40 Simulated multiplicity 2 energy spectrum of the  $2\nu\beta\beta$  to  $2_1^+$  decay mode

FIG. 41 Effect of 559 keV peak cuts on sum energy spectra in BG (left) and ES (right) simulations.



TABLE X Table of energy estimation uncertainties for the 559 keV peak.

DS	$E_{peak}$ (keV)	$\sigma_{drift}$ (keV)	$\sigma_{fit}$ (keV)	$f_{t,fit}$ (keV)	$\sigma$ (keV)	$\tau_{f,fit}$ (keV)	$\delta_{\mu,fit}$ (keV)	$\delta_{\mu,NL}$ (keV)	$\delta_{\mu,drift}$ (keV)	$\delta_{\mu,atalk}$ (keV)	$\delta_{\mu,peak}$ (keV)	$\delta_u$ (keV)	FWHM	$\delta_{fwhm,fit}$ (keV)	$\delta_{fwhm,drift}$ (keV)	$\delta_{fwhm,atalk}$ (keV)	$\delta_{fwhm,peak}$ (keV)	$E_{ROI,1}$ (keV)	$E_{ROI,2}$ (keV)	$\delta_\alpha$		
DS1	559.101	0.460	0.063	0.464	0.230	0.515	0.001	0.104	0.002	0.012	0.005	0.105	1.152	0.001	0.039	0.011	0.040	0.035	558.214	559.835	0.866	0.015
DS2	559.101	0.461	0.055	0.464	0.249	0.515	0.002	0.067	0.004	0.012	0.005	0.068	1.158	0.001	0.107	0.011	0.108	0.093	558.201	559.833	0.868	0.031
DS3	559.101	0.470	0.066	0.474	0.224	0.505	0.001	0.026	0.024	0.012	0.005	0.038	1.174	0.001	0.073	0.011	0.074	0.063	558.201	559.851	0.874	0.021
DS4	559.101	0.455	0.077	0.461	0.108	0.445	0.002	0.076	0.010	0.012	0.005	0.078	1.111	0.001	0.106	0.011	0.107	0.096	558.295	559.844	0.882	0.033
DS5a	559.101	0.560	0.085	0.567	0.106	0.885	0.002	0.079	0.005	0.012	0.005	0.080	1.367	0.002	0.055	0.011	0.056	0.041	558.114	560.009	0.870	0.015
DS5b	559.101	0.469	0.074	0.475	0.158	0.491	0.001	0.020	0.011	0.012	0.005	0.026	1.157	0.001	0.125	0.011	0.125	0.108	558.243	559.860	0.880	0.036
DS5c	559.101	0.460	0.085	0.468	0.174	0.489	0.001	0.037	0.030	0.012	0.005	0.050	1.145	0.001	0.162	0.011	0.162	0.142	558.245	559.848	0.877	0.047
DS6a	559.101	0.456	0.044	0.458	0.191	0.463	0.001	0.069	0.025	0.012	0.005	0.075	1.123	0.000	0.041	0.011	0.042	0.038	558.255	559.830	0.875	0.014



Cut Name	Cut Description	$\langle \epsilon_{total} \rangle$	$\hat{\epsilon}_{total}$	$\langle \epsilon_{unique} \rangle$	$\hat{\epsilon}_{unique}$	Sacrifice	$\Delta DP$
Enriched Source Detector Cut	Any other detector: isBar	M1: 21.5 % M2: 40.6 %	23.0 <sup>+2.7</sup> <sub>-2.5</sub> % 63.8 <sup>+6.0</sup> <sub>-6.5</sub> %	4.0 % 7.7 %	3.0 <sup>+1.2</sup> <sub>-0.9</sub> % 15.5 <sup>+5.3</sup> <sub>-4.2</sub> %	1.6 % 3.5 %	17%
Multiplicity 2 Cut $m=2$	No other detector: ((energy>316.8)    (energy>329.8 && energy<366.6)    (energy>398.6 && energy<420.)    energy<466.6)    (energy>496.6 && energy<520.)    energy<566.6)    (energy>606.6 && energy<635.6)    (energy>1116.4 && energy<1121.6)    (energy>1144. && energy<1260.6)    (energy>205.2) && isBar)	M1: 15.0 % M2: 11.5 %	16.6 <sup>+2.4</sup> <sub>-2.2</sub> % 17.2 <sup>+5.5</sup> <sub>-4.4</sub> %	0.6 % 0.7 %	0.0 <sup>+0.4</sup> <sub>-0.0</sub> % 1.7 <sup>+2.7</sup> <sub>-1.1</sub> %	0.0 % 0.0 %	2%
Coincident Energy Cut	Not: ((sumE>975.6)    (sumE>888.4 && sumE>925.4)    (sumE>957.4 && sumE>975.6)    (sumE>1165.4 && sumE>1174.6)    (sumE>1330. && sumE>1333.6)    (sumE>1457. && sumE<1492.4)    (sumE>1702. && sumE<1819.4)    (sumE>1824.2)	M1: 61.7 % M2: 47.3 %	54.7 <sup>+3.1</sup> <sub>-3.0</sub> % 27.6 <sup>+6.2</sup> <sub>-5.5</sub> %	3.4 % 3.1 %	1.1 <sup>+0.9</sup> <sub>-0.5</sub> % 0.0 <sup>+1.7</sup> <sub>-0.0</sub> %	0.6 % 0.6 %	11%
Sum Energy Cut		M1: 76.1 % M2: 77.2 %	78.1 <sup>+2.4</sup> <sub>-2.6</sub> % 72.4 <sup>+2.5</sup> <sub>-6.2</sub> %	5.7 % 4.0 %	7.5 <sup>+1.8</sup> <sub>-1.5</sub> % 1.7 <sup>+2.7</sup> <sub>-1.1</sub> %	0.8 % 0.8 %	17%
Combined Cuts		M1: 89.9 % M2: 92.9 %	86.8 <sup>+1.9</sup> <sub>-2.2</sub> % 96.6 <sup>+1.7</sup> <sub>-3.3</sub> %	— —	31.0 % 35.1 %	84%	

TABLE XI Table of cut descriptions and efficiencies for simulated backgrounds and measured data for the 559 keV peak.

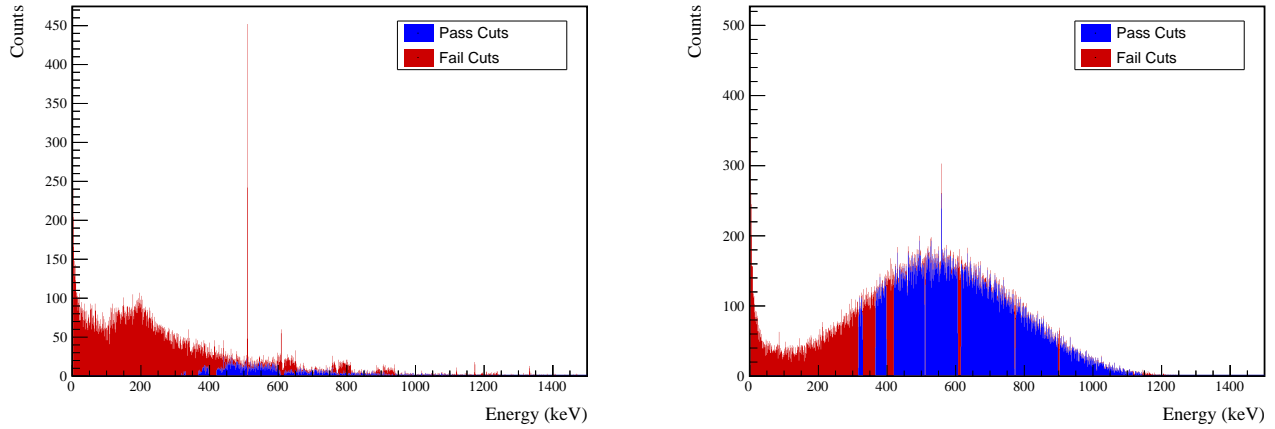


FIG. 42 Effect of 559 keV peak cuts on coincident energy spectra in BG (left) and ES (right) simulations.

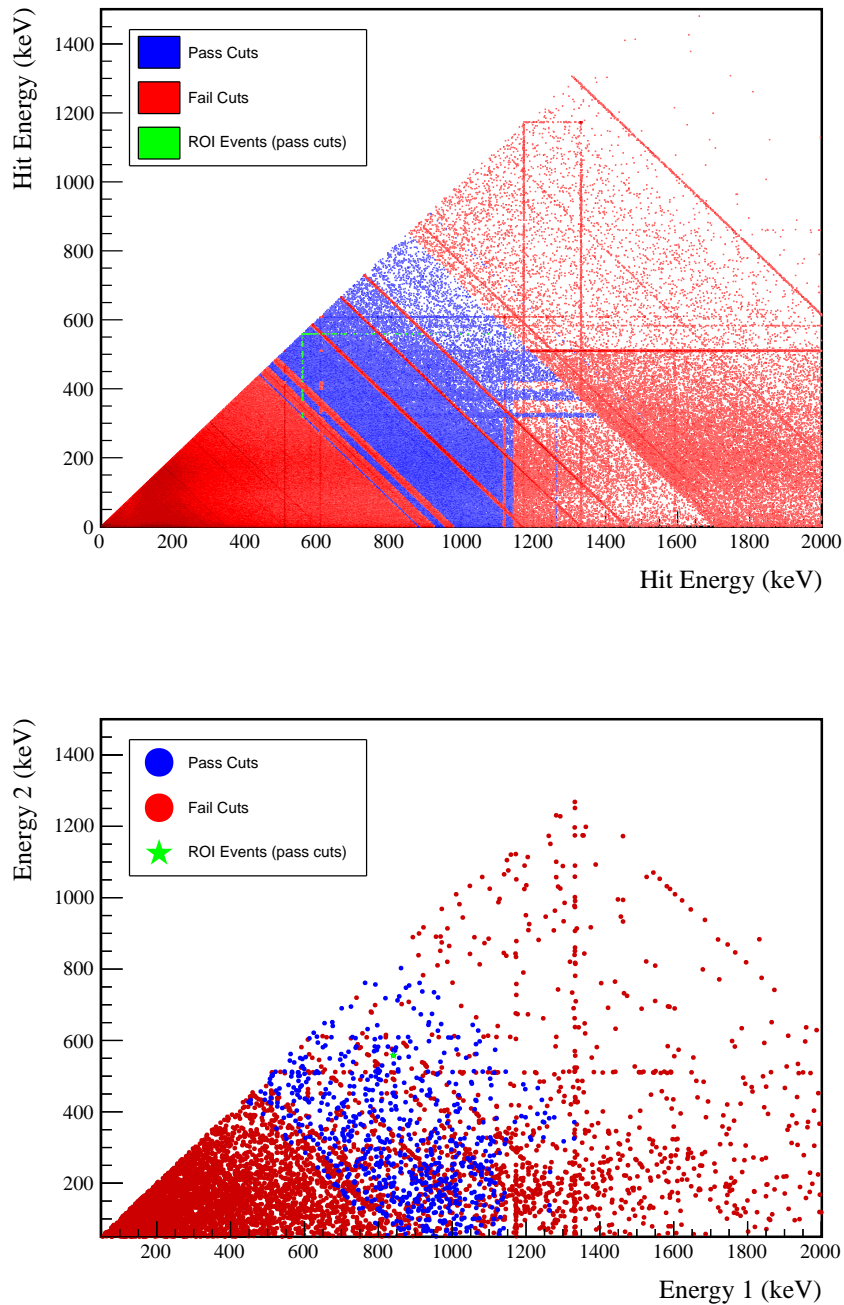
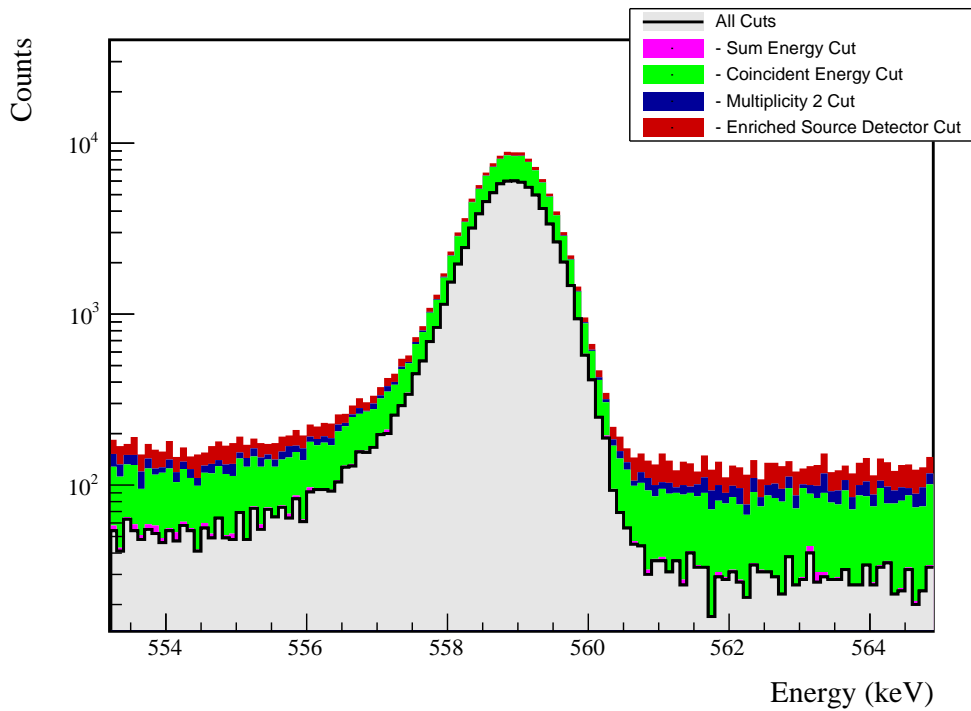


FIG. 43 Simulated (left) and measured (right) multiplicity 2 energy spectrum with sum and coincident energy cuts included for the 559 keV peak.

FIG. 44 Effect of all cuts applied sequentially on ROI for 559 keV peak of  $2\nu\beta\beta$  to  $2_1^+$ 

Source	Module 1 efficiency	Module 2 efficiency
Multi-Detector with Full Energy $\gamma$	$2.9 \pm 0.2\%$	$1.5 \pm 0.5\%$
Region of Interest	$87.4 \pm 2.0\%$	$87.4 \pm 2.0\%$
Dead Layer	$71.5 \pm 4.9\%$	$60.2 \pm 7.0\%$
Detector Dead Times	$98.3 \pm 0.8\%$	$98.6 \pm 0.7\%$
Enriched Source Detector Cut	$97.5 \pm < 0.1\%$	$94.1 \pm < 0.1\%$
Multiplicity 2 Cut	$99.5 \pm < 0.1\%$	$99.7 \pm < 0.1\%$
Coincident Energy Cut	$72.3 \pm 0.5\%$	$71.6 \pm 0.5\%$
Sum Energy Cut	$71.4 \pm 0.5\%$	$69.1 \pm 0.5\%$
Final Efficiency	$1.35 \pm 0.14\%$	$0.58 \pm 0.19\%$

FIG. 45 Table of detection efficiencies for the 559 keV peak.

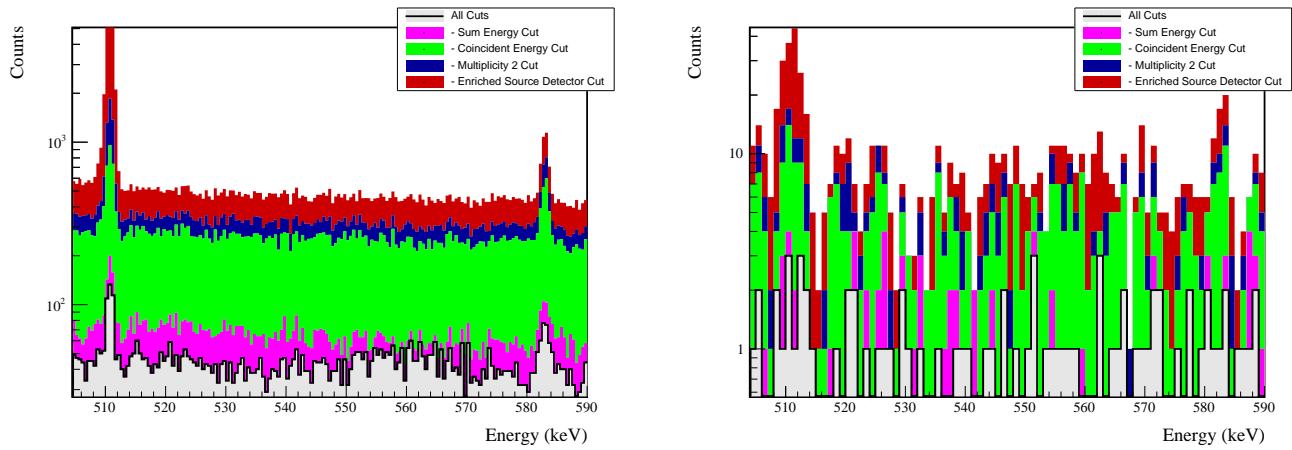
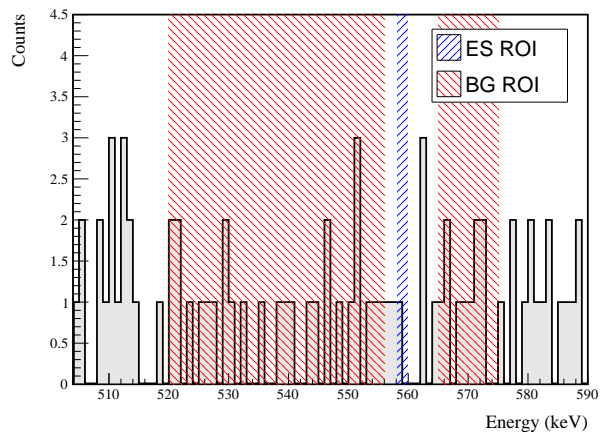


FIG. 46 Effect of all cuts applied to sequentially simulated (left) and measured (right) background data.

FIG. 47 All events after cuts in background (red) and signal (blue) ROIs for 559 keV peak of  $2\nu\beta\beta$  to  $2_1^+$

706 **Appendix D:  $2\nu\beta\beta$  to  $2_2^+$**

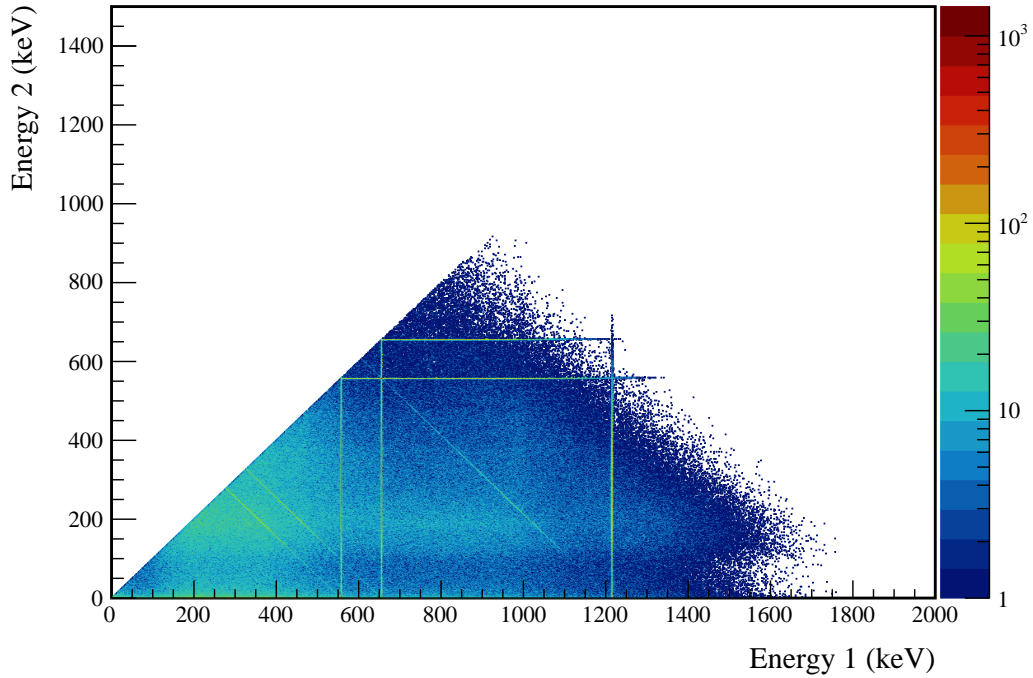


FIG. 48 Simulated multiplicity 2 energy spectrum of the  $2\nu\beta\beta$  to  $2_2^+$  decay mode

707 **1. 559 keV peak**

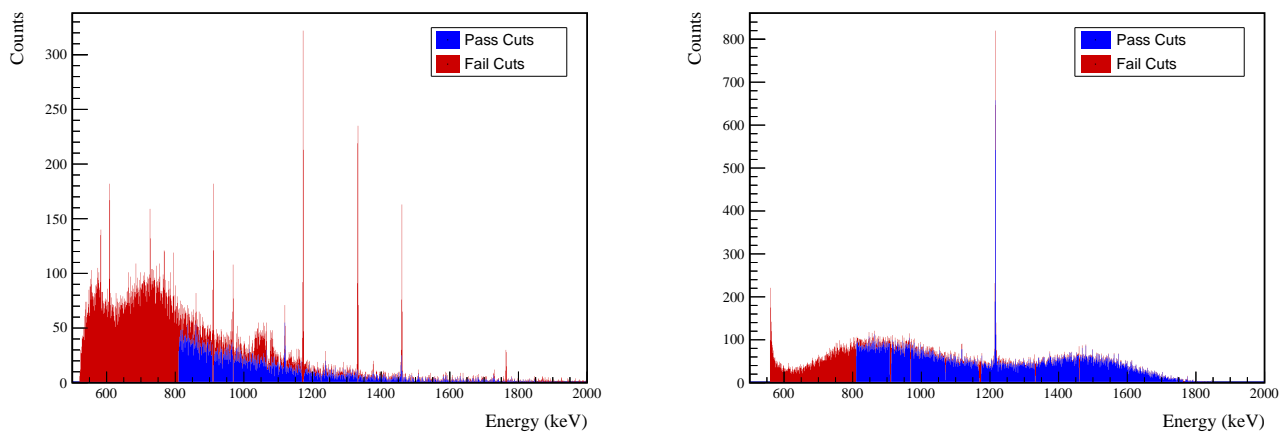


FIG. 49 Effect of 559 keV peak cuts on sum energy spectra in BG (left) and ES (right) simulations.



TABLE XII Table of energy estimation uncertainties for the 559 keV peak.

DS	$E_{peak}$ (keV)	$\sigma_{drift}$ (keV)	$\sigma_{fit}$ (keV)	$\sigma$ (keV)	$f_{t,fit}$	$\tau_{f,fit}$ (keV)	$\delta_{\mu,NL}$ (keV)	$\delta_{\mu,drift}$ (keV)	$\delta_{\mu,atalk}$ (keV)	$\delta_{\mu,peak}$ (keV)	$\delta_u$ (keV)	FWHM (keV)	$\delta_{fwhm,fit}$ (keV)	$\delta_{fwhm,drift}$ (keV)	$\delta_{fwhm,atalk}$ (keV)	$\delta_{FWHM}$ (keV)	$\delta_\alpha$	$E_{ROI,1}$ (keV)	$E_{ROI,2}$ (keV)	$\epsilon_{ROI}$	$\sigma_{e_{ROI}}$	
DS1	559.101	0.460	0.063	0.464	0.230	0.515	0.001	0.104	0.002	0.012	0.005	0.105	1.152	0.001	0.039	0.011	0.040	0.035	558.243	559.812	0.854	0.016
DS2	559.101	0.461	0.055	0.464	0.249	0.515	0.002	0.067	0.004	0.012	0.005	0.068	1.158	0.001	0.107	0.011	0.108	0.093	558.231	559.810	0.857	0.033
DS3	559.101	0.470	0.066	0.474	0.224	0.505	0.001	0.026	0.024	0.012	0.005	0.038	1.174	0.001	0.073	0.011	0.074	0.063	558.231	559.827	0.862	0.022
DS4	559.101	0.455	0.077	0.461	0.108	0.445	0.002	0.076	0.010	0.012	0.005	0.078	1.111	0.001	0.106	0.011	0.107	0.096	558.321	559.821	0.871	0.035
DS5a	559.101	0.560	0.085	0.567	0.106	0.885	0.002	0.079	0.005	0.012	0.005	0.080	1.367	0.002	0.055	0.011	0.056	0.041	558.145	559.981	0.859	0.015
DS5b	559.101	0.469	0.074	0.475	0.158	0.491	0.001	0.020	0.011	0.012	0.005	0.026	1.157	0.001	0.125	0.011	0.125	0.108	558.270	559.836	0.869	0.038
DS5c	559.101	0.460	0.085	0.468	0.174	0.489	0.001	0.037	0.030	0.012	0.005	0.050	1.145	0.001	0.162	0.011	0.162	0.142	558.273	559.824	0.866	0.050
DS6a	559.101	0.456	0.044	0.458	0.191	0.463	0.001	0.069	0.025	0.012	0.005	0.075	1.123	0.000	0.041	0.011	0.042	0.038	558.282	559.806	0.864	0.015



Cut Name	Cut Description	$\langle \epsilon_{total} \rangle$	$\hat{\epsilon}_{total}$	$\langle \epsilon_{unique} \rangle$	$\hat{\epsilon}_{unique}$	Sacrifice	$\Delta DP$
Enriched Source Detector Cut	Any other detector: isBar	M1: 21.5 %	$23.0^{+2.7}_{-2.5}$ %	6.1 %	$6.0^{+1.6}_{-1.3}$ %	1.8 %	10%
No other detector:	( ((energy<41.)    (energy>509.8 && energy<12.2)    (energy>608.2 && energy<12.6)    (energy>1208.4)    (energy>307.4)) && isBar )    ((energy<40.4)    (energy>259. && energy>513.2)    (energy>604. && energy>610.)    (energy>884.8) && isBar )	M2: 40.6 %	$63.8^{+6.0}_{-6.5}$ %	11.9 %	$17.2^{+5.5}_{-4.4}$ %	5.0 %	
Coincident Energy Cut	M1: 19.2 %	$20.8^{+2.6}_{-2.4}$ %	3.5 %	$2.3^{+1.1}_{-0.8}$ %	2.9 %	2.3 %	2%
	M2: 21.2 %	$32.8^{+6.4}_{-5.8}$ %	3.2 %	$5.2^{+3.7}_{-2.2}$ %	2.3 %		
Sum Energy Cut	M1: 61.2 %	$61.5 \pm 3.0$ %	36.0 %	$35.5^{+3.0}_{-2.9}$ %	16.4 %	17.2 %	18%
	M2: 62.3 %	$56.9^{+6.3}_{-6.6}$ %	27.0 %	$17.2^{+5.5}_{-4.4}$ %			
Combined Cuts	M1: 72.1 %	$71.3^{+2.7}_{-2.9}$ %	—	—	26.1 %	34.4 %	32%
	M2: 79.9 %	$86.2^{+3.9}_{-5.1}$ %					

TABLE XIII Table of cut descriptions and efficiencies for simulated backgrounds and measured data for the 559 keV peak.

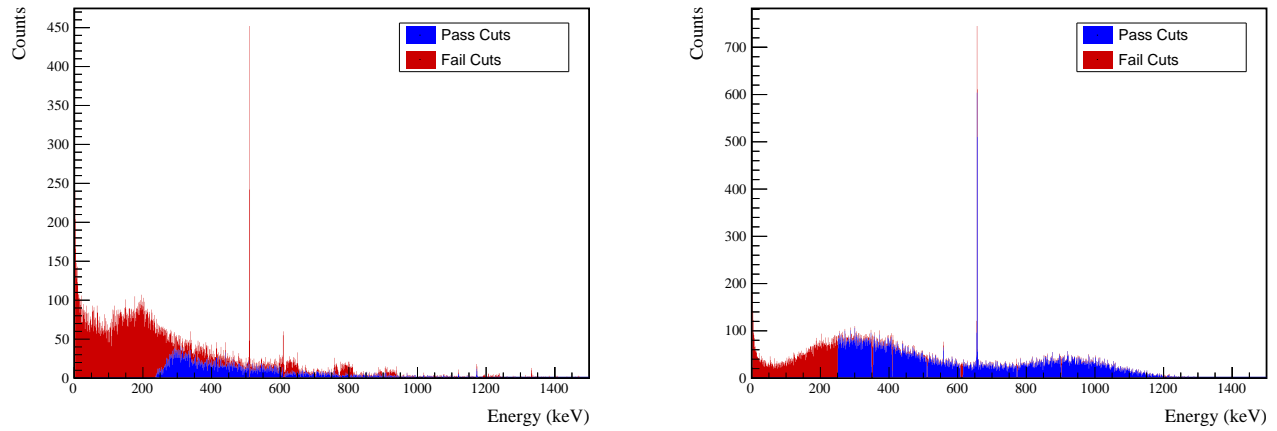


FIG. 50 Effect of 559 keV peak cuts on coincident energy spectra in BG (left) and ES (right) simulations.

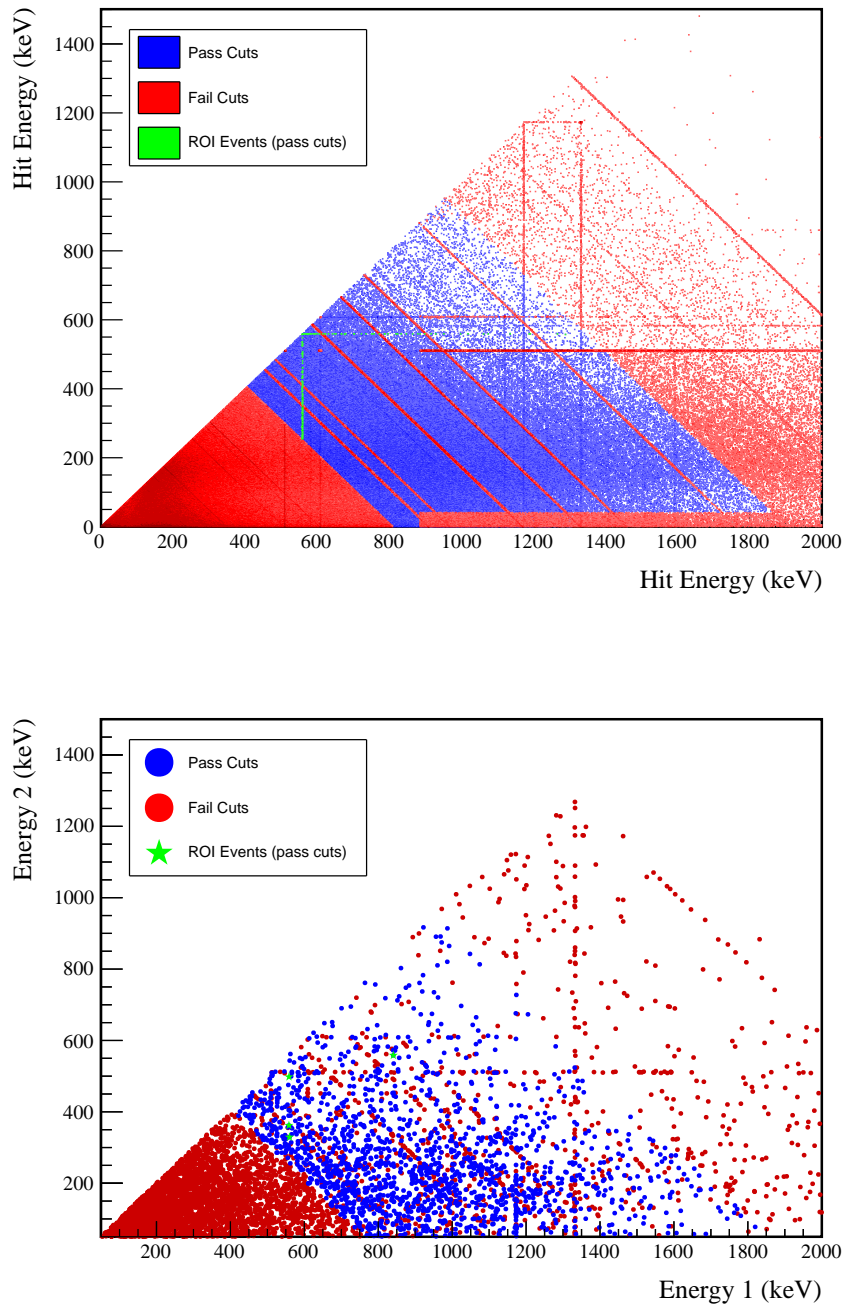
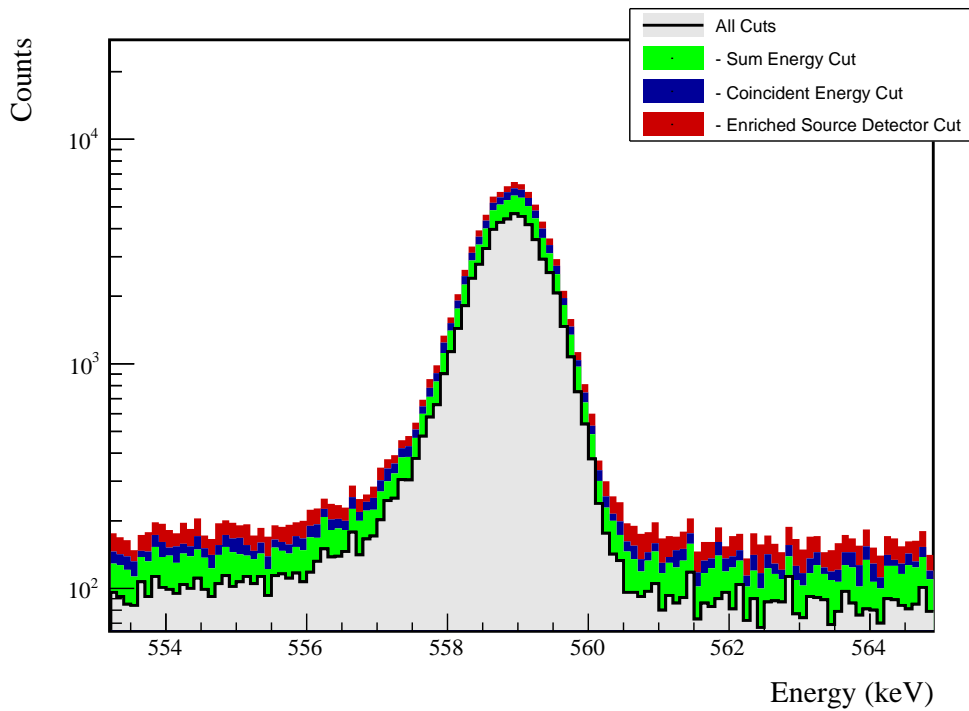


FIG. 51 Simulated (left) and measured (right) multiplicity 2 energy spectrum with sum and coincident energy cuts included for the 559 keV peak.

FIG. 52 Effect of all cuts applied sequentially on ROI for 559 keV peak of  $2\nu\beta\beta$  to  $2_2^+$ 

Source	Module 1 efficiency	Module 2 efficiency
Multi-Detector with Full Energy $\gamma$	$1.9 \pm 0.2\%$	$1.1 \pm 0.5\%$
Region of Interest Dead Layer	$86.2 \pm 2.1\%$	$86.2 \pm 2.1\%$
Detector Dead Times	$75.5 \pm 4.2\%$	$65.5 \pm 6.0\%$
Enriched Source Detector Cut	$98.4 \pm 0.8\%$	$98.6 \pm 0.7\%$
Coincident Energy Cut	$96.7 \pm <0.1\%$	$90.2 \pm <0.1\%$
Sum Energy Cut	$93.0 \pm 0.5\%$	$91.2 \pm 0.5\%$
Final Efficiency	$78.9 \pm 0.5\%$	$73.4 \pm 0.5\%$
	$0.98 \pm 0.12\%$	$0.44 \pm 0.20\%$

FIG. 53 Table of detection efficiencies for the 559 keV peak.

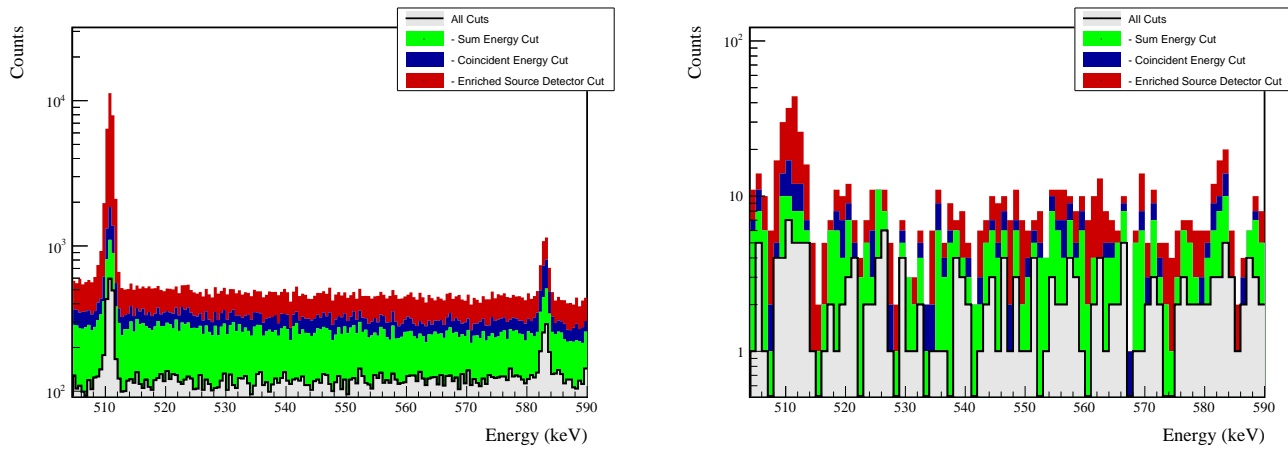
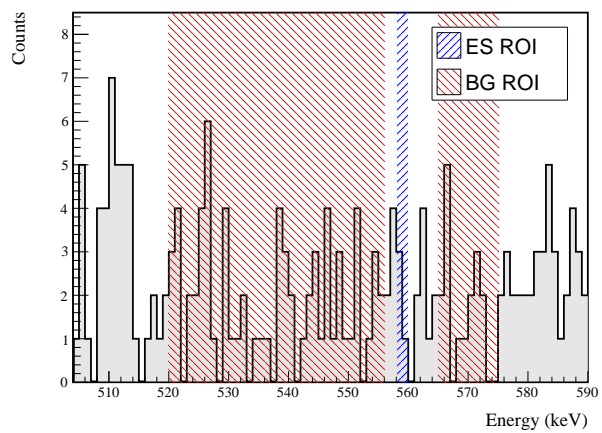


FIG. 54 Effect of all cuts applied to sequentially simulated (left) and measured (right) background data.

FIG. 55 All events after cuts in background (red) and signal (blue) ROIs for 559 keV peak of  $2\nu\beta\beta$  to  $2_2^+$



## 708 2. 657 keV peak

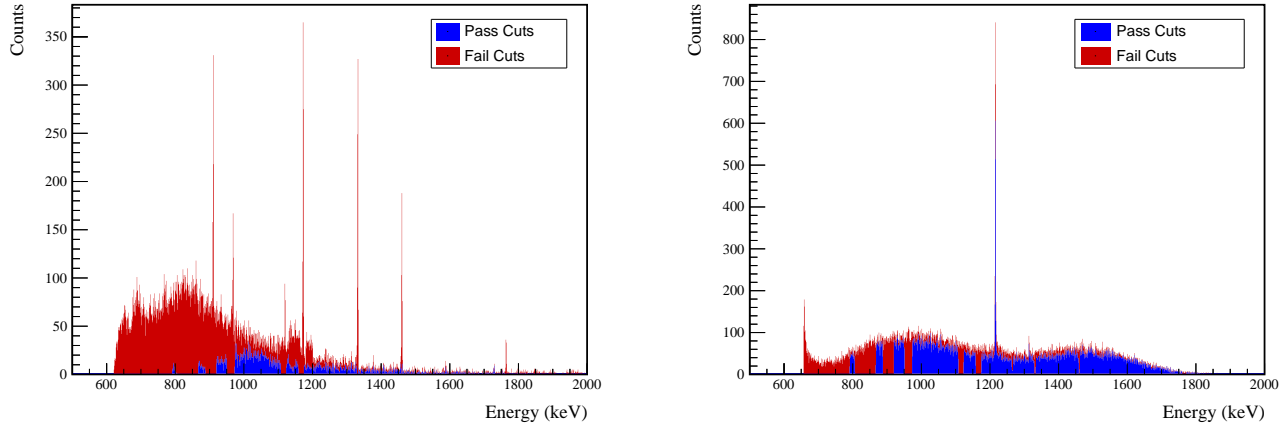


FIG. 56 Effect of 657 keV peak cuts on sum energy spectra in BG (left) and ES (right) simulations.

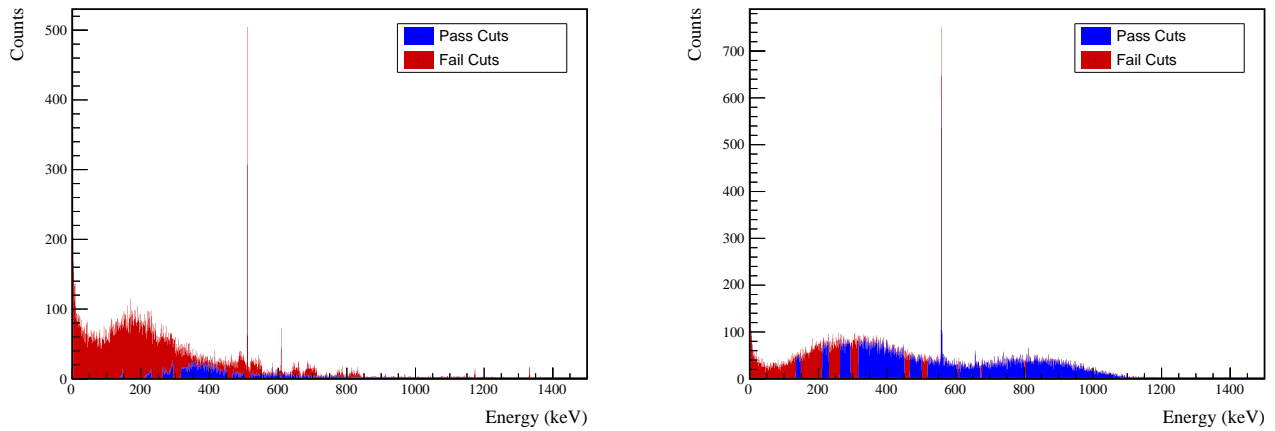


FIG. 57 Effect of 657 keV peak cuts on coincident energy spectra in BG (left) and ES (right) simulations.



TABLE XIV Table of energy estimation uncertainties for the 657 keV peak.

DS	$E_{peak}$ (keV)	$\sigma_{fit}$ (keV)	$\sigma_{drift}$ (keV)	$f_{t,fit}$	$\sigma$ (keV)	$\tau_{f,it}$ (keV)	$\delta_{\mu,f,it}$ (keV)	$\delta_{\mu,NL}$ (keV)	$\delta_{\mu,drift}$ (keV)	$\delta_{\mu,xtalk}$ (keV)	$\delta_u$ (keV)	FWHM	$\delta_{fwhm,fit}$ (keV)	$\delta_{fwhm,drift}$ (keV)	$\delta_{fwhm,xtalk}$ (keV)	$\delta_{FWHM}$ (keV)	$\delta_\alpha$	$E_{ROI,1}$ (keV)	$E_{ROI,2}$ (keV)	$\epsilon_{ROI}$	$\sigma_{e_{ROI}}$	
DS1	657.041	0.500	0.074	0.505	0.230	0.579	0.002	0.104	0.003	0.012	0.005	0.105	1.256	0.001	0.039	0.011	0.040	0.032	656.067	657.845	0.867	0.014
DS2	657.041	0.502	0.064	0.506	0.249	0.580	0.002	0.067	0.005	0.012	0.005	0.068	1.263	0.001	0.107	0.011	0.108	0.085	656.052	657.843	0.869	0.028
DS3	657.041	0.510	0.078	0.516	0.224	0.568	0.002	0.026	0.026	0.012	0.005	0.040	1.278	0.001	0.073	0.011	0.074	0.058	656.056	657.862	0.874	0.019
DS4	657.041	0.493	0.090	0.501	0.108	0.490	0.002	0.076	0.076	0.012	0.005	0.078	1.207	0.001	0.106	0.011	0.107	0.088	656.161	657.852	0.884	0.030
DS5a	657.041	0.606	0.100	0.614	0.106	0.924	0.002	0.079	0.006	0.012	0.005	0.080	1.481	0.002	0.055	0.011	0.056	0.038	655.966	658.029	0.872	0.013
DS5b	657.041	0.509	0.087	0.517	0.158	0.562	0.001	0.020	0.013	0.012	0.005	0.027	1.259	0.001	0.125	0.011	0.125	0.100	656.101	657.871	0.880	0.033
DS5c	657.041	0.500	0.100	0.510	0.174	0.555	0.002	0.037	0.035	0.012	0.005	0.053	1.247	0.001	0.162	0.011	0.162	0.130	656.102	657.859	0.878	0.043
DS6a	657.041	0.495	0.051	0.497	0.191	0.524	0.001	0.069	0.030	0.012	0.005	0.076	1.221	0.001	0.041	0.011	0.042	0.035	656.115	657.837	0.876	0.013



Cut Name	Cut Description	$\langle \epsilon_{total} \rangle$	$\hat{\epsilon}_{total}$	$\langle \epsilon_{unique} \rangle$	$\hat{\epsilon}_{unique}$	Sacrifice	$\Delta DP$
Enriched Source Detector Cut	Any other detector: isBar	M1: 22.2 % M2: 41.6 %	23.4 <sup>+2.9</sup> <sub>-2.7</sub> % 59.7 <sup>+2.6</sup> <sub>-5.9</sub> %	6.1 % 11.8 %	5.2 <sup>+1.7</sup> <sub>-1.3</sub> % 15.3 <sup>+4.7</sup> <sub>-3.8</sub> %	1.4 % 4.5 %	17%
Coincident Energy Cut	No other detector: ((energy<48.)    (energy>100.4 && energy<134.4)    (energy>148.8 && energy<209.8)    (energy>230.8 && energy<262.6)    (energy>294.4 && energy<316.4)    (energy>345.6 && energy<466.6)    (energy>492.2 && energy<517.2)    (energy>566.4 && energy<610.4)    (energy>1156.6) && isBar)    ((energy<41.6)    (energy>483.2 && energy<520.2)    (energy>579.8) && !isBar))    ((energy<41.6)    (energy>897.6)    (sumE>806.2 && sumE<897.6)    (sumE>920.)    (sumE>950.8 && sumE<973.4)    (sumE>108.6 && sumE>1108.6)    (sumE>1123.2)    (sumE>1158.6 && sumE<1174.6)    (sumE>1333.6)    (sumE>1458.6 && sumE<1461.8)    (sumE>1771.6)    (sumE>1953.6))	M1: 48.2 % M2: 43.9 %	50.6 ± 3.3 % 38.9 <sup>+5.9</sup> <sub>-5.6</sub> %	14.7 % 11.7 %	19.9 <sup>+2.8</sup> <sub>-2.5</sub> % 9.7 <sup>+4.1</sup> <sub>-3.0</sub> %	12.3 % 7.2 %	15%
Sum Energy Cut		M1: 62.0 % M2: 61.9 %	60.2 ± 3.3 % 66.7 <sup>+5.3</sup> <sub>-5.8</sub> %	20.2 % 14.1 %	20.8 <sup>+2.8</sup> <sub>-2.5</sub> % 12.5 <sup>+4.4</sup> <sub>-3.4</sub> %	3.5 % 3.7 %	34%
Combined Cuts		M1: 84.8 % M2: 88.7 %	87.0 <sup>+2.1</sup> <sub>-2.4</sub> % 95.8 <sup>+1.8</sup> <sub>-3.0</sub> %	— —	39.7 % 43.3 %	36%	

TABLE XV Table of cut descriptions and efficiencies for simulated backgrounds and measured data for the 657 keV peak.

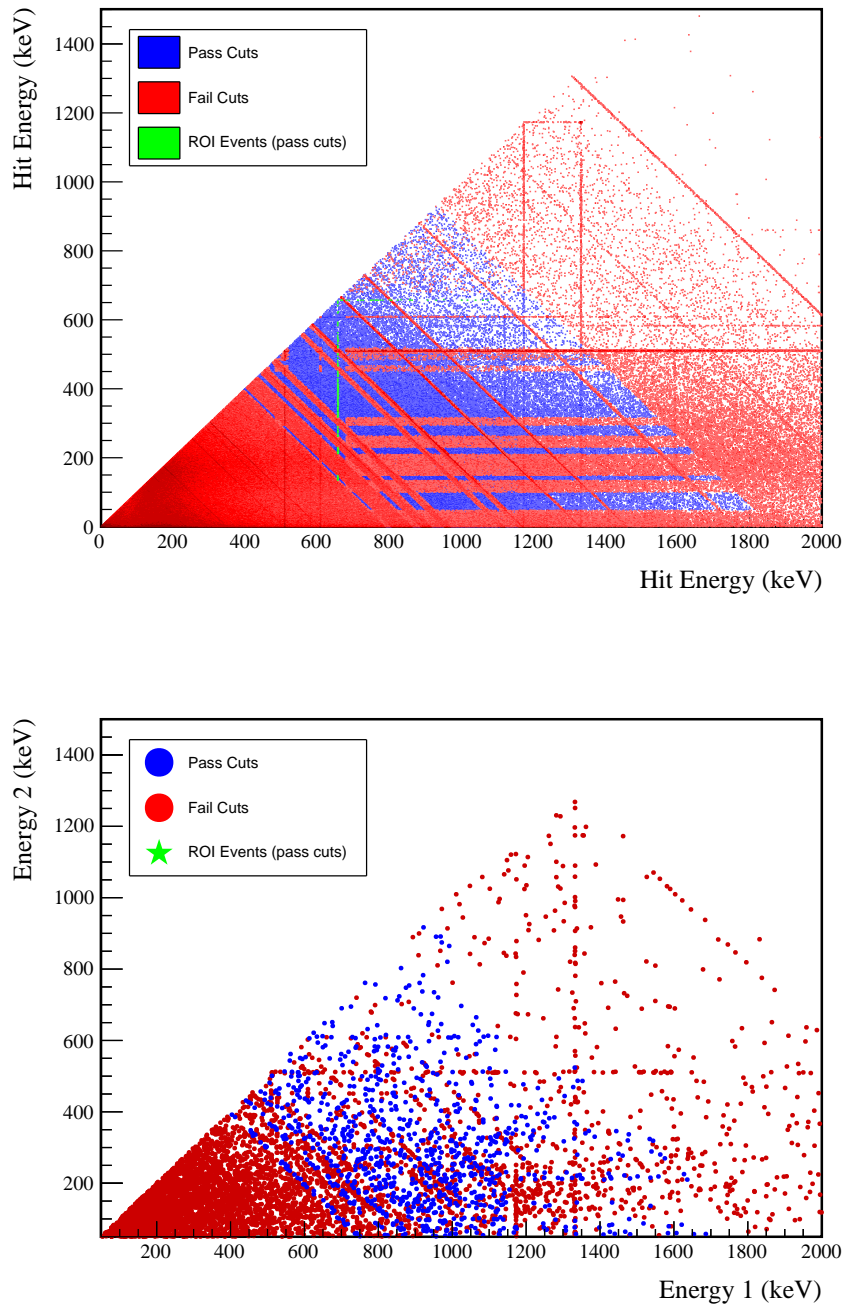
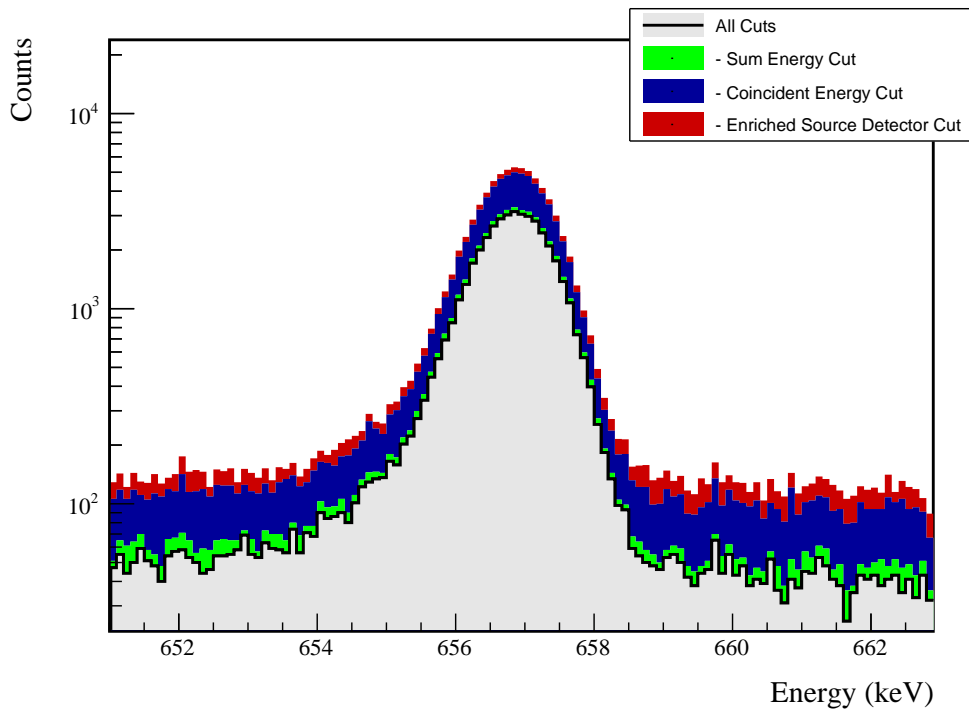


FIG. 58 Simulated (left) and measured (right) multiplicity 2 energy spectrum with sum and coincident energy cuts included for the 657 keV peak.

FIG. 59 Effect of all cuts applied sequentially on ROI for 657 keV peak of  $2\nu\beta\beta$  to  $2_2^+$ 

Source	Module 1 efficiency	Module 2 efficiency
Multi-Detector with Full Energy $\gamma$	$1.8 \pm 0.2\%$	$1.0 \pm 0.5\%$
Region of Interest Dead Layer	$87.5 \pm 1.8\%$	$87.5 \pm 1.8\%$
Detector Dead Times	$76.0 \pm 4.1\%$	$64.8 \pm 6.2\%$
Enriched Source Detector Cut	$96.8 \pm <0.1\%$	$89.8 \pm <0.1\%$
Coincident Energy Cut	$66.2 \pm 0.5\%$	$68.6 \pm 0.5\%$
Sum Energy Cut	$74.6 \pm 0.5\%$	$69.4 \pm 0.5\%$
Final Efficiency	$0.75 \pm 0.10\%$	$0.34 \pm 0.17\%$

FIG. 60 Table of detection efficiencies for the 657 keV peak.

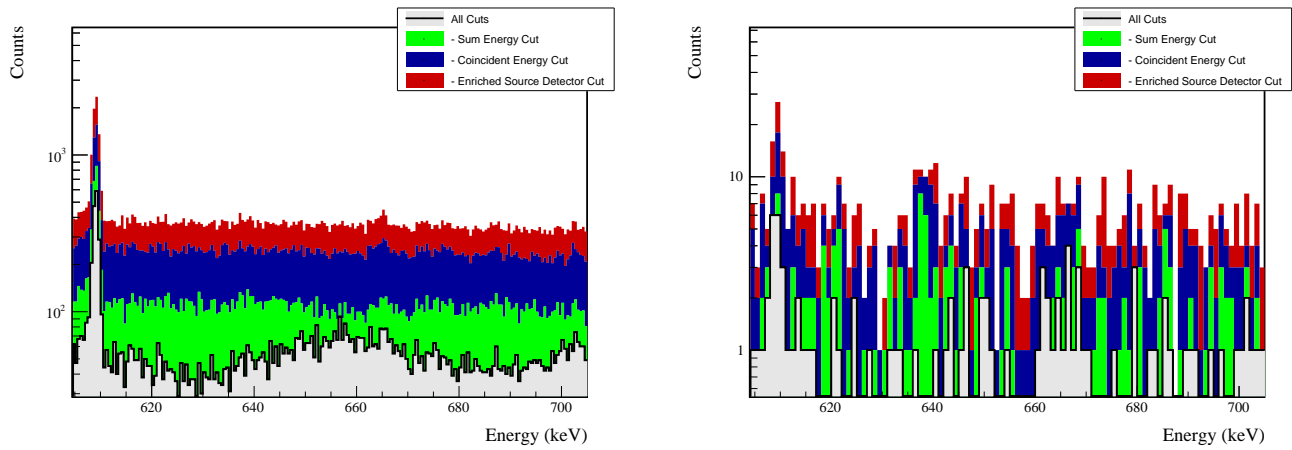
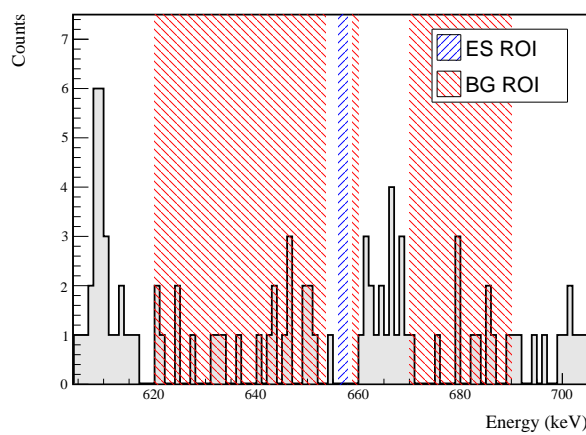


FIG. 61 Effect of all cuts applied to sequentially simulated (left) and measured (right) background data.

FIG. 62 All events after cuts in background (red) and signal (blue) ROIs for 657 keV peak of  $2\nu\beta\beta$  to  $2_2^+$



## 709 3. 1216 keV peak

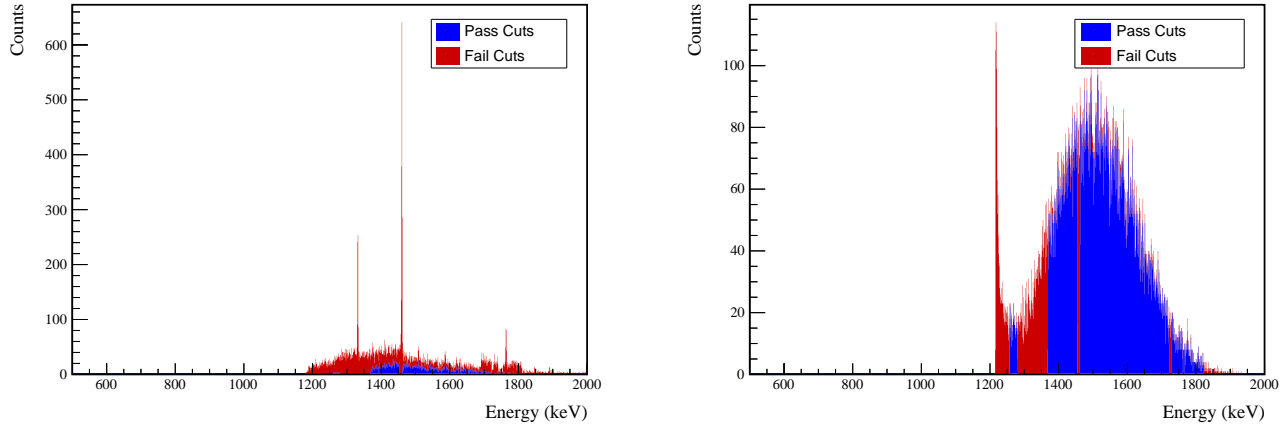


FIG. 63 Effect of 1216 keV peak cuts on sum energy spectra in BG (left) and ES (right) simulations.

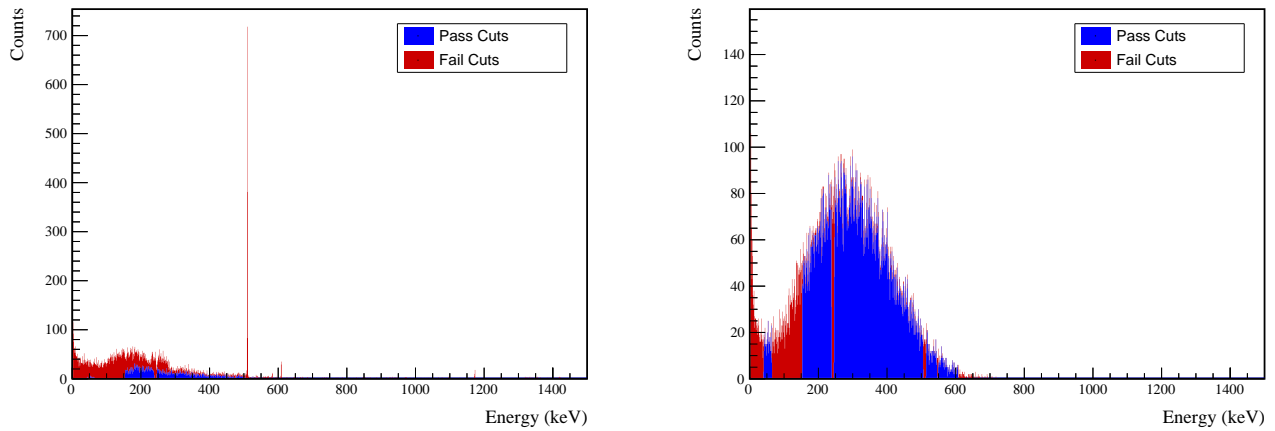


FIG. 64 Effect of 1216 keV peak cuts on coincident energy spectra in BG (left) and ES (right) simulations.



TABLE XVI Table of energy estimation uncertainties for the 1216 keV peak.

DS	$E_{peak}$ (keV)	$\sigma_{f_{fit}}$ (keV)	$\sigma_{drift}$ (keV)	$\sigma$ (keV)	$f_{t,f_{fit}}$	$\tau_{f_{fit}}$ (keV)	$\delta_{\mu,f_{fit}}$ (keV)	$\delta_{\mu,NL}$ (keV)	$\delta_{\mu,drift}$ (keV)	$\delta_{\mu,x talk}$ (keV)	$\delta_{\mu,peak}$ (keV)	$\delta_{\mu}$ (keV)	FWHM	$\delta_{fwhm,fit}$ (keV)	$\delta_{fwhm,drift}$ (keV)	$\delta_{fwhm,x talk}$ (keV)	$\delta_{FWHM}$ (keV)	$E_{ROI,1}$ (keV)	$E_{ROI,2}$ (keV)	$\epsilon_{ROI}$	$\sigma_{\epsilon_{ROI}}$	
DS1	1216.104	0.705	0.137	0.718	0.230	0.945	0.003	0.104	0.005	0.012	0.020	0.107	1.787	0.001	0.039	0.011	0.040	0.023	1214.713	1217.245	0.862	0.009
DS2	1216.104	0.710	0.119	0.720	0.249	0.951	0.003	0.067	0.008	0.012	0.020	0.072	1.803	0.001	0.107	0.011	0.108	0.060	1214.686	1217.245	0.862	0.020
DS3	1216.104	0.715	0.144	0.729	0.224	0.925	0.003	0.026	0.051	0.012	0.020	0.062	1.812	0.001	0.073	0.011	0.074	0.041	1214.702	1217.263	0.867	0.014
DS4	1216.104	0.697	0.167	0.717	0.108	0.746	0.003	0.076	0.022	0.012	0.020	0.083	1.726	0.001	0.106	0.011	0.107	0.062	1214.847	1217.261	0.884	0.021
DS5a	1216.104	0.838	0.185	0.859	0.106	1.316	0.004	0.079	0.012	0.012	0.020	0.083	2.070	0.002	0.055	0.011	0.056	0.027	1214.604	1217.483	0.872	0.009
DS5b	1216.104	0.716	0.161	0.734	0.158	0.963	0.002	0.020	0.024	0.012	0.020	0.039	1.791	0.001	0.125	0.011	0.125	0.070	1214.764	1217.282	0.873	0.023
DS5c	1216.104	0.703	0.185	0.727	0.174	0.932	0.003	0.037	0.066	0.012	0.020	0.079	1.783	0.001	0.162	0.011	0.162	0.091	1214.759	1217.269	0.871	0.030
DS6a	1216.104	0.693	0.095	0.700	0.191	0.873	0.002	0.069	0.055	0.012	0.020	0.092	1.723	0.001	0.041	0.011	0.042	0.025	1214.792	1217.224	0.870	0.009



Cut Name	Cut Description	$\langle \epsilon_{total} \rangle$	$\hat{\epsilon}_{total}$	$\langle \epsilon_{unique} \rangle$	$\hat{\epsilon}_{unique}$	Sacrifice	$\Delta D_P$
Enriched Source		M1: 25.2 %	24.7 <sup>+3.5</sup> / <sub>-2.2</sub> %	13.6 %	10.5 <sup>+2.7</sup> / <sub>-2.2</sub> %	2.1 %	23%
Detector Cut	Any other detector: <code>iEar</code>	M2: 41.8 %	61.9 <sup>+7.1</sup> / <sub>-7.7</sub> %	23.7 %	33.3 <sup>+7.6</sup> / <sub>-6.8</sub> %	5.0 %	
Multiplicity 2 Cut	<code>n==2</code>	M1: 14.8 %	19.8 <sup>+3.3</sup> / <sub>-2.9</sub> %	3.5 %	2.5 <sup>+1.5</sup> / <sub>-1.0</sub> %	0.1 %	5%
Coincident Energy Cut	No other detector: <code>((energy&lt;40.3)    (energy&gt;34.6 &amp;&amp; energy&lt;153.2)    (energy&gt;238.8 &amp;&amp; energy&lt;245.8)    (energy&gt;505.2 &amp;&amp; energy&lt;613.6)    (energy&gt;1287.)    (energy&gt;607.)) &amp;&amp; iEar -&gt; 1</code> Note: <code>(sumE&lt;1281.8 &amp;&amp; sumE&lt;1368.4)    (sumE&gt;1454.2 &amp;&amp; sumE&lt;1462.6)    (sumE&gt;1721.6 &amp;&amp; sumE&lt;1730.2)    (sumE&gt;1761.8 &amp;&amp; sumE&lt;1766.)    (sumE&gt;1822.8)    (sumE&gt;1822.8)</code>	M1: 36.0 %	39.5 <sup>+3.9</sup> / <sub>-3.8</sub> %	10.8 %	7.4 <sup>+2.3</sup> / <sub>-1.8</sub> %	0.2 %	16%
Sum Energy Cut		M2: 27.7 %	19.0 <sup>+6.8</sup> / <sub>-5.3</sub> %	9.4 %	7.1 <sup>+5.0</sup> / <sub>-3.1</sub> %	0.2 %	
Combined Cuts		M1: 44.2 %	47.5 <sup>+3.9</sup> / <sub>-3.9</sub> %	11.4 %	7.4 <sup>+2.3</sup> / <sub>-1.8</sub> %	0.6 %	14%
		M2: 38.7 %	40.5 <sup>+7.7</sup> / <sub>-7.3</sub> %	6.7 %	0.0 <sup>+2.3</sup> / <sub>-0.0</sub> %	0.6 %	
		M1: 77.8 %	74.7 <sup>+3.3</sup> / <sub>-3.6</sub> %	—	—	20.7 %	48%
		M2: 80.1 %	83.3 <sup>+3.6</sup> / <sub>-6.5</sub> %	—	—	24.9 %	

TABLE XVII Table of cut descriptions and efficiencies for simulated backgrounds and measured data for the 1216 keV peak.

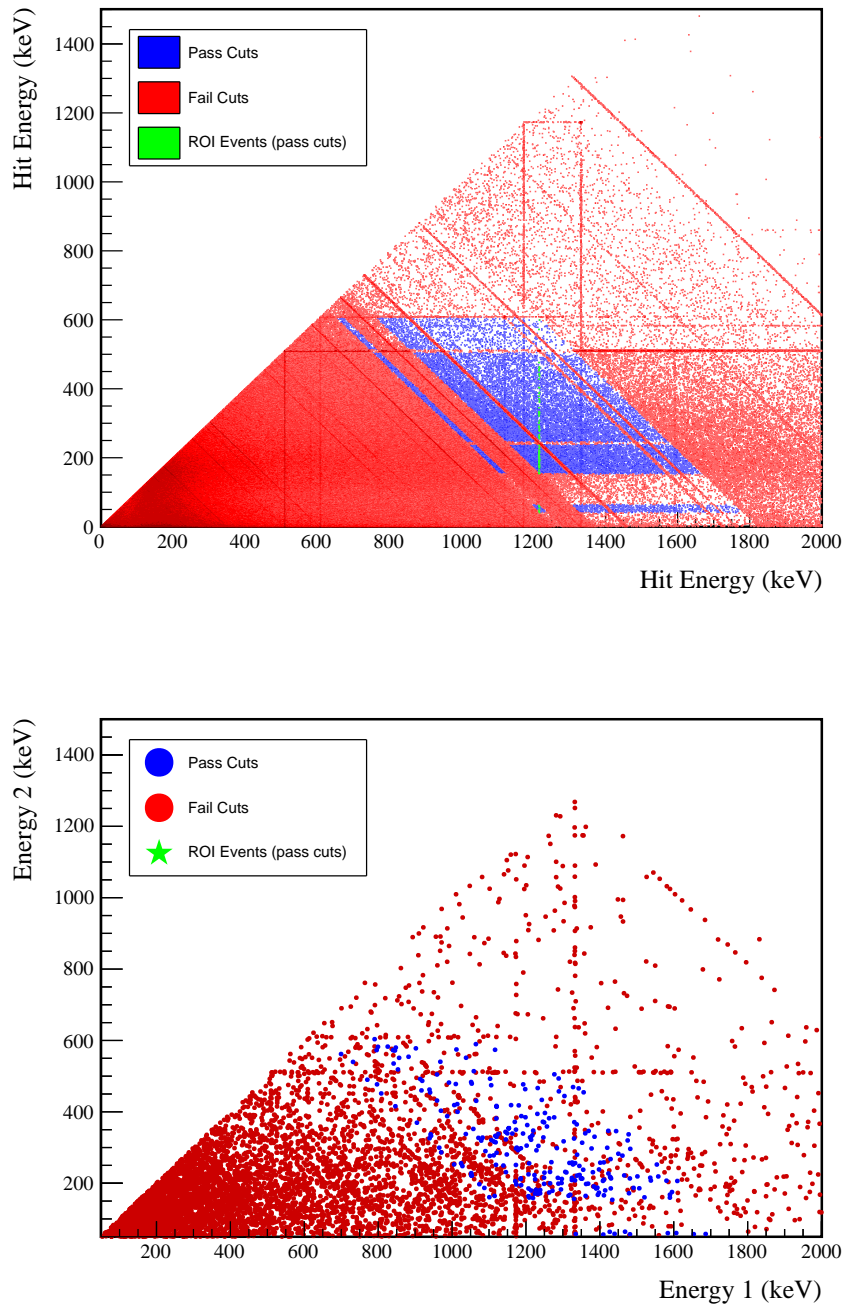
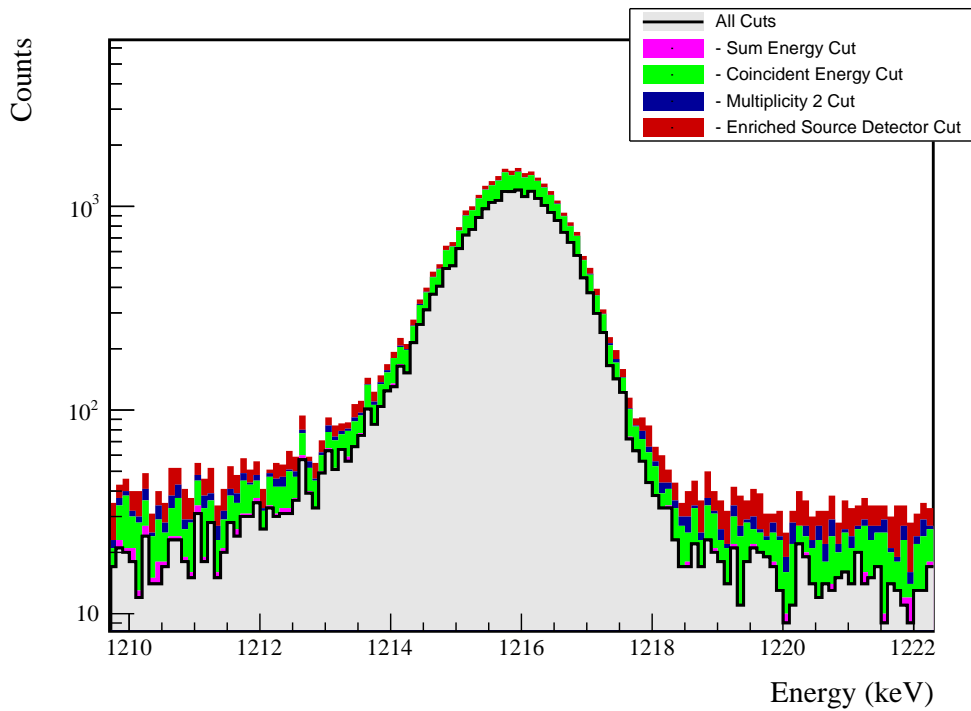


FIG. 65 Simulated (left) and measured (right) multiplicity 2 energy spectrum with sum and coincident energy cuts included for the 1216 keV peak.

FIG. 66 Effect of all cuts applied sequentially on ROI for 1216 keV peak of  $2\nu\beta\beta$  to  $2_2^+$ 

Source	Module 1 efficiency	Module 2 efficiency
Multi-Detector with Full Energy $\gamma$	$0.8 \pm 0.2\%$	$0.4 \pm 0.5\%$
Region of Interest	$87.0 \pm 1.3\%$	$87.0 \pm 1.3\%$
Dead Layer	$73.7 \pm 4.5\%$	$61.8 \pm 6.7\%$
Detector Dead Times	$98.3 \pm 0.8\%$	$98.6 \pm 0.6\%$
Enriched Source Detector Cut	$97.3 \pm < 0.1\%$	$93.3 \pm < 0.1\%$
Multiplicity 2 Cut	$99.6 \pm < 0.1\%$	$99.8 \pm < 0.1\%$
Coincident Energy Cut	$82.7 \pm 0.5\%$	$82.5 \pm 0.5\%$
Sum Energy Cut	$82.0 \pm 0.5\%$	$80.5 \pm 0.5\%$
Final Efficiency	$0.41 \pm 0.11\%$	$0.17 \pm 0.21\%$

FIG. 67 Table of detection efficiencies for the 1216 keV peak.

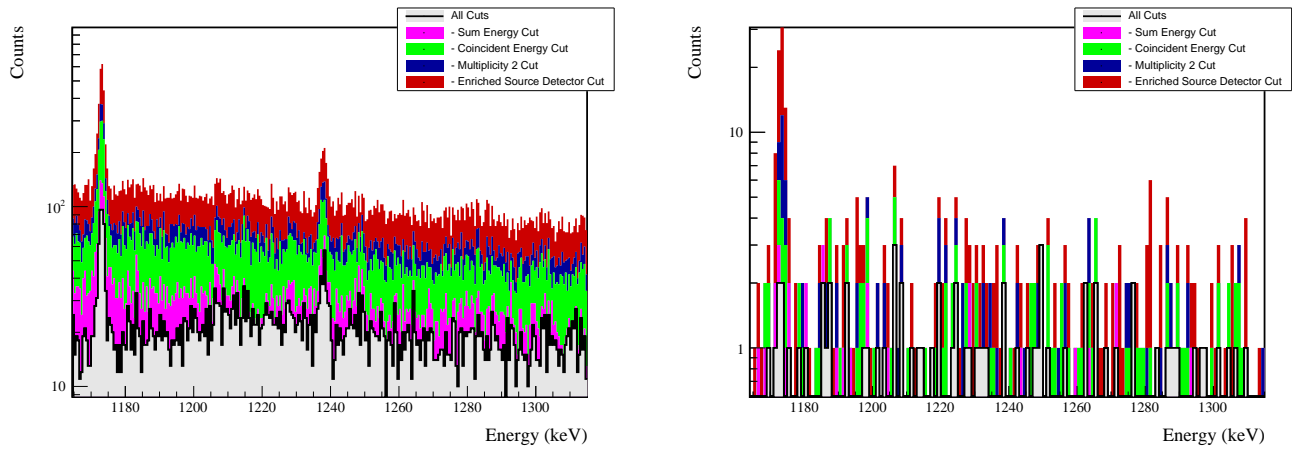
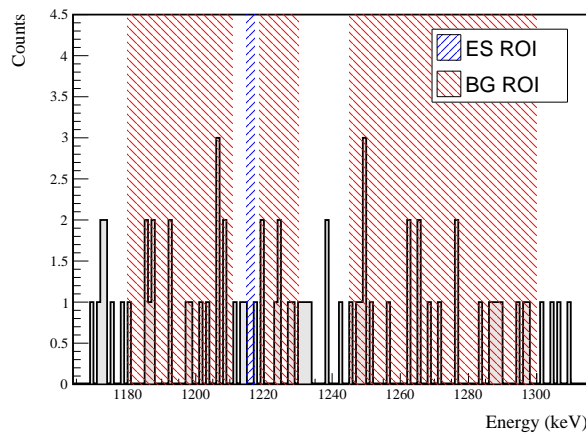
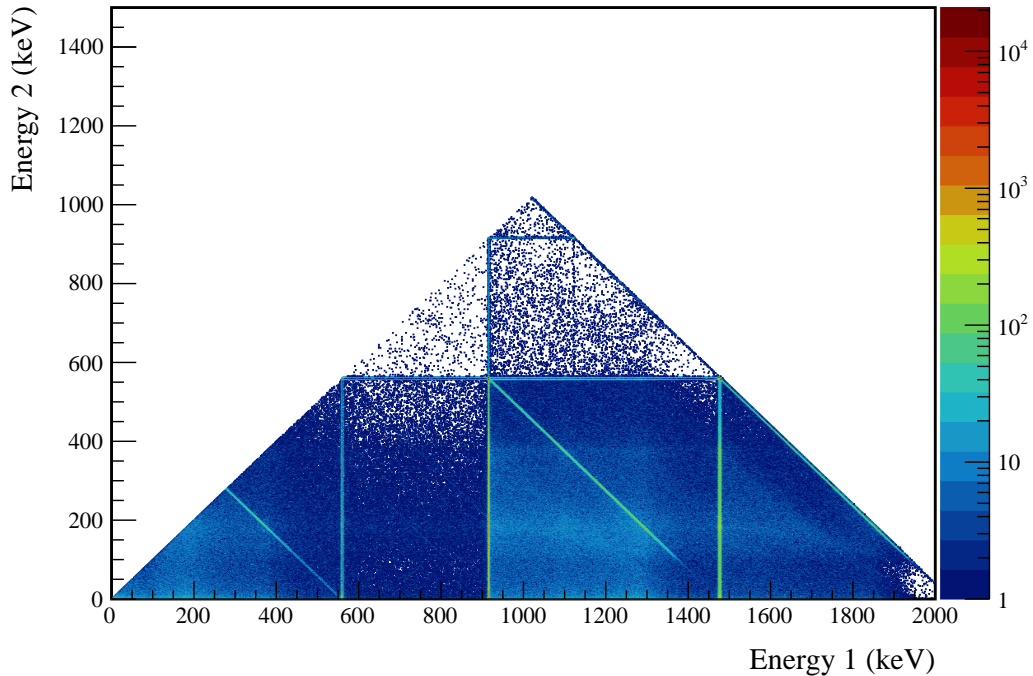


FIG. 68 Effect of all cuts applied to sequentially simulated (left) and measured (right) background data.

FIG. 69 All events after cuts in background (red) and signal (blue) ROIs for 1216 keV peak of  $2\nu\beta\beta$  to  $2_2^+$

**710 Appendix E:  $0\nu\beta\beta$  to  $0_1^+$** 

711 Note that both the 559 and 563 keV peaks will be shown together since they use the same sets of cuts.



712 FIG. 70 Simulated multiplicity 2 energy spectrum of the  $0\nu\beta\beta$  to  $0_1^+$  decay mode

713

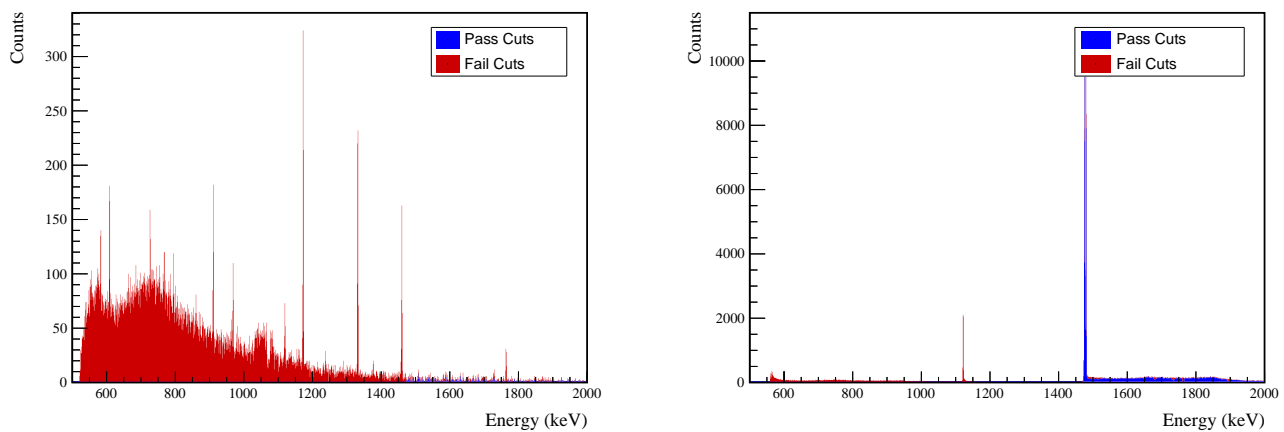


FIG. 71 Effect of 559 and 563 keV peaks cuts on sum energy spectra in BG (left) and ES (right) simulations.



TABLE XVIII Table of energy estimation uncertainties for the 559 and 563 keV peaks.

DS	$E_{peak}$ (keV)	$\sigma_{fit}$ (keV)	$\sigma_{drift}$ (keV)	$\sigma$ (keV)	$f_{t,fit}$ (keV)	$f_{t,fit}$ (keV)	$\tau_{fit}$ (keV)	$\delta_{\mu,fit}$ (keV)	$\delta_{\mu,NL}$ (keV)	$\delta_{\mu,drift}$ (keV)	$\delta_{\mu,peak}$ (keV)	$\delta_u$ (keV)	FWHM (keV)	$\delta_{fwhm,drift}$ (keV)	$\delta_{fwhm,fit}$ (keV)	$\delta_{fwhm,x talk}$ (keV)	$\delta_{FWHM}$ (keV)	$\delta_\alpha$	$E_{ROI,1}$ (keV)	$E_{ROI,2}$ (keV)	$\sigma_{e_{ROI}}$	
DS1	559.101	0.460	0.063	0.464	0.230	0.515	0.001	0.104	0.002	0.012	0.005	0.105	1.152	0.001	0.039	0.001	0.040	0.035	558.141	559.892	0.891	0.014
DS2	559.101	0.461	0.055	0.464	0.249	0.515	0.002	0.067	0.004	0.012	0.005	0.068	1.158	0.001	0.107	0.011	0.108	0.093	558.125	559.891	0.894	0.027
DS3	559.101	0.470	0.066	0.474	0.224	0.505	0.001	0.026	0.024	0.012	0.005	0.038	1.174	0.001	0.073	0.011	0.074	0.063	558.128	559.909	0.898	0.019
DS4	559.101	0.455	0.077	0.461	0.108	0.445	0.002	0.076	0.010	0.012	0.005	0.078	1.111	0.001	0.106	0.011	0.107	0.096	558.233	559.901	0.907	0.029
DS5a	559.101	0.560	0.085	0.567	0.106	0.855	0.002	0.079	0.005	0.012	0.005	0.080	1.367	0.002	0.055	0.011	0.056	0.041	558.036	560.077	0.894	0.013
DS5b	559.101	0.469	0.074	0.475	0.158	0.491	0.001	0.020	0.011	0.012	0.005	0.026	1.157	0.001	0.125	0.011	0.125	0.108	558.175	559.918	0.904	0.032
DS5c	559.101	0.460	0.085	0.468	0.174	0.489	0.001	0.037	0.030	0.012	0.005	0.050	1.145	0.001	0.162	0.011	0.162	0.142	558.176	559.905	0.902	0.042
DS6a	559.101	0.456	0.044	0.458	0.191	0.463	0.001	0.069	0.025	0.012	0.005	0.075	1.123	0.000	0.041	0.011	0.042	0.038	558.187	559.886	0.900	0.012
DS1	563.178	0.461	0.064	0.466	0.230	0.518	0.001	0.104	0.002	0.012	0.005	0.105	1.156	0.001	0.039	0.011	0.040	0.035	562.214	563.972	0.891	0.013
DS2	563.178	0.463	0.055	0.466	0.249	0.517	0.002	0.067	0.004	0.012	0.005	0.068	1.162	0.001	0.107	0.011	0.108	0.093	562.198	563.971	0.893	0.027
DS3	563.178	0.471	0.066	0.476	0.224	0.508	0.001	0.026	0.024	0.012	0.005	0.038	1.179	0.001	0.073	0.011	0.074	0.063	562.202	563.989	0.898	0.019
DS4	563.178	0.457	0.077	0.463	0.108	0.447	0.002	0.076	0.010	0.012	0.005	0.078	1.115	0.001	0.106	0.011	0.107	0.096	562.307	563.980	0.907	0.029
DS5a	563.178	0.562	0.086	0.569	0.106	0.858	0.002	0.079	0.006	0.012	0.005	0.080	1.372	0.002	0.055	0.011	0.056	0.041	562.109	564.157	0.894	0.013
DS5b	563.178	0.471	0.074	0.477	0.158	0.494	0.001	0.020	0.011	0.012	0.005	0.026	1.162	0.001	0.125	0.011	0.125	0.108	562.248	563.998	0.904	0.032
DS5c	563.178	0.462	0.086	0.470	0.174	0.492	0.001	0.037	0.030	0.012	0.005	0.050	1.49	0.001	0.162	0.011	0.162	0.141	562.250	563.985	0.902	0.041
DS6a	563.178	0.457	0.044	0.459	0.191	0.465	0.001	0.069	0.026	0.012	0.005	0.075	1.127	0.000	0.041	0.011	0.042	0.038	562.260	563.965	0.900	0.012



Cut Name	Cut Description	$\langle \epsilon_{total} \rangle$	$\hat{\epsilon}_{total}$	$\langle \epsilon_{unique} \rangle$	$\hat{\epsilon}_{unique}$	Sacrifice	$\Delta DP$
Enriched Source Detector Cut	Any other detector: isEsr No other detector: $( ((energy < 61.) \& (energy > 504.6) \& energy < 25.2) \& (energy > 587.8 \& energy < 65.2) \& (energy > 117.2 \& energy < 121.8) \& (energy > 170.6 \& energy > 1175.6) \& (energy > 330.2 \& energy < 1337.) \& (energy > 1483.) \& (energy > 1395.6) \& isEsr ) \& ( (energy < 44.8) \& (energy > 1765.8) \& sumE > 1472.) \& !isEsr )$ Not: $(sumE > 2042.8)$	M1: 21.5 % M2: 40.5 %	$23.3^{+2.7}_{-2.5}\%$ $63.8^{+6.0}_{-6.5}\%$	0.5 % 0.9 %	$1.1^{+0.9}_{-0.5}\%$ $6.9^{+4.1}_{-2.6}\%$	1.2 % 2.7 %	1.2 % 2.7 %
Coincident Energy Cut		M1: 26.2 % M2: 24.8 %	$28.9^{+2.9}_{-2.7}\%$ $29.3^{+6.3}_{-5.6}\%$	0.7 % 0.5 %	$1.5^{+0.9}_{-0.6}\%$ $6.9^{+4.1}_{-2.6}\%$	3.9 % 2.7 %	9 %
Sum Energy Cut		M1: 97.1 % M2: 97.6 %	$94.7^{+1.2}_{-1.5}\%$ $84.5^{+4.2}_{-5.3}\%$	54.1 % 40.6 %	$51.5 \pm 3.1\%$ $24.1^{+6.0}_{-5.2}\%$	12.8 % 16.4 %	261 %
Combined Cuts		M1: 98.3 % M2: 99.1 %	$97.7^{+1.1}_{-1.1}\%$ $98.3^{+2.7}_{-2.7}\%$	—	—	25.7 % 35.8 %	317 %

TABLE XIX Table of cut descriptions and efficiencies for simulated backgrounds and measured data for the 559 and 563 keV peaks.

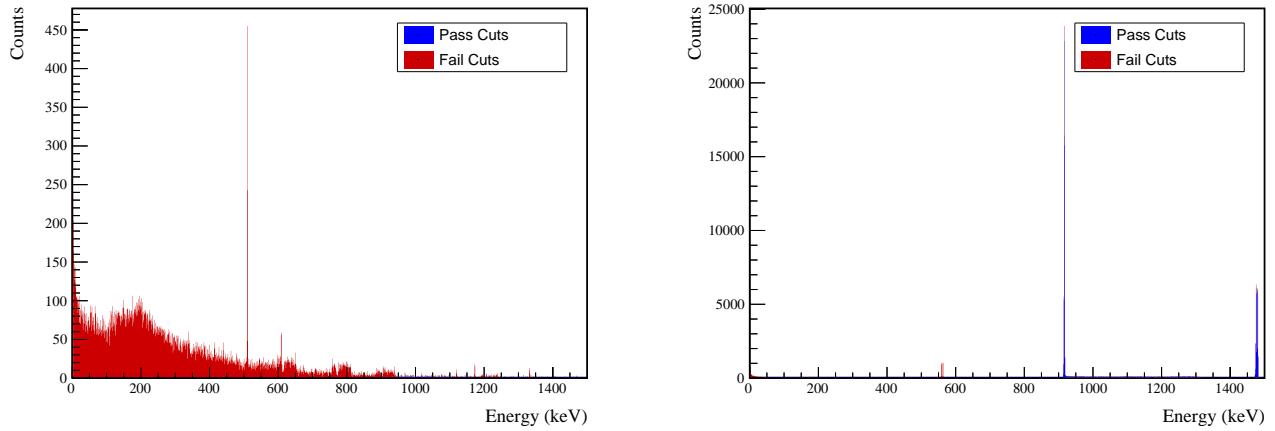


FIG. 72 Effect of 559 and 563 keV peaks cuts on coincident energy spectra in BG (left) and ES (right) simulations.

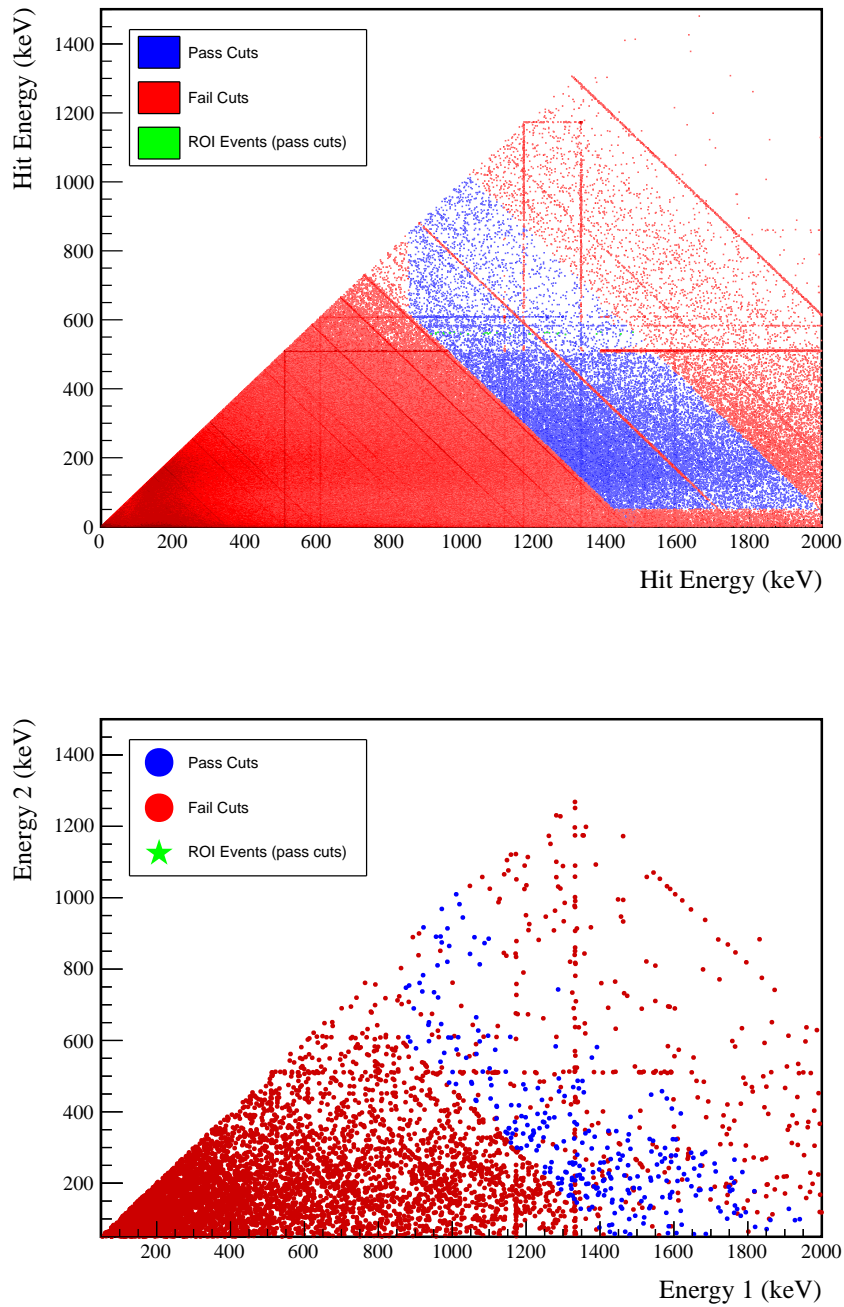
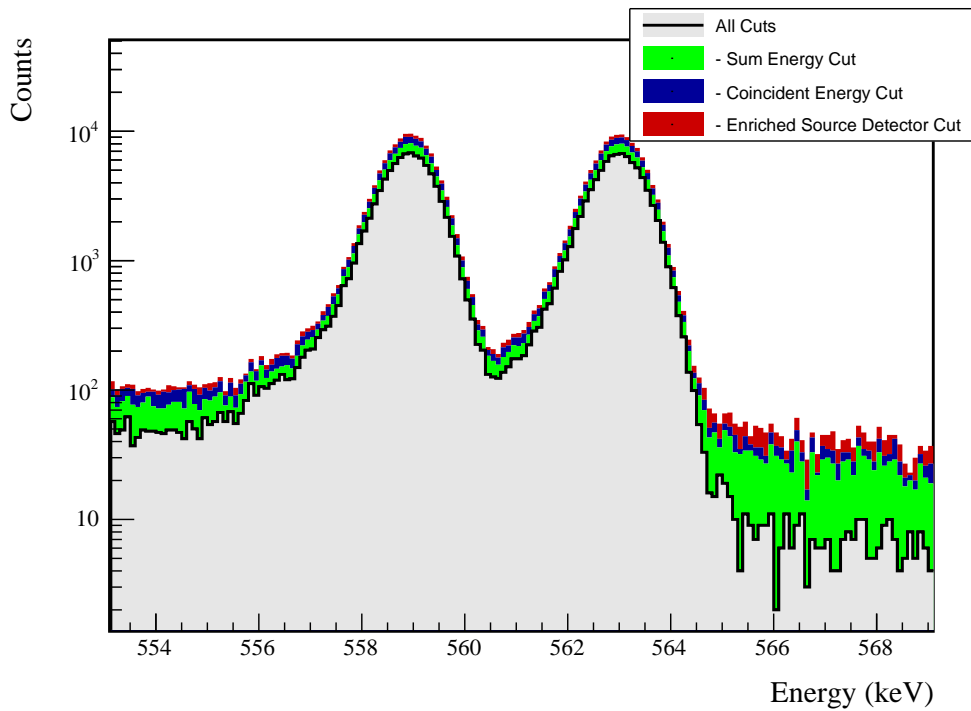


FIG. 73 Simulated (left) and measured (right) multiplicity 2 energy spectrum with sum and coincident energy cuts included for the 559 and 563 keV peaks.

FIG. 74 Effect of all cuts applied sequentially on ROI for 559 and 563 keV peaks of  $0\nu\beta\beta$  to  $0_1^+$ 

Source	Module 1 efficiency	Module 2 efficiency
Multi-Detector with Full Energy $\gamma$	$5.6 \pm 0.2\%$	$3.0 \pm 0.5\%$
Region of Interest	$89.8 \pm 1.3\%$	$89.8 \pm 1.3\%$
Dead Layer	$69.7 \pm 5.2\%$	$58.2 \pm 7.3\%$
Detector Dead Times	$98.4 \pm 0.8\%$	$98.6 \pm 0.6\%$
Enriched Source Detector Cut	$97.1 \pm <0.1\%$	$91.2 \pm <0.1\%$
Coincident Energy Cut	$89.4 \pm 0.3\%$	$87.8 \pm 0.3\%$
Sum Energy Cut	$79.7 \pm 0.3\%$	$70.3 \pm 0.3\%$
Final Efficiency	$3.00 \pm 0.25\%$	$1.27 \pm 0.26\%$

FIG. 75 Table of detection efficiencies for the 559 and 563 keV peaks.

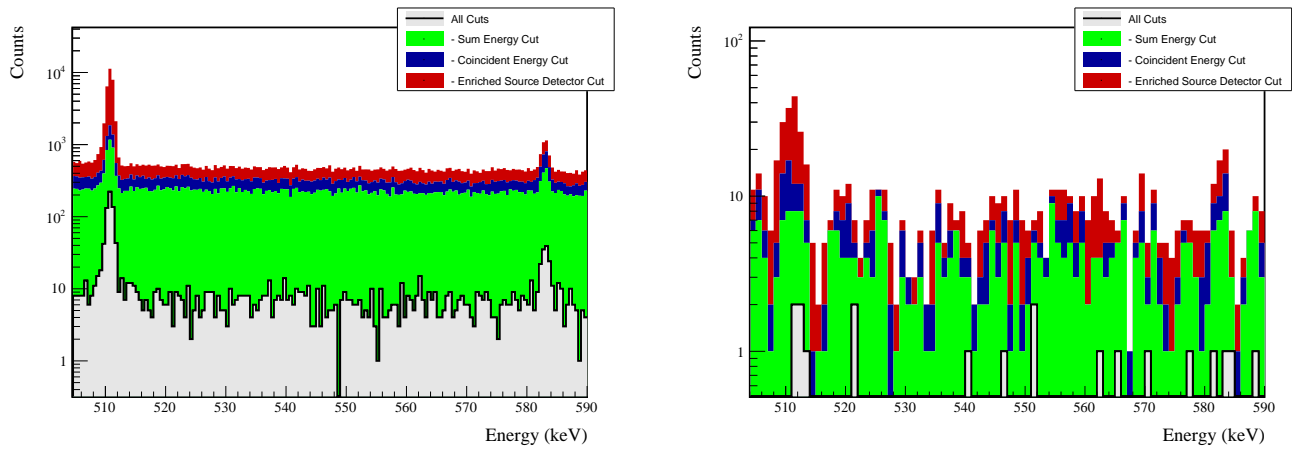
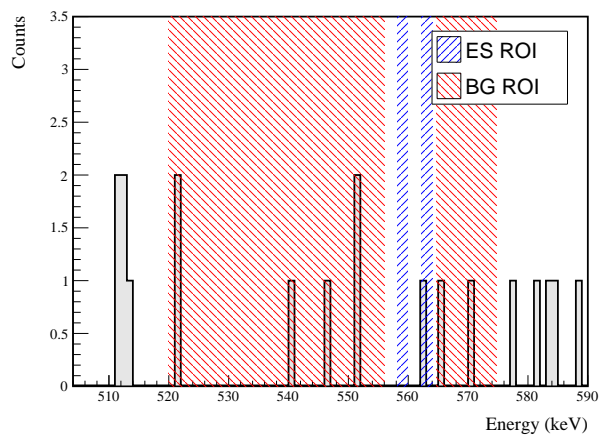


FIG. 76 Effect of all cuts applied to sequentially simulated (left) and measured (right) background data.

FIG. 77 All events after cuts in background (red) and signal (blue) ROIs for 559 and 563 keV peaks of  $0\nu\beta\beta$  to  $0_1^+$

<sup>714</sup> **Appendix F:  $0\nu\beta\beta$  to  $2_1^+$**

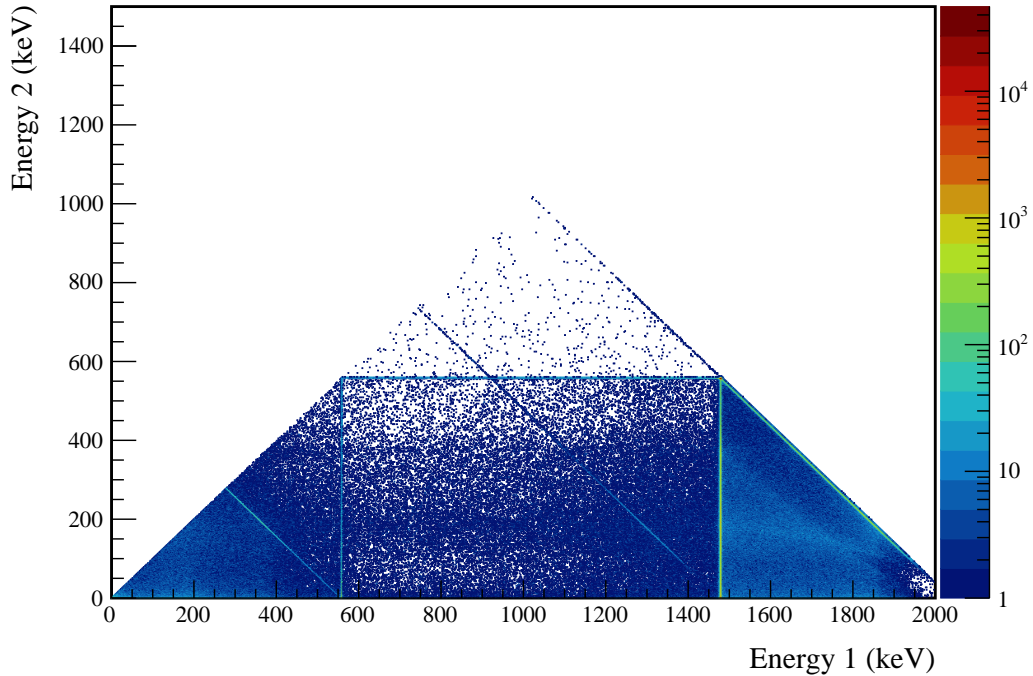


FIG. 78 Simulated multiplicity 2 energy spectrum of the  $0\nu\beta\beta$  to  $2_1^+$  decay mode

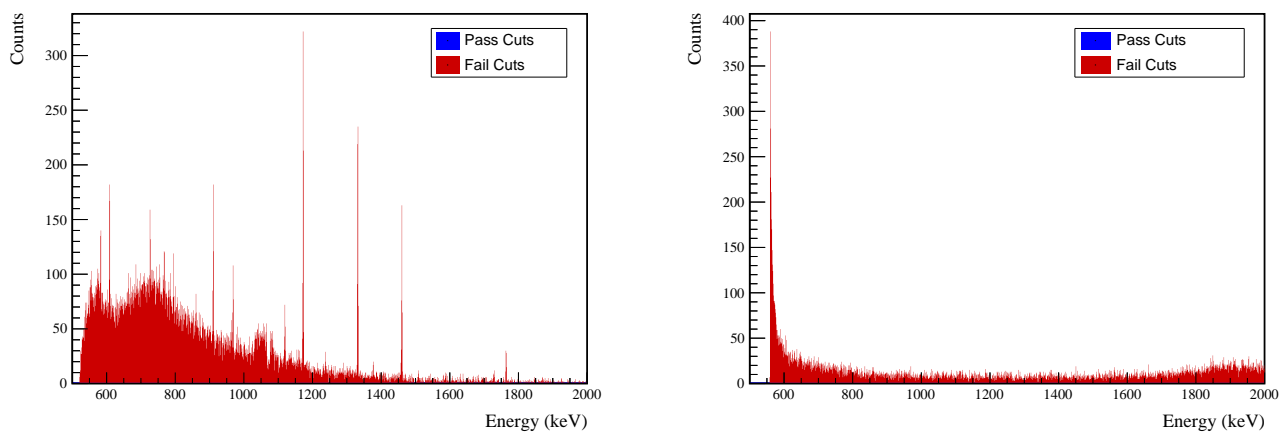


FIG. 79 Effect of 559 keV peak cuts on sum energy spectra in BG (left) and ES (right) simulations.



TABLE XX Table of energy estimation uncertainties for the 559 keV peak.

DS	$E_{peak}$ (keV)	$\sigma_{drift}$ (keV)	$\sigma_{fit}$ (keV)	$\sigma$ (keV)	$f_{t,fit}$	$\tau_{f,fit}$ (keV)	$\delta_{\mu,NL}$ (keV)	$\delta_{\mu,drift}$ (keV)	$\delta_{\mu,atalk}$ (keV)	$\delta_{\mu,peak}$ (keV)	$\delta_u$ (keV)	FWHM (keV)	$\delta_{fwhm,fit}$ (keV)	$\delta_{fwhm,drift}$ (keV)	$\delta_{fwhm,atalk}$ (keV)	$\delta_{FWHM}$ (keV)	$\delta_\alpha$	$E_{ROI,1}$ (keV)	$E_{ROI,2}$ (keV)	$\epsilon_{ROI}$	$\sigma_{e_{ROI}}$	
DS1	559.101	0.460	0.063	0.464	0.230	0.515	0.001	0.104	0.002	0.012	0.005	0.105	1.152	0.001	0.039	0.011	0.040	0.035	558.052	559.959	0.915	0.011
DS2	559.101	0.461	0.055	0.464	0.249	0.515	0.002	0.067	0.004	0.012	0.005	0.068	1.158	0.001	0.107	0.011	0.108	0.093	558.035	559.957	0.917	0.023
DS3	559.101	0.470	0.066	0.474	0.224	0.505	0.001	0.026	0.024	0.012	0.005	0.038	1.174	0.001	0.073	0.011	0.074	0.063	558.039	559.977	0.921	0.016
DS4	559.101	0.455	0.077	0.461	0.108	0.445	0.002	0.076	0.010	0.012	0.005	0.078	1.111	0.001	0.106	0.011	0.107	0.096	558.161	559.966	0.929	0.024
DS5a	559.101	0.560	0.085	0.567	0.106	0.885	0.002	0.079	0.005	0.012	0.005	0.080	1.367	0.002	0.055	0.011	0.056	0.041	557.942	560.158	0.918	0.011
DS5b	559.101	0.469	0.074	0.475	0.158	0.491	0.001	0.020	0.011	0.012	0.005	0.026	1.157	0.001	0.125	0.011	0.125	0.108	558.094	559.986	0.927	0.027
DS5c	559.101	0.460	0.085	0.468	0.174	0.489	0.001	0.037	0.030	0.012	0.005	0.050	1.145	0.001	0.162	0.011	0.162	0.142	558.095	559.972	0.924	0.035
DS6a	559.101	0.456	0.044	0.458	0.191	0.463	0.001	0.069	0.025	0.012	0.005	0.075	1.123	0.000	0.041	0.011	0.042	0.038	558.106	559.951	0.923	0.010



Cut Name	Cut Description	$\langle \epsilon_{total} \rangle$	$\hat{\epsilon}_{total}$	$\langle \epsilon_{unique} \rangle$	$\hat{\epsilon}_{unique}$	Sacrifice	$\Delta DP$
Enriched Source Detector Cut	Any other detector: isEar	M1: 21.5 % M2: 40.6 %	23.0 <sup>+2.7</sup> / <sub>-2.5</sub> % 63.8 <sup>+6.0</sup> / <sub>-6.5</sub> %	0.0 % 0.0 %	0.0 <sup>+0.4</sup> / <sub>-0.9</sub> % 0.0 <sup>+1.7</sup> / <sub>-0.0</sub> %	1.9 % 4.0 %	-1 %
Multiplicity 2 Cut $n=2$		M1: 15.0 % M2: 11.5 %	16.6 <sup>+2.4</sup> / <sub>-2.2</sub> % 17.2 <sup>+2.5</sup> / <sub>-4.4</sub> %	0.0 % 0.0 %	0.0 <sup>+0.4</sup> / <sub>-0.9</sub> % 0.0 <sup>+1.7</sup> / <sub>-0.9</sub> %	0.0 % 0.0 %	0 %
Coincident Energy Cut	Any other detector: energy>1472.4 && energy<1483.3	M1: 100.0 % M2: 100.0 %	100.0 <sup>+0.0</sup> / <sub>-0.4</sub> % 100.0 <sup>+0.0</sup> / <sub>-1.7</sub> %	64.6 % 49.9 %	62.3 <sup>+3.0</sup> / <sub>-5.3</sub> % 25.9 <sup>+6.1</sup> / <sub>-5.3</sub> %	18.3 % 22.0 %	1046 %
Combined Cuts		M1: 100.0 % M2: 100.0 %	100.0 <sup>+0.0</sup> / <sub>-0.4</sub> % 100.0 <sup>+0.0</sup> / <sub>-1.7</sub> %	—	—	22.1 % 28.5 %	1273 %

TABLE XXI Table of cut descriptions and efficiencies for simulated backgrounds and measured data for the 559 keV peak.

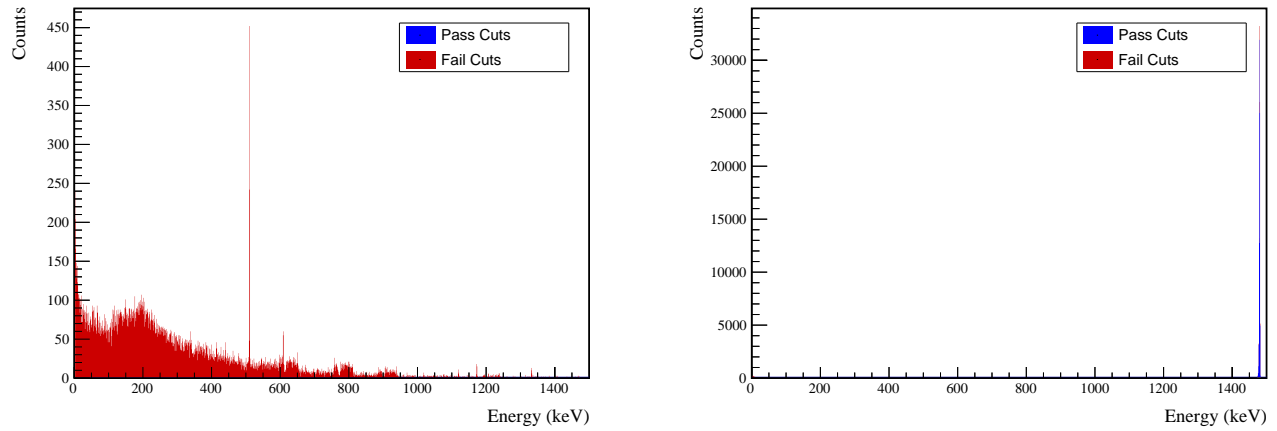


FIG. 80 Effect of 559 keV peak cuts on coincident energy spectra in BG (left) and ES (right) simulations.

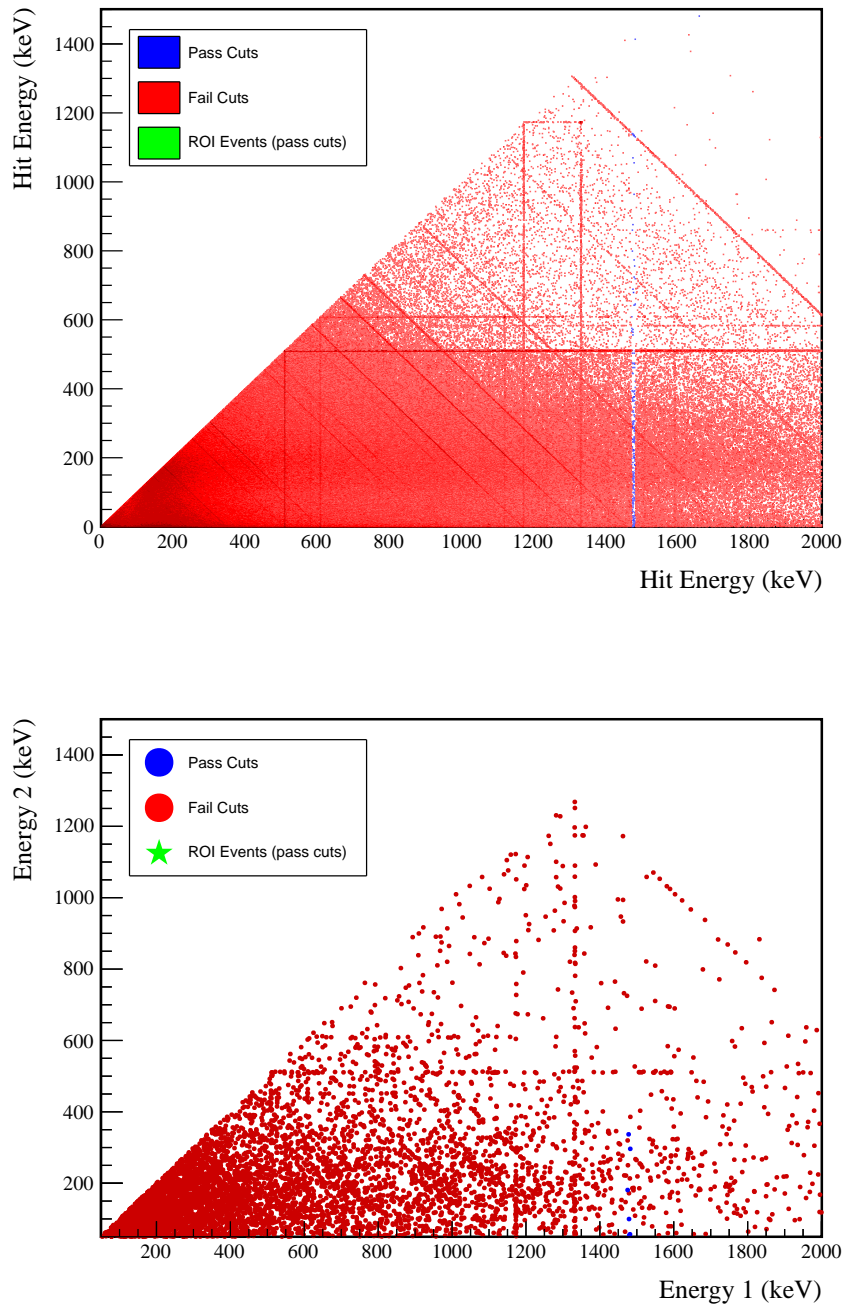
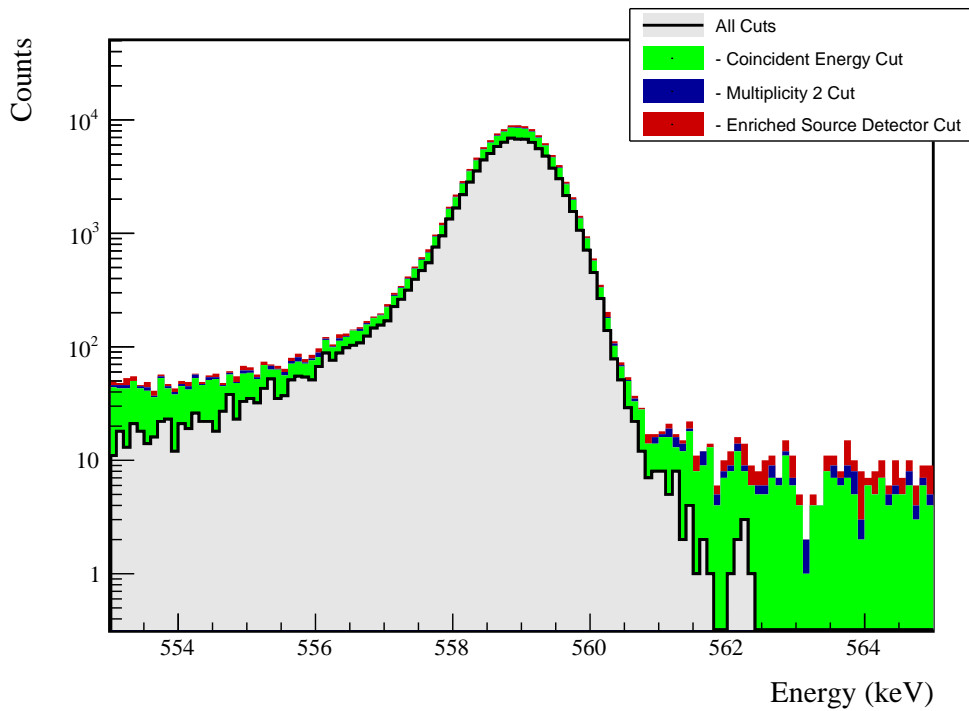


FIG. 81 Simulated (left) and measured (right) multiplicity 2 energy spectrum with sum and coincident energy cuts included for the 559 keV peak.

FIG. 82 Effect of all cuts applied sequentially on ROI for 559 keV peak of  $0\nu\beta\beta$  to  $2_1^+$ 

Source	Module 1 efficiency	Module 2 efficiency
Multi-Detector with Full Energy $\gamma$	$2.9 \pm 0.2\%$	$1.5 \pm 0.5\%$
Region of Interest	$92.2 \pm 1.5\%$	$92.2 \pm 1.5\%$
Dead Layer	$68.3 \pm 5.4\%$	$56.6 \pm 7.6\%$
Detector Dead Times	$98.4 \pm 0.8\%$	$98.6 \pm 0.7\%$
Enriched Source Detector Cut	$97.6 \pm < 0.1\%$	$94.2 \pm < 0.1\%$
Multiplicity 2 Cut	$98.7 \pm < 0.1\%$	$99.2 \pm < 0.1\%$
Coincident Energy Cut	$79.8 \pm 0.3\%$	$75.4 \pm 0.3\%$
Final Efficiency	$1.61 \pm 0.17\%$	$0.68 \pm 0.23\%$

FIG. 83 Table of detection efficiencies for the 559 keV peak.

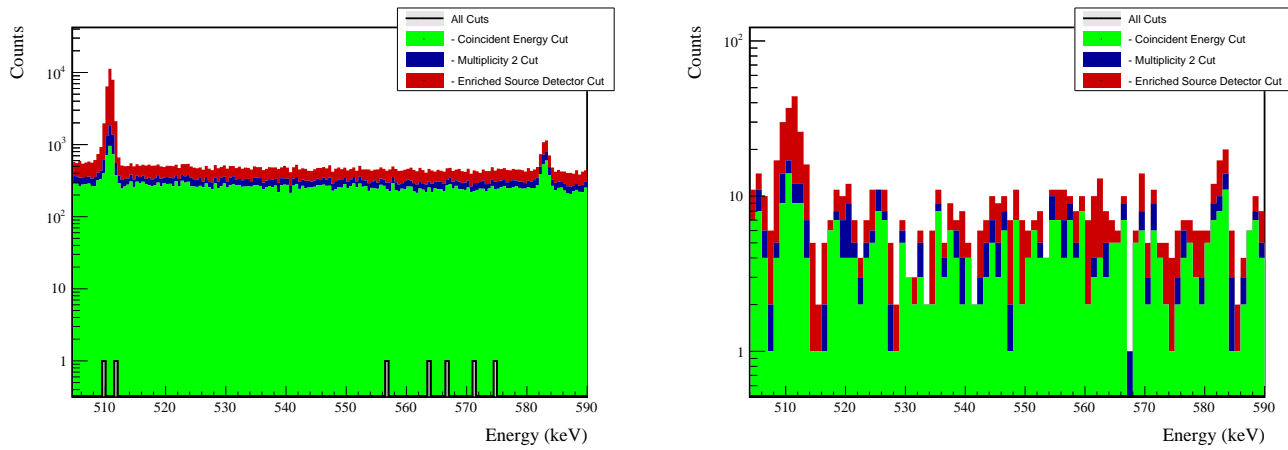
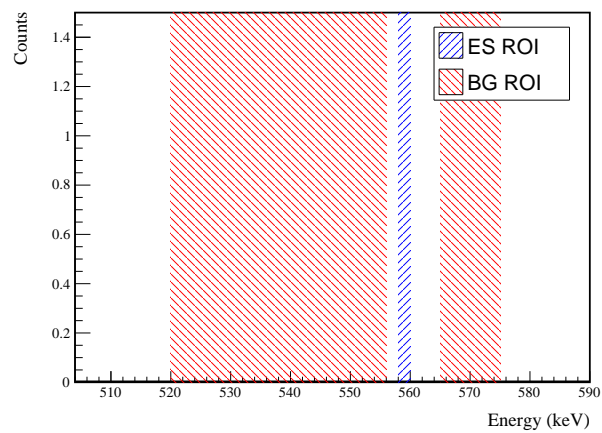


FIG. 84 Effect of all cuts applied to sequentially simulated (left) and measured (right) background data.

FIG. 85 All events after cuts in background (red) and signal (blue) ROIs for 559 keV peak of  $0\nu\beta\beta$  to  $2_1^+$

<sup>715</sup> **Appendix G:  $0\nu\beta\beta$  to  $2_2^+$**

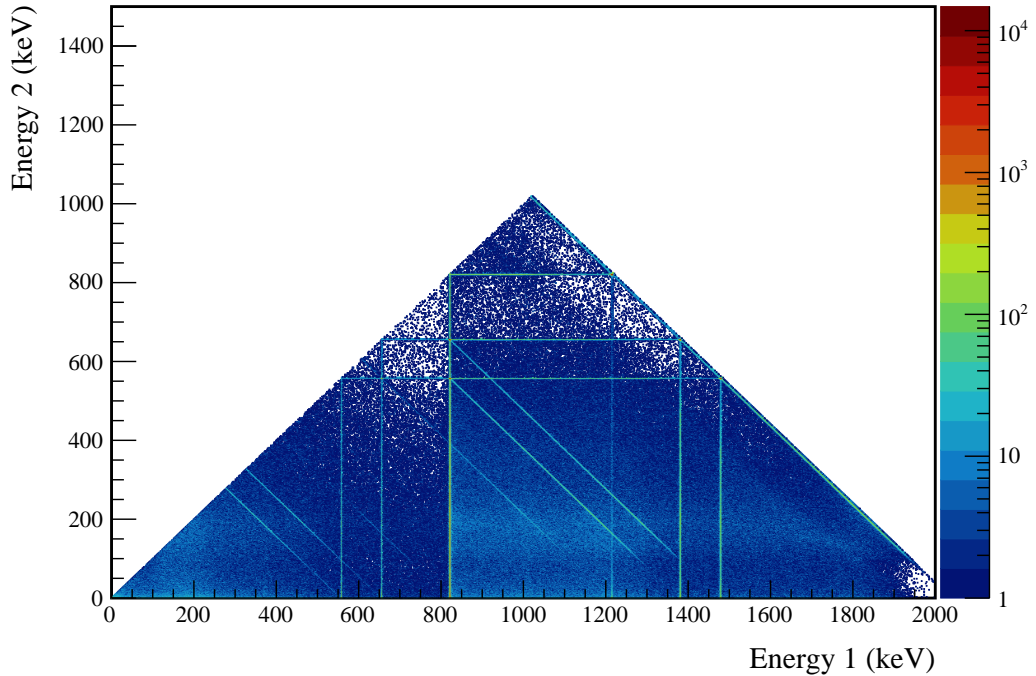


FIG. 86 Simulated multiplicity 2 energy spectrum of the  $0\nu\beta\beta$  to  $2_2^+$  decay mode

<sup>716</sup> **1. 559 keV peak**

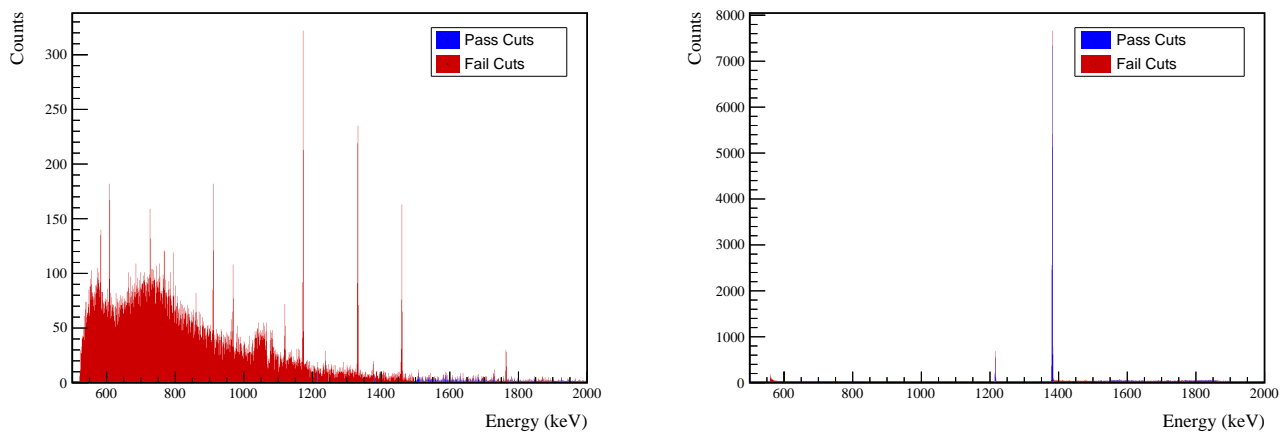


FIG. 87 Effect of 559 keV peak cuts on sum energy spectra in BG (left) and ES (right) simulations.



TABLE XXII Table of energy estimation uncertainties for the 559 keV peak.

DS	$E_{peak}$ (keV)	$\sigma_{drift}$ (keV)	$\sigma_{fit}$ (keV)	$\sigma$ (keV)	$f_{t,fit}$	$\tau_{f,fit}$ (keV)	$\delta_{\mu,fit}$ (keV)	$\delta_{\mu,NL}$ (keV)	$\delta_{\mu,drift}$ (keV)	$\delta_{\mu,xtalk}$ (keV)	$\delta_{\mu,peak}$ (keV)	$\delta_u$ (keV)	FWHM	$\delta_{fwhm,fit}$ (keV)	$\delta_{fwhm,drift}$ (keV)	$\delta_{fwhm,xtalk}$ (keV)	$\delta_{fwhm,HM}$ (keV)	$\delta_\alpha$	$E_{ROI,1}$ (keV)	$E_{ROI,2}$ (keV)	$\epsilon_{ROI}$	$\sigma_{\epsilon_{ROI}}$
DS1	559.101	0.460	0.063	0.464	0.230	0.515	0.001	0.104	0.002	0.012	0.005	0.105	1.152	0.001	0.039	0.011	0.040	0.035	558.152	559.883	0.887	0.014
DS2	559.101	0.461	0.055	0.464	0.249	0.515	0.002	0.067	0.004	0.012	0.005	0.068	1.158	0.001	0.107	0.011	0.108	0.093	558.137	559.882	0.890	0.028
DS3	559.101	0.470	0.066	0.474	0.224	0.505	0.001	0.026	0.024	0.012	0.005	0.038	1.174	0.001	0.073	0.011	0.074	0.063	558.140	559.900	0.894	0.019
DS4	559.101	0.455	0.077	0.461	0.108	0.445	0.002	0.076	0.010	0.012	0.005	0.078	1.111	0.001	0.106	0.011	0.107	0.096	558.243	559.892	0.903	0.030
DS5a	559.101	0.560	0.085	0.567	0.106	0.885	0.002	0.079	0.005	0.012	0.005	0.080	1.367	0.002	0.055	0.011	0.056	0.041	558.049	560.067	0.891	0.013
DS5b	559.101	0.469	0.074	0.475	0.158	0.491	0.001	0.020	0.011	0.012	0.005	0.026	1.157	0.001	0.125	0.011	0.125	0.108	558.185	559.909	0.901	0.033
DS5c	559.101	0.460	0.085	0.468	0.174	0.489	0.001	0.037	0.030	0.012	0.005	0.050	1.145	0.001	0.162	0.011	0.162	0.142	558.187	559.896	0.898	0.042
DS6a	559.101	0.456	0.044	0.458	0.191	0.463	0.001	0.069	0.025	0.012	0.005	0.075	1.123	0.000	0.041	0.011	0.042	0.038	558.198	559.877	0.896	0.012



Cut Name	Cut Description	$\langle \epsilon_{total} \rangle$	$\hat{\epsilon}_{total}$	$\langle \epsilon_{unique} \rangle$	$\hat{\epsilon}_{unique}$	Sacrifice	$\Delta DP$
Enriched Source Detector Cut	Any other detector: <code>isEsr</code>	M1: 21.5 % M2: 40.6 %	23.0 <sup>+2.7</sup> <sub>-2.5</sub> % 63.8 <sup>+6.0</sup> <sub>-6.5</sub> %	0.5 % 0.9 %	0.8 <sup>+0.7</sup> <sub>-0.4</sub> % 6.9 <sup>+4.1</sup> <sub>-2.6</sub> %	1.3 % 3.0 %	9%
Coincident Energy Cut	No other detector: <code>((energy&lt;63)    (energy&gt;591.4 &amp;&amp; energy&lt;1170.6 &amp;&amp; energy&lt;1175.6)    (energy&gt;1205. &amp;&amp; energy&lt;1208.)    (energy&gt;1331.    (energy&lt;1331.6)    (energy&gt;1482.6)) &amp;&amp; !isEsr)    (    (energy&lt;1337.)    (energy&gt;1482.6)) &amp;&amp; !isEsr)    (    (energy&lt;44.8)    (energy&gt;502.2 &amp;&amp; energy&lt;515.2)    (energy&gt;375.4) &amp;&amp; !isEsr)</code>	M1: 20.6 % M2: 21.3 %	21.9 <sup>+2.6</sup> <sub>-2.4</sub> % 25.9 <sup>+6.1</sup> <sub>-5.3</sub> %	0.4 % 0.3 %	1.1 <sup>+0.9</sup> <sub>-0.5</sub> % 5.2 <sup>+3.7</sup> <sub>-2.2</sub> %	2.3 % 1.4 %	5%
Sum Energy Cut	Not: <code>(sumE&gt;1383.6 &amp;&amp; sumE&lt;1496.6)    (sumE&gt;1216.2 &amp;&amp; sumE&lt;1378.)    (sumE&gt;2041.6)</code>	M1: 97.2 % M2: 97.7 %	94.7 <sup>+1.2</sup> <sub>-1.5</sub> % 86.2 <sup>+3.9</sup> <sub>-5.1</sub> %	60.3 % 45.3 %	58.9 <sup>+3.1</sup> <sub>-0.9</sub> % 27.6 <sup>+6.2</sup> <sub>-5.5</sub> %	20.2 % 22.8 %	208%
Combined Cuts		M1: 98.1 % M2: 99.0 %	97.0 <sup>+0.9</sup> <sub>-1.2</sub> % 98.3 <sup>+1.1</sup> <sub>-2.7</sub> %	—	—	30.5 % 39.9 %	244%

TABLE XXIII Table of cut descriptions and efficiencies for simulated backgrounds and measured data for the 559 keV peak.

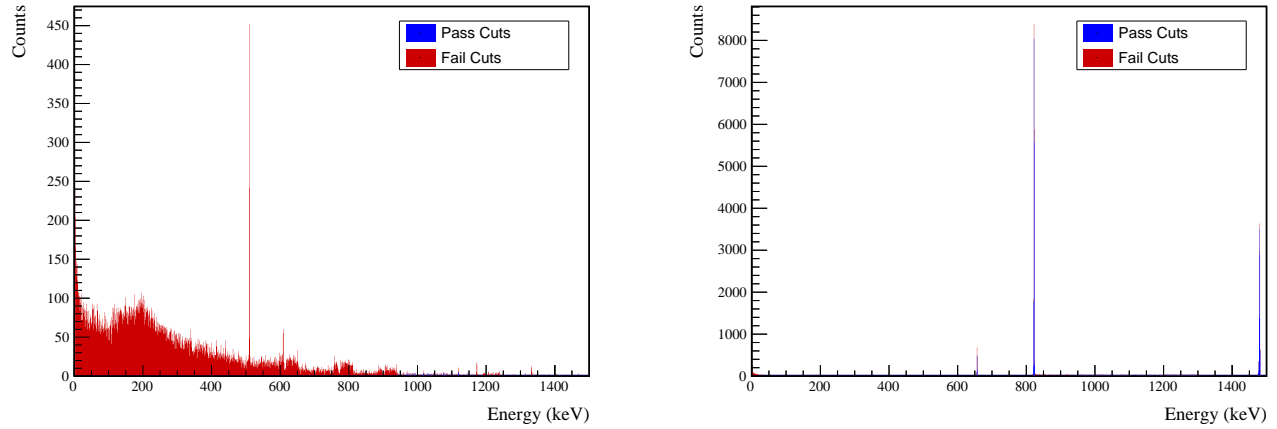


FIG. 88 Effect of 559 keV peak cuts on coincident energy spectra in BG (left) and ES (right) simulations.

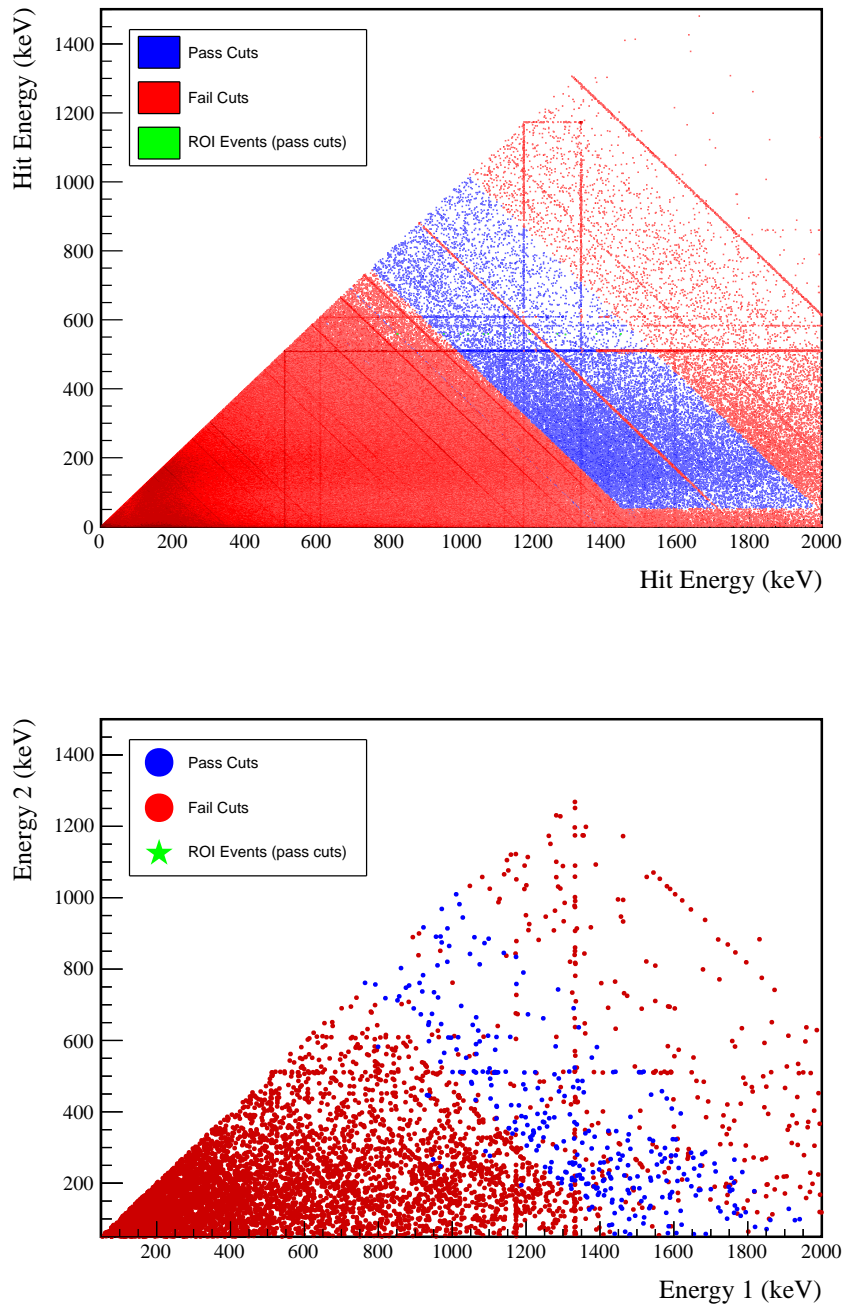
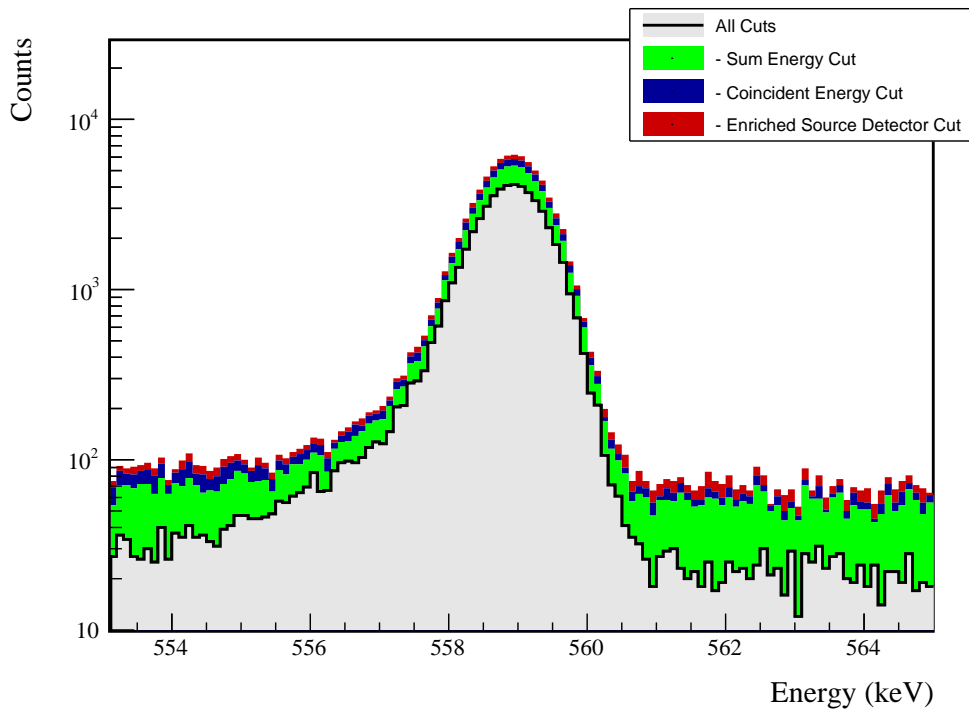


FIG. 89 Simulated (left) and measured (right) multiplicity 2 energy spectrum with sum and coincident energy cuts included for the 559 keV peak.

FIG. 90 Effect of all cuts applied sequentially on ROI for 559 keV peak of  $0\nu\beta\beta$  to  $2_2^+$ 

Source	Module 1 efficiency	Module 2 efficiency
Multi-Detector with Full Energy $\gamma$	$1.9 \pm 0.2\%$	$1.0 \pm 0.5\%$
Region of Interest	$89.5 \pm 1.8\%$	$89.5 \pm 1.8\%$
Dead Layer	$69.1 \pm 5.3\%$	$57.9 \pm 7.4\%$
Detector Dead Times	$98.4 \pm 0.8\%$	$98.6 \pm 0.7\%$
Enriched Source Detector Cut	$97.0 \pm <0.1\%$	$90.7 \pm <0.1\%$
Coincident Energy Cut	$92.3 \pm 0.3\%$	$90.6 \pm 0.3\%$
Sum Energy Cut	$73.4 \pm 0.3\%$	$65.1 \pm 0.3\%$
Final Efficiency	$0.94 \pm 0.13\%$	$0.40 \pm 0.19\%$

FIG. 91 Table of detection efficiencies for the 559 keV peak.

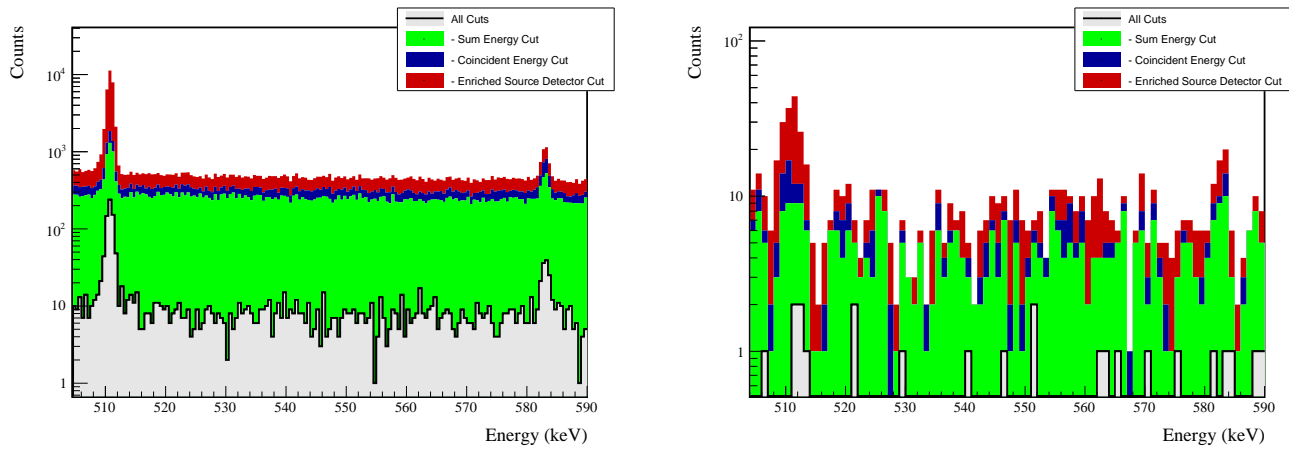
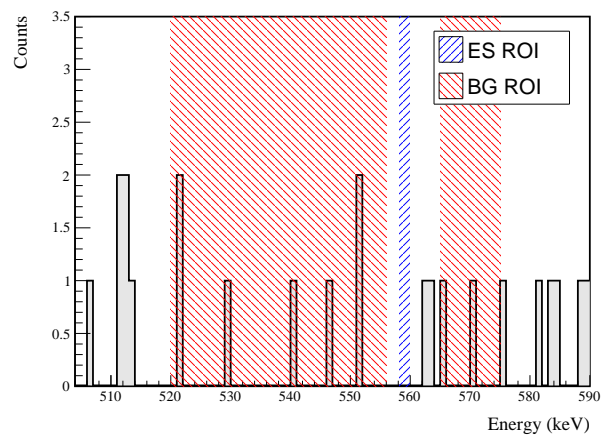


FIG. 92 Effect of all cuts applied to sequentially simulated (left) and measured (right) background data.

FIG. 93 All events after cuts in background (red) and signal (blue) ROIs for 559 keV peak of  $0\nu\beta\beta$  to  $2_2^+$



## 717 2. 657 keV peak

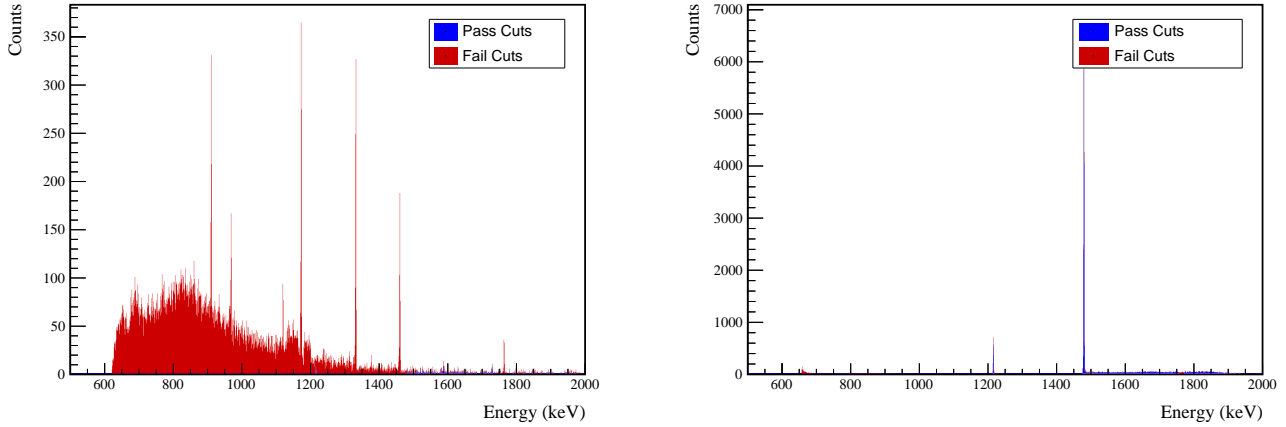


FIG. 94 Effect of 657 keV peak cuts on sum energy spectra in BG (left) and ES (right) simulations.

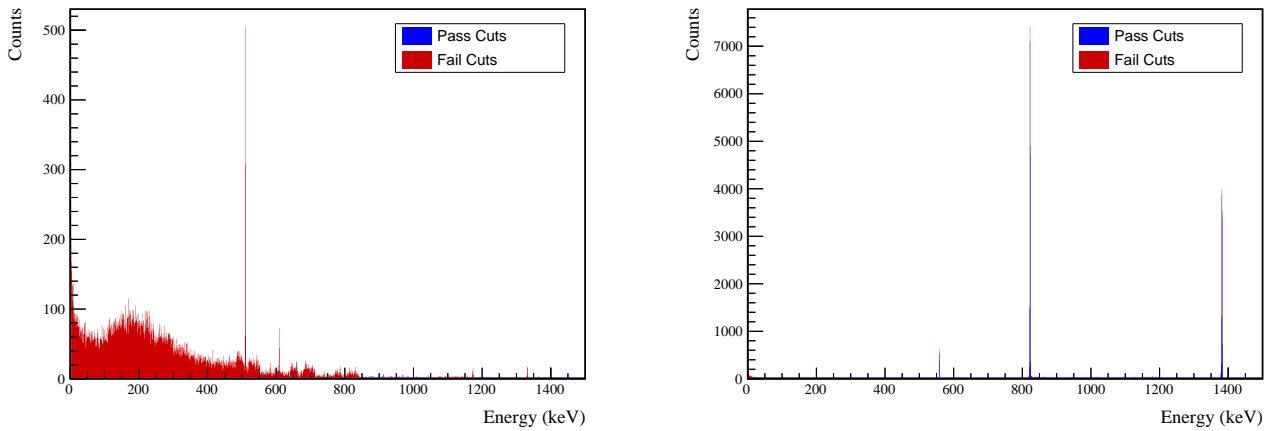


FIG. 95 Effect of 657 keV peak cuts on coincident energy spectra in BG (left) and ES (right) simulations.



TABLE XXIV Table of energy estimation uncertainties for the 657 keV peak.

DS	$E_{peak}$ (keV)	$\sigma_{drift}$ (keV)	$\sigma_{fit}$ (keV)	$\sigma$ (keV)	$f_{t,fit}$	$\tau_{f,fit}$ (keV)	$\delta_{\mu,fit}$ (keV)	$\delta_{\mu,NL}$ (keV)	$\delta_{\mu,drift}$ (keV)	$\delta_{\mu,xtalk}$ (keV)	$\delta_u$ (keV)	FWHM (keV)	$\delta_{fwhm,fit}$ (keV)	$\delta_{fwhm,drift}$ (keV)	$\delta_{fwhm,xtalk}$ (keV)	$\delta_{FWHM}$ (keV)	$\delta_\alpha$	$E_{ROI,1}$ (keV)	$E_{ROI,2}$ (keV)	$\epsilon_{ROI}$	$\sigma_{e_{ROI}}$	
DS1	657.041	0.500	0.074	0.505	0.230	0.579	0.002	0.104	0.003	0.012	0.005	0.105	1.256	0.001	0.039	0.011	0.040	0.032	656.029	657.875	0.880	0.013
DS2	657.041	0.502	0.064	0.506	0.249	0.580	0.002	0.067	0.005	0.012	0.005	0.068	1.263	0.001	0.107	0.011	0.108	0.085	656.013	657.873	0.881	0.027
DS3	657.041	0.510	0.078	0.516	0.224	0.568	0.002	0.026	0.026	0.012	0.005	0.040	1.278	0.001	0.073	0.011	0.074	0.058	656.017	657.892	0.886	0.018
DS4	657.041	0.493	0.090	0.501	0.108	0.490	0.002	0.076	0.076	0.012	0.005	0.078	1.207	0.001	0.106	0.011	0.107	0.088	656.128	657.882	0.897	0.028
DS5a	657.041	0.606	0.100	0.614	0.106	0.924	0.002	0.079	0.006	0.012	0.005	0.080	1.481	0.002	0.055	0.011	0.056	0.038	655.925	658.065	0.885	0.013
DS5b	657.041	0.509	0.087	0.517	0.158	0.562	0.001	0.020	0.013	0.012	0.005	0.027	1.259	0.001	0.125	0.011	0.125	0.100	656.066	657.902	0.892	0.031
DS5c	657.041	0.500	0.100	0.510	0.174	0.555	0.002	0.037	0.035	0.012	0.005	0.053	1.247	0.001	0.162	0.011	0.162	0.130	656.066	657.888	0.890	0.041
DS6a	657.041	0.495	0.051	0.497	0.191	0.524	0.001	0.069	0.030	0.012	0.005	0.076	1.221	0.001	0.041	0.011	0.042	0.035	656.079	657.866	0.888	0.012



Cut Name	Cut Description	$\langle \epsilon_{total} \rangle$	$\hat{\epsilon}_{total}$	$\langle \epsilon_{unique} \rangle$	$\hat{\epsilon}_{unique}$	Sacrifice	$\Delta DP$
Enriched Source Detector Cut	Any other detector: isEsr No other detector: $((energy < 41.2)    (energy > 425.2 \&& energy < 529.4)    (energy > 562.4 \&& energy < 611.4)    (energy > 775.6 \&& energy < 817.8)    (energy > 159.6 \&& energy < 1175.1)    (energy > 159.6 \&& energy < 133.2)    (energy > 308.8 \&& energy > 133.2)    (energy > 384.8) \&& isEsr )    ((energy < 40.6)    (energy > 489.6 \&& energy < 521.1)    (energy > 1248.1) \&& :isEsr )$	M1: 22.2 % M2: 41.6 %	$23.4^{+2.9}_{-2.7}\%$ $59.7^{+5.6}_{-5.9}\%$	0.5 % 1.1 %	$2.2^{+1.2}_{-0.8}\%$ $2.8^{+2.7}_{-1.4}\%$	1.3 % 3.3 %	12 %
Coincident Energy Cut	$((energy > 1214.8)    (sumE < 1216.8 \&& sumE < 1474.4)    (sumE > 1757.6 \&& sumE < 1771.6)    (sumE > 2042.6))$	M1: 97.0 % M2: 97.1 % M1: 98.4 % M2: 99.0 %	$90.5^{+1.8}_{-2.1}\%$ $93.1^{+2.4}_{-3.6}\%$ $95.7^{+1.2}_{-1.5}\%$ $98.6^{+0.9}_{-2.2}\%$	$51.9 \pm 3.3\%$ $40.5 \pm 5.6\%$ — —	$27.8^{+5.6}_{-4.9}\%$ $24.8 \pm 4.9\%$ — —	12.3 % 15.3 % 24.8 % 28.1 %	232 %
Sum Energy Cut							
Combined Cuts							

TABLE XXV Table of cut descriptions and efficiencies for simulated backgrounds and measured data for the 657 keV peak.

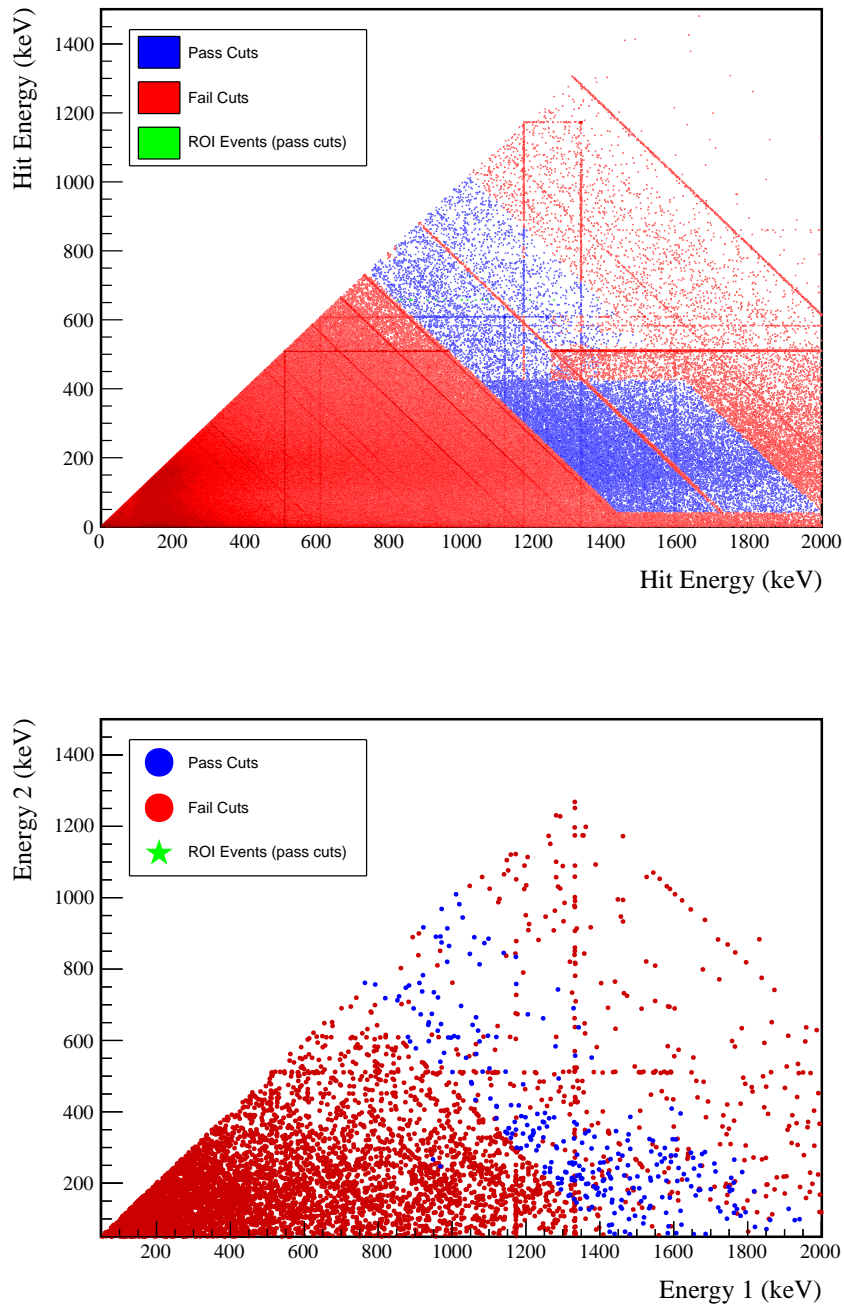
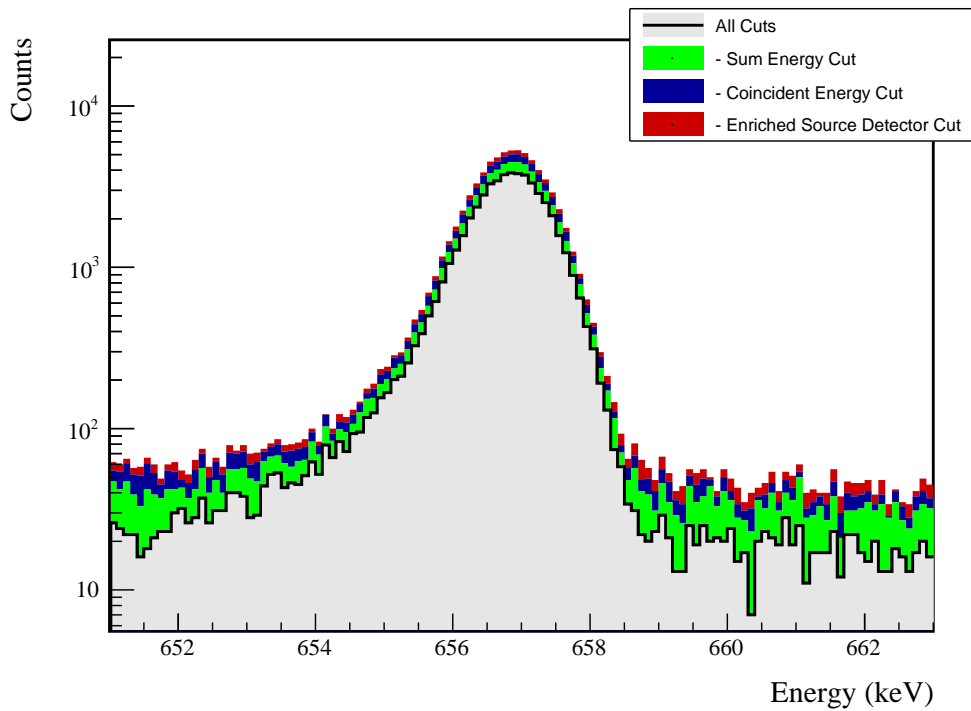


FIG. 96 Simulated (left) and measured (right) multiplicity 2 energy spectrum with sum and coincident energy cuts included for the 657 keV peak.

FIG. 97 Effect of all cuts applied sequentially on ROI for 657 keV peak of  $0\nu\beta\beta$  to  $2_2^+$ 

Source	Module 1 efficiency	Module 2 efficiency
Multi-Detector with Full Energy $\gamma$	$1.7 \pm 0.2\%$	$0.9 \pm 0.5\%$
Region of Interest Dead Layer	$88.7 \pm 1.7\%$	$88.7 \pm 1.7\%$
Detector Dead Times	$70.0 \pm 5.1\%$	$58.9 \pm 7.2\%$
Enriched Source Detector Cut	$97.0 \pm <0.1\%$	$90.5 \pm <0.1\%$
Coincident Energy Cut	$89.9 \pm 0.3\%$	$88.1 \pm 0.3\%$
Sum Energy Cut	$80.9 \pm 0.3\%$	$71.9 \pm 0.3\%$
Final Efficiency	$0.93 \pm 0.13\%$	$0.39 \pm 0.21\%$

FIG. 98 Table of detection efficiencies for the 657 keV peak.

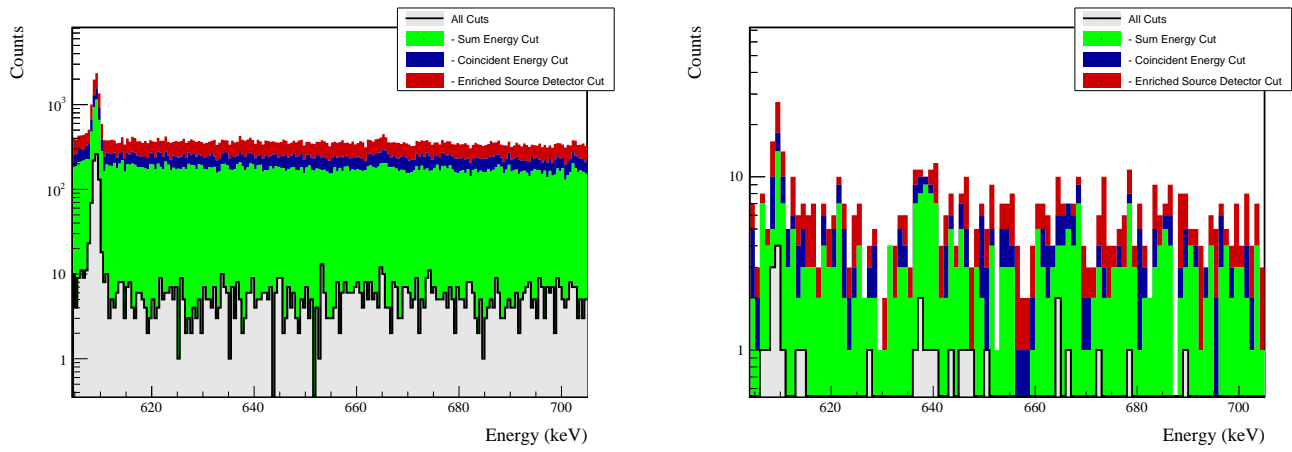
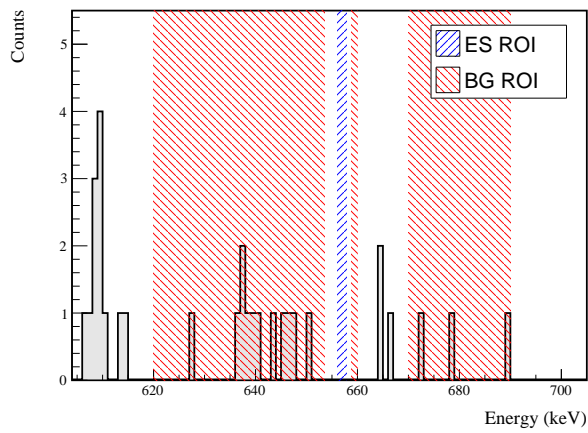


FIG. 99 Effect of all cuts applied to sequentially simulated (left) and measured (right) background data.

FIG. 100 All events after cuts in background (red) and signal (blue) ROIs for 657 keV peak of  $0\nu\beta\beta$  to  $2_2^+$



## 718 3. 1216 keV peak

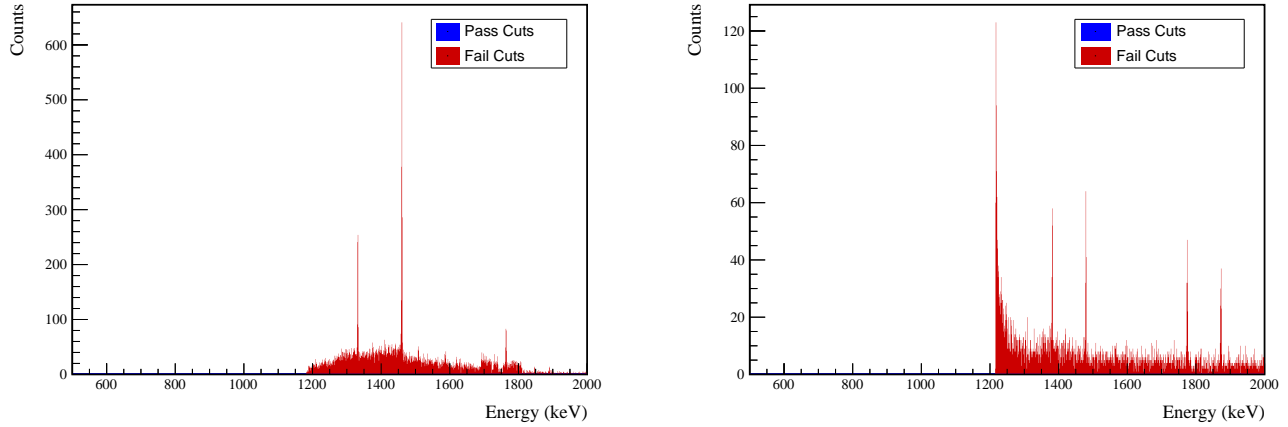


FIG. 101 Effect of 1216 keV peak cuts on sum energy spectra in BG (left) and ES (right) simulations.

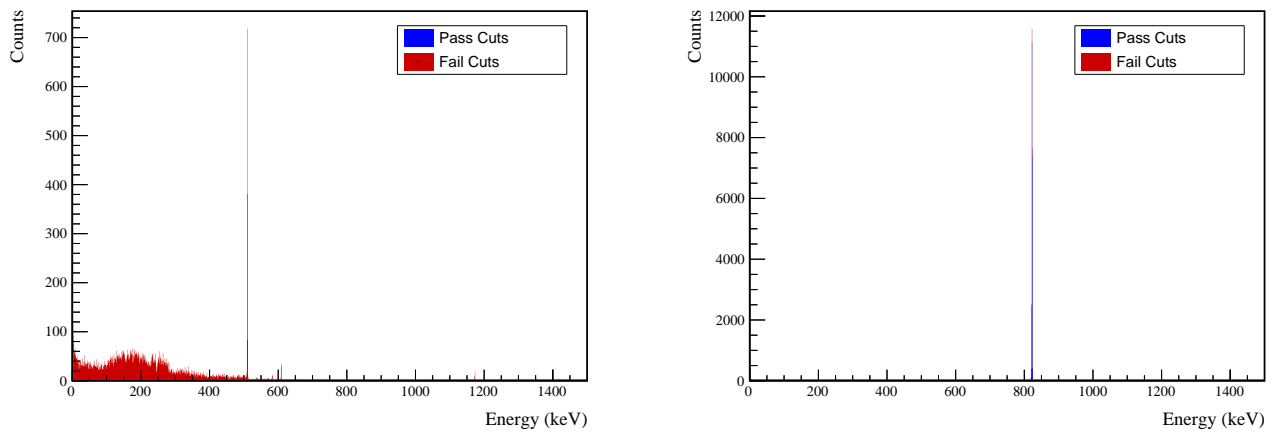


FIG. 102 Effect of 1216 keV peak cuts on coincident energy spectra in BG (left) and ES (right) simulations.



TABLE XXVI Table of energy estimation uncertainties for the 1216 keV peak.

DS	$E_{peak}$ (keV)	$\sigma_{fit}$ (keV)	$\sigma_{drift}$ (keV)	$\sigma$ (keV)	$f_{t,fit}$	$\tau_{fit}$ (keV)	$\delta_{\mu,NL}$ (keV)	$\delta_{\mu,drift}$ (keV)	$\delta_{\mu,xtalk}$ (keV)	$\delta_{\mu,peak}$ (keV)	$\delta_\mu$ (keV)	FWHM	$\delta_{fwhm,fit}$ (keV)	$\delta_{fwhm,drift}$ (keV)	$\delta_{fwhm,xtalk}$ (keV)	$\delta_{FWHM}$ (keV)	$\delta_\alpha$	$E_{ROI,1}$ (keV)	$E_{ROI,2}$ (keV)	$\epsilon_{ROI}$	$\sigma_{e_{ROI}}$	
DS1	1216.104	0.705	0.137	0.718	0.230	0.945	0.003	0.104	0.005	0.012	0.020	0.107	1.787	0.001	0.039	0.011	0.040	0.023	1214.426	1217.449	0.914	0.006
DS2	1216.104	0.710	0.119	0.720	0.249	0.951	0.003	0.067	0.008	0.012	0.020	0.072	1.803	0.001	0.107	0.011	0.108	0.060	1214.387	1217.449	0.914	0.014
DS3	1216.104	0.715	0.144	0.729	0.224	0.925	0.003	0.026	0.051	0.012	0.020	0.062	1.812	0.001	0.073	0.011	0.074	0.041	1214.416	1217.470	0.917	0.010
DS4	1216.104	0.697	0.167	0.717	0.108	0.746	0.003	0.076	0.022	0.012	0.020	0.083	1.726	0.001	0.106	0.011	0.107	0.062	1214.621	1217.461	0.932	0.015
DS5a	1216.104	0.838	0.185	0.859	0.106	1.316	0.004	0.079	0.012	0.012	0.020	0.083	2.070	0.002	0.055	0.011	0.056	0.027	1214.323	1217.722	0.921	0.007
DS5b	1216.104	0.716	0.161	0.734	0.158	0.963	0.002	0.020	0.024	0.012	0.020	0.039	1.791	0.001	0.125	0.011	0.125	0.070	1214.506	1217.487	0.922	0.017
DS5c	1216.104	0.703	0.185	0.727	0.174	0.932	0.003	0.037	0.066	0.012	0.020	0.079	1.783	0.001	0.162	0.011	0.162	0.091	1214.497	1217.474	0.921	0.022
DS6a	1216.104	0.693	0.095	0.700	0.191	0.873	0.002	0.069	0.055	0.012	0.020	0.092	1.723	0.001	0.041	0.011	0.042	0.025	1214.535	1217.422	0.920	0.006



Cut Name	Cut Description	$\langle \epsilon_{total} \rangle$	$\hat{\epsilon}_{total}$	$\langle \epsilon_{unique} \rangle$	$\hat{\epsilon}_{unique}$	Sacrifice	$\Delta DP$
Enriched Source		M1: 25.2 %	24.7 <sup>+3.5</sup> <sub>-3.2</sub> %	0.0 %	0.0 <sup>+0.6</sup> <sub>-0.9</sub> %	1.9 %	0 %
Detector Cut	Any other detector: isBar	M2: 41.8 %	61.9 <sup>+3.1</sup> <sub>-7.7</sub> %	0.0 %	0.0 <sup>+2.3</sup> <sub>-0.9</sub> %	3.8 %	0 %
Multiplicity 2 Cut	m=2	M1: 14.8 %	19.8 <sup>+3.3</sup> <sub>-2.9</sub> %	0.0 %	0.0 <sup>+0.6</sup> <sub>-0.9</sub> %	0.0 %	1 %
Coincident Energy Cut	Any other detector: energy>817.7 & energy<825.4	M2: 11.6 %	4.8 <sup>+4.5</sup> <sub>-2.4</sub> %	0.0 %	0.0 <sup>+2.3</sup> <sub>-0.9</sub> %	0.0 %	0 %
Combined Cuts		M1: 100.0 %	100.0 <sup>+0.0</sup> <sub>-0.0</sub> %	61.6 %	59.3 <sup>+3.8</sup> <sub>-3.9</sub> %	18.1 %	781 %
		M2: 100.0 %	100.0 <sup>+2.3</sup> <sub>-0.0</sub> %	48.9 %	35.7 <sup>+7.6</sup> <sub>-7.0</sub> %	19.6 %	0 %
		M1: 100.0 %	100.0 <sup>+0.6</sup> <sub>-0.0</sub> %	—	—	24.2 %	936 %
		M2: 100.0 %	100.0 <sup>+0.0</sup> <sub>-2.3</sub> %	—	—	29.4 %	0 %

TABLE XXVII Table of cut descriptions and efficiencies for simulated backgrounds and measured data for the 1216 keV peak.

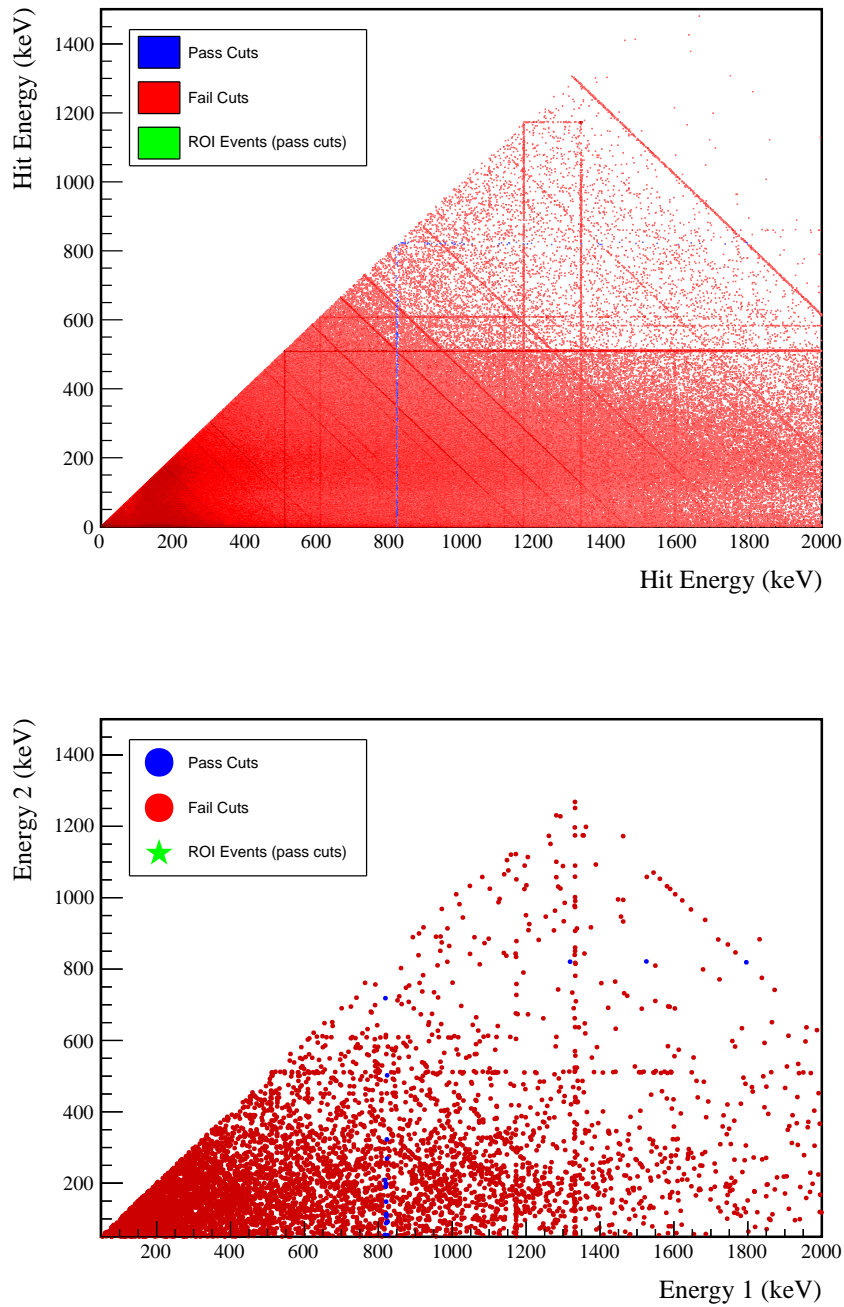
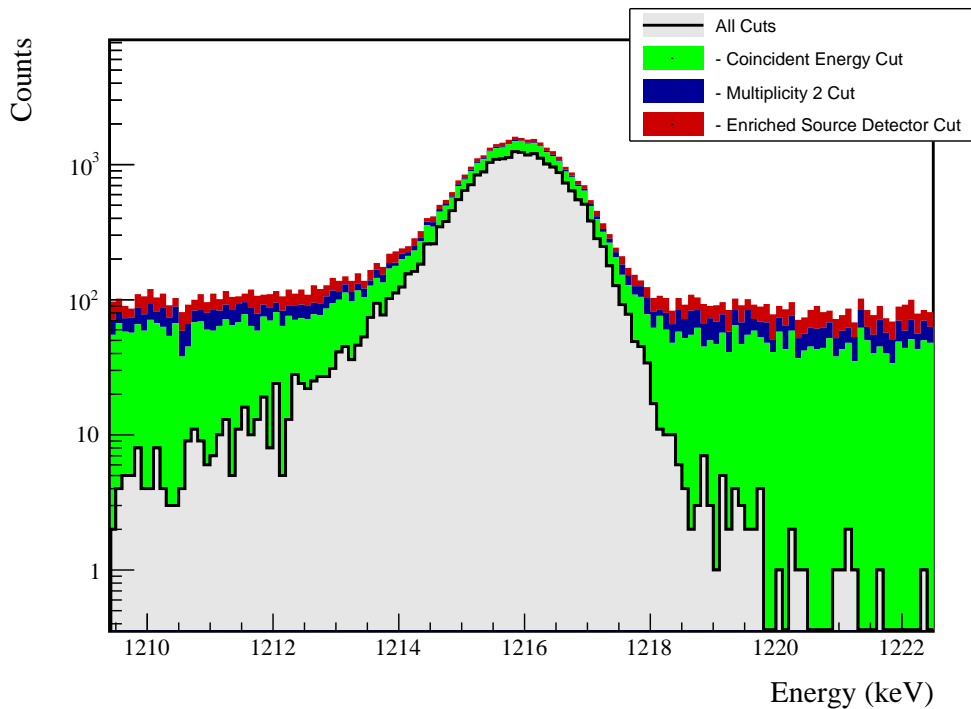


FIG. 103 Simulated (left) and measured (right) multiplicity 2 energy spectrum with sum and coincident energy cuts included for the 1216 keV peak.

FIG. 104 Effect of all cuts applied sequentially on ROI for 1216 keV peak of  $0\nu\beta\beta$  to  $2_2^+$ 

Source	Module 1 efficiency	Module 2 efficiency
Multi-Detector with Full Energy $\gamma$	$0.8 \pm 0.2\%$	$0.4 \pm 0.5\%$
Region of Interest	$92.0 \pm 0.9\%$	$92.0 \pm 0.9\%$
Dead Layer	$69.2 \pm 5.2\%$	$58.6 \pm 7.2\%$
Detector Dead Times	$98.3 \pm 0.8\%$	$98.6 \pm 0.7\%$
Enriched Source Detector Cut	$96.4 \pm < 0.1\%$	$91.7 \pm < 0.1\%$
Multiplicity 2 Cut	$97.4 \pm < 0.1\%$	$98.2 \pm < 0.1\%$
Coincident Energy Cut	$77.7 \pm 0.3\%$	$74.4 \pm 0.3\%$
Final Efficiency	$0.43 \pm 0.12\%$	$0.18 \pm 0.21\%$

FIG. 105 Table of detection efficiencies for the 1216 keV peak.

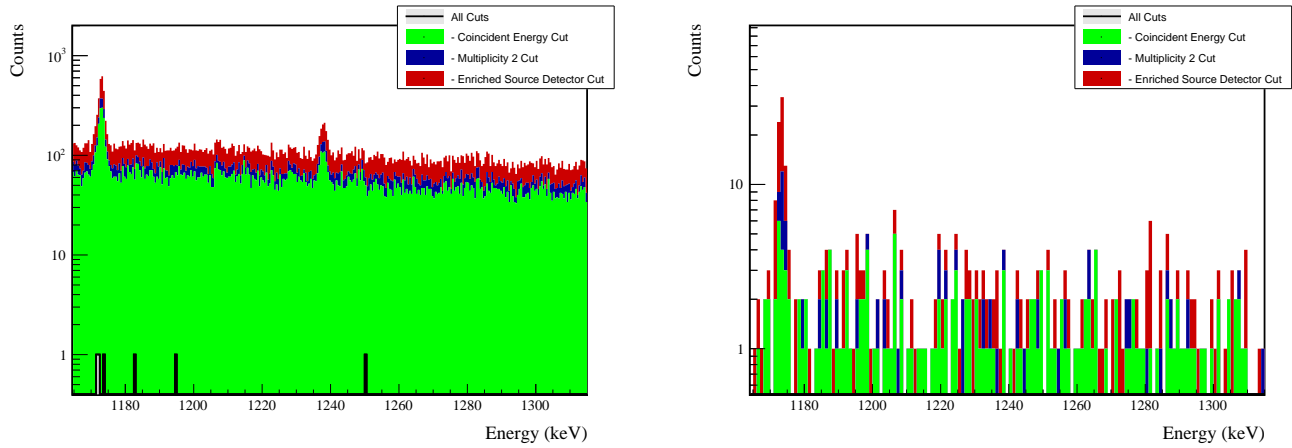


FIG. 106 Effect of all cuts applied to sequentially simulated (left) and measured (right) background data.

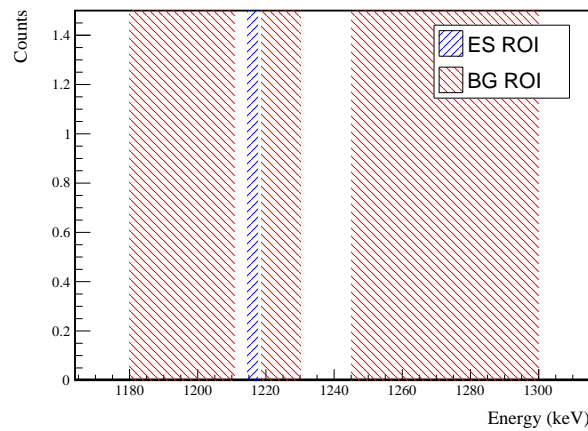


FIG. 107 All events after cuts in background (red) and signal (blue) ROIs for 1216 keV peak of  $0\nu\beta\beta$  to  $2_2^+$



## 719 Appendix H: Sensitivity and Discovery Potential

720 When performing rare event searches in the presence of backgrounds, it is often useful to select regions of interest  
721 and data cleaning cuts that optimize the experimental sensitivity. Median  $n\sigma$  count sensitivity,  $\hat{S}(\bar{B}, n_\sigma)$  is defined as  
722 the median upper limit of an  $n\sigma$  confidence interval on the number of observed signal counts, assuming the presence  
723 of no signal and backgrounds sampled from a distribution based on measured background level  $\bar{B}$ . A similar quantity,  
724  $n\sigma$  discovery sensitivity, is defined as the true strength of a signal that would produce a discovery with significance  
725  $n\sigma$  50% of the time. Unlike median sensitivity, discovery sensitivity accounts for the distribution in the number  
726 of counts that would be seen based on the true rate. For this reason, discovery sensitivity is a slightly more useful  
727 quantity when projecting or optimizing an experiment's sensitivity, even though median (or mean) sensitivity is the  
728 quantity that is usually reported. For the purpose of this appendix, we will focus on discovery sensitivity.

729 The sensitivity of the experiment to the total rate of the process being searched for is

$$\hat{\Gamma}(\bar{B}, \epsilon, n_\sigma) \propto \frac{\hat{S}(\bar{B}, n_\sigma)}{\epsilon} \quad (H1)$$

730 where  $\epsilon$  is the total detection efficiency of the signal being sought. Optimizing event selection for a search requires  
731 balancing the tradeoff between reducing backgrounds, which will decrease  $\hat{S}(\bar{B})$ , and improving signal detection  
732 efficiency.

733 When optimizing a search, it is useful to use certain approximations when calculating sensitivity. In the high  
734 background limit, a common approximation is to assume the backgrounds measured will have a gaussian distribution  
735 with standard deviation of  $\sqrt{\bar{B}}$ . In this case, the discovery (and median) sensitivity will be

$$\hat{S}(\bar{B}, n_\sigma) = n_\sigma * \sqrt{\bar{B}} \quad (H2)$$

736 This approximation fails, however, in the low background limit, where a better approximation is that the background  
737 will instead be sampled from a Poisson distribution with mean counts  $\bar{B}$ . Because the Poisson distribution is a PDF  
738 over a discrete variable, the resultant sensitivity will have step-like properties and must be solved for using a toy  
739 Monte Carlo, properties that are not ideal for performing sensitivity optimizations. For this reason, when computing  
740 the sensitivity we instead use the analytic continuation of the CDF of the poisson distribution, which is the lower  
741 incomplete gamma function

$$\gamma(s, x) = \frac{1}{\Gamma(s)} \int_0^x t^{s-1} e^{-t} dt \quad (H3)$$

742 In this case, we can find the sensitivity, by first numerically solving for the number of counts required for an  $n$ -sigma  
743 discovery,  $\hat{N}$ , with expected backgrounds  $\bar{B}$ , where

$$\gamma(\hat{N} + 1, \bar{B}) = \operatorname{erfc}\left(\frac{n_\sigma}{\sqrt{2}}\right) \quad (H4)$$

744 To get the median sensitivity, we then numerically solve

$$\gamma(\hat{N} + 1, \bar{B} + \hat{S}) = 0.5 \quad (H5)$$

745 We define the function found by solving these equations to be the discovery potential[15],

$$\hat{S}(\bar{B}, n_\sigma) = \operatorname{DP}(\bar{B}, n_\sigma) \quad (H6)$$

746 For the purposes of this dissertation, we always use the 3-sigma discovery potential

$$\operatorname{DP}(\bar{B}) = \operatorname{DP}(\bar{B}, 3) \quad (H7)$$

747 Figure 108 shows a comparison of the gaussian approximation for sensitivity to the discovery potential. This function is  
748 implemented in `GATPeakShapeUtils.hh` as  
749 `GATPeakShapeFunction::DiscoveryLimit`.

750 Next, we want to figure out how we will use these quantities to optimize our data selection. To determine whether  
751 it is worth adding a cut or modifying a cut, consider the efficiency and expected background counts before and after  
752 applying the cut ( $\epsilon_i$ ,  $\bar{B}_i$  and  $\epsilon_f$ ,  $\bar{B}_f$ , respectively). A cut represents an improvement if

$$\frac{\hat{S}(\bar{B}_f)}{\epsilon_f} < \frac{\hat{S}(\bar{B}_i)}{\epsilon_i} \quad (H8)$$

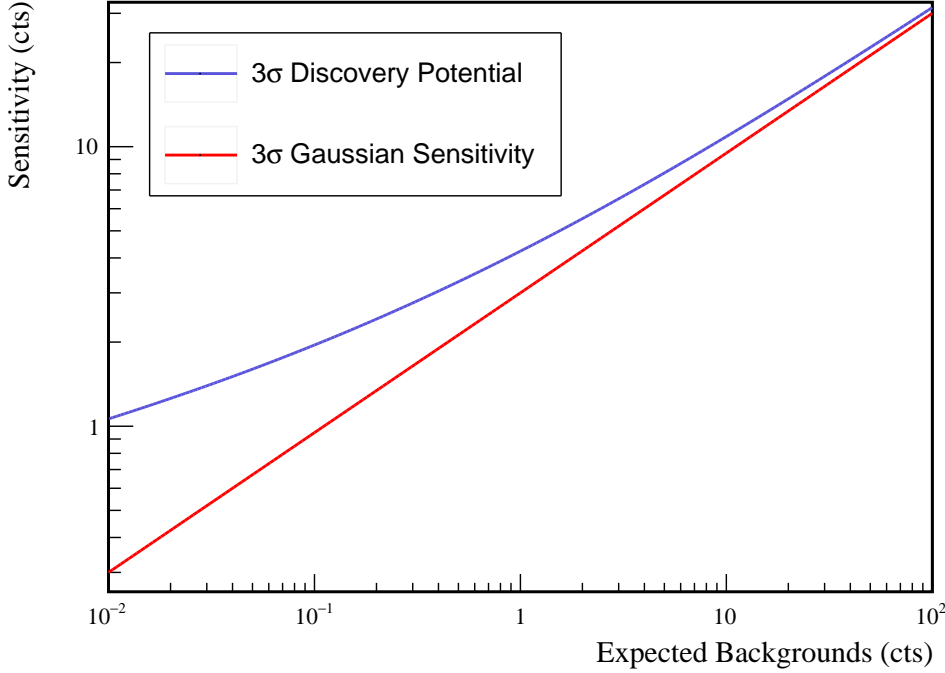


FIG. 108 A comparison of the Gaussian approximation for sensitivity and the discovery potential as a function of expected background level. Note that in the high background limit, both formulations for sensitivity converge, as expected.

753 Rearranging this, we get

$$\frac{\Delta \hat{S}(\bar{B})}{\hat{S}(\bar{B}_i)} < \frac{\Delta \epsilon}{\epsilon_i} \quad (\text{H9})$$

754 If we assume that a small number of events are cut, we can Taylor expand:

$$\frac{\partial \hat{S}}{\partial \bar{B}} \frac{\Delta \bar{B}}{\hat{S}(\bar{B})} < \frac{\Delta \epsilon}{\epsilon} \quad (\text{H10})$$

755

$$\frac{\partial \log(\hat{S})}{\partial \log(\bar{B})} > \frac{\text{False Positive Rate}}{\text{True Positive Rate}} \quad (\text{H11})$$

756 Looking at figure 108, we see that in the high background limit, using the Gaussian sensitivity approximation we will  
 757 draw the same conclusion about whether or not a cut is worth applying regardless of the absolute background level. A  
 758 cut is worth applying as long as the true positive rate of the cut is twice the true negative rate. On the other hand, in  
 759 the low background limit, this is not the case; instead, as we approach zero background, we will be less aggressive in  
 760 cutting events. For this reason, experiments approaching the background free limit will use wider regions of interest  
 761 in peak searches.